5-2014

Investigation of the Phase Transformation Kinetics and Texture Evolution in a TRIP Steel under Complex Loads

Ercan Cakmak
University of Tennessee - Knoxville, ecakmak@utk.edu

To the Graduate Council:

I am submitting herewith a dissertation written by Ercan Cakmak entitled "Investigation of the Phase Transformation Kinetics and Texture Evolution in a TRIP Steel under Complex Loads." I have examined the final electronic copy of this dissertation for form and content and recommend that it be accepted in partial fulfillment of the requirements for the degree of Doctor of Philosophy, with a major in Materials Science and Engineering.

Hahn Choo, Major Professor

We have read this dissertation and recommend its acceptance:

Peter K. Liaw, Yanfei Gao, John D. Landes

Accepted for the Council:

Carolyn R. Hodges

Vice Provost and Dean of the Graduate School

(Original signatures are on file with official student records.)

Investigation of the Phase Transformation Kinetics and Texture Evolution in a TRIP Steel under Complex Loads

A Dissertation Presented for the

Doctor of Philosophy

Degree

The University of Tennessee, Knoxville

Ercan Cakmak

May 2014

DEDICATION

This Doctoral dissertation is dedicated to my parents and uncles who have supported me through continuous love and encouragement during my PhD study. I would also like to dedicate this work to the Akyildiz family who had accepted me as part of their own during my stay in USA. Further dedication is given to other family members and friends for their support.

ACKNOWLEDGEMENTS

First of all, I would like to express my deepest gratitude to my advisor Prof. Hahn Choo for his guidance and constant support on my research during my Ph.D at the University of Tennessee. Without his support it would be impossible to complete my Ph.D study. I would also like to thank my committee members, Prof Yanfei Gao, Prof. Peter K. Liaw and Prof. John D. Landes for their precious time and effort devoted to the completion of my Ph.D degree.

I am thankful to Dr. Ke An at the Spallation Neutron Source (SNS), Oak Ridge National Laboratory (ORNL), for his help and guidance during my Ph.D study. Further thanks are in order for Dr. Yang Ren for his help during my experiments at the Advanced Photon Source (APS), Argonne National Laboratory (ANL), that constitute the majority of this thesis work. I also owe my thanks to Mr. Harley Skorpenske (ORNL) for his help with the mechanical testing and Mr. Douglas Fielden (UT) for the sample preparations.

This research is supported in part by the NSF Major Research Instrumentation (MRI) program under contract DMR.0421219. Use of the Advanced Photon Source was supported by the Scientific User Facilities Division, Office of Basic Energy Sciences, U.S. Department of Energy, under Contract No. DE-AC02-06CH11357. The work at Oak Ridge National Laboratory was sponsored by the Scientific User Facilities Division, Office of Basic Energy Sciences, U.S. Department of Energy. I would also like to acknowledge the International Center for Diffraction Data (ICDD) for the support supplied by the 2012 and 2013 Ludo Frevel Crystallography Scholarship Awards.

ABSTRACT

The martensitic phase transformation kinetics and its relation with texture evolution and deformation/transformation microstructures under complex loading conditions were investigated in a 304L stainless steel that exhibits the transformation induced plasticity (TRIP) effect when strained at ambient temperature. The applied load paths included torsional and biaxial deformation scenarios including simultaneous biaxial torsion/tension and torsion/compression as well as stepwise deformation of tension followed by torsion. Synchrotron x-ray and electron back-scatter diffraction techniques were used to investigate the phase transformation-microstructure-texture evolutions relations.

Under torsional deformation, the inhomogeneous distribution of martensite phase fractions were recorded through the radius of solid cylindrical specimens consistent with the shear strains showing a linear variation along the radial position. The fundamental studies on phase transformation kinetics and texture evolution during torsional deformation were conducted using data close to the surface of the specimens. Texture-transformation relations were also investigated and preferential phase transformation of grains belonging to certain components in the parent austenite phase (namely the C- and B-texture components) was identified.

When the specimens were deformed under biaxial deformation conditions, the resultant phase transformations were enhanced under biaxial torsion/tension and stepwise tension-torsion cases, whereas there was a decrease in transformation kinetics under the

biaxial torsion/compression loading. Further analyses were performed with selected subsets of the biaxial loading studies and the changes in phase transformation kinetics were discussed in the context of preferential phase transformation mechanisms and effects of the addition of axial strains on the phase transformation kinetics. Furthermore the results were also discussed from a microscopic perspective including the formation of shear bands and their intersections, and volume changes associated with the martensitic transformation.

Table of Contents

List of Tables

List of Figures

Chapter 1 Introduction

1.1. Transformation Induced Plasticity

Austenitic stainless steels exist within a range of stacking fault energy (SFE) levels from medium to low. As the SFE is lowered in these alloys, the stability of the fcc austenite phase (γ) decreases. As the stability of austenite decreases, the TRansformation Induced Plasticity (TRIP) phenomenon [1-3] can occur by the transformation of the parent austenite to product bcc (α') and hcp (ε) martensite phases [4, 5], with applied strains. Such evolution of constituent phases during deformation and forming processes (e.g., rolling, drawing, etc.) has important ramifications on the physical and mechanical properties of the material, affecting its strength, total elongation, formability, and possible failure modes [6-8].

In particular, the effective increase in the strain hardening rate due to the in-situ formation of the bcc martensite phase during the deformation helps to prevent premature failure and increase the ductility while maintaining the high strength of the material. In general, the harder bcc martensite phases act as barriers to dislocation motion during straining and enhance the strain hardening rate in this type of alloys [9]. The TRIP effect, therefore, helps increase the formability of these alloys, e.g., achieving higher rolling reductions without premature failure since the transformation occurs more readily at locations with the highest strain concentration, and allowing the manufacturing of more complex shapes. However, for enhanced ductility gradual introduction of the martensite is essential because otherwise only the yield strength will increase if the transformation is rapid [9, 10]. Therefore, the strain-induced martensitic transformation kinetics is an important fundamental and practical issue.

Moreover, texture evolution, in general, is an important aspect of plastic deformation studies since it affects critical material properties such as modulus, hardening rate, ductility, and toughness during and after the manufacturing processes [11]. One of the most important aspects of the texture evolution in TRIP steels is that it can also influence the martensitic phase transformation such that grains with certain crystallographic orientations can transform more readily than others [12]. Furthermore, due to the parent austenite being textured, the resultant martensite is also expected to be textured and, subsequently, contributes to the plastic anisotropy [13-15].

1.2. Motivation and Scientific Issues

The TRIP phenomenon, in general, is fairly well understood for uniaxial deformation conditions. Torsional deformation studies, on the other hand, have so far been conducted using single phase (mostly fcc) materials. However, the TRIP effect under torsional and biaxial deformation conditions involving a combination of axial and shear strains, especially regarding the phase transformation - texture evolution relations, are not well understood. The main motivation of this research involves a systematic investigation of deformation and transformation behavior under torsional and biaxial deformation conditions. In this study, commercial-grade TRIP steel was used to investigate the role of martensitic phase transformation on the material behavior with a focus on the transformation-texture relations and possible selective transformation mechanisms under loading conditions that are more complex than simple uniaxial tensile or compression loadings.

In addition to the pure torsional loading, biaxial loading paths investigated in this study involve various combinations of torsional and axial loads. These are: 1) simultaneous application of torsional and tensile strains, 2) simultaneous application of torsional and compressive strains, and 3) stepwise deformation of tension followed by torsion.

The main objectives of this study can be summarized for pure torsion and biaxial deformation cases as follows:

A. Pure Torsion

(1) Advance the basic understanding of the phase transformation kinetics under torsional deformation in comparison to uniaxial deformation cases;

(2) Distinguish the texture evolution for a multi-phase TRIP steel from that of a single phase material and identify the interaction between deformation and transformation textures.

(3) Identify potential influence of the transformation on the texture evolution of the parent austenite phase and investigate preferential transformation.

(4) Investigate the product bcc martensite texture evolution for a possible relation with that of the parent phase in terms of texture inheritance and also study other contributing factors to its texture formation.

B. Biaxial Loading

(5) Investigate the influence of the introduction of axial strains over the shear strains for a given equivalent strain range on the transformation behavior.

(6) Differentiate the texture evolution from pure torsional deformation and also within the different biaxial deformation cases; and relate the texture evolution to the observed changes in the transformation behavior.

(7) De-convolute the effects of proportional and non-proportional loading and identify the major differences when the axial strains change from positive to negative.

The better understanding of microscopic material behavior such as texture, phase, and deformation/transformation microstructure evolutions of the TRIP alloy under complex loads can aid in the development of more advanced TRIP steels. The results from this study could also help improve the industrial forming operations where combinations of shear and axial forces are applied.

Chapter 2 Literature Review

2.1. Martensitic Phase Transformation

Martensitic transformation in austenitic steels can occur under strain [16], temperature change [17] or both [2, 3, 13, 18]; which involves the transformation of the metastable austenitic (γ) parent phase into bcc/bct (α') and hcp (ε) martensite phases [19-21]. The phase change occurs by the movement of an interface formed between the parent and the product phases; and atomic realignments from one structure to another take place, e.g., fcc to bcc, as this interface moves. This is a diffusionless process and therefore the compositions of the parent and product phases stay the same [22].

Metals capable of going through the martensitic phase transformation have an equilibrium temperature between the austenite and the martensite phases, denoted with T_0, Figure 2.1 [22, 23]. Even though the two phases are in energy equilibrium at T_0, when the temperature is lowered towards the martensite start temperature (M_S), the free energy difference between the austenite and martensite phases increases; and the parent phase becomes unstable. This energy difference reaches the critical value, ΔF_{cr}, at M_S, Figure 2.1; and once the critical energy is achieved spontaneous transformation takes place to lower the system's energy. However, this transformation is reversible and the reverse transformation takes place at the austenite start temperature, A_S, where the martensite phase becomes unstable, Figure 2.1.

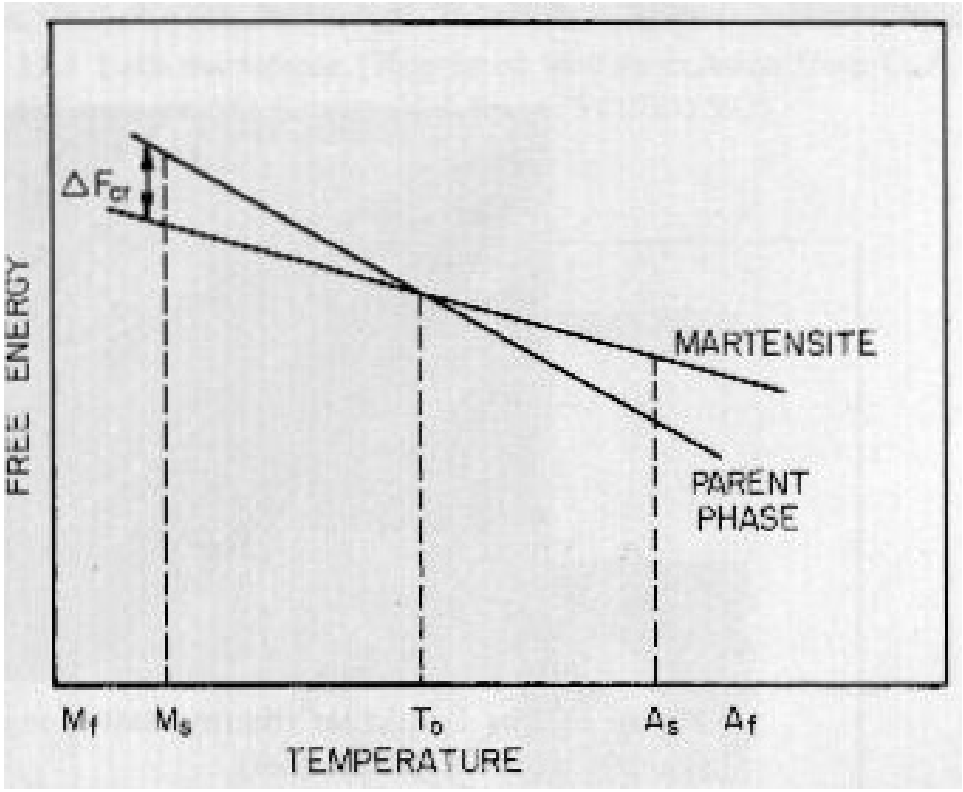

Figure 2.1. Free energy difference between the parent austenite and the product martensite phases as a function of temperature [23].

M_S depends mainly on three factors: a) the T_0 temperature, b) F_N, the strain and surface energy of nucleation and the existence of sites for heterogeneous nucleation such as grain boundaries; and c) F_τ, the stress to overcome to shear austenite into martensite. The energy needed for the initiation of martensitic transformation can be given with Eq. (2-1);

$$F_{\alpha\gamma} \geq F_N + F_\tau \tag{2-1}$$

which corresponds an undercooling, ΔT, defined by Eq. (2-2), where $\Delta S_{\alpha\gamma}$ is the transformation entropy.

$$\Delta T = T_0 - M_S = \frac{F_N + F_\tau}{\Delta S_{\alpha\gamma}} \tag{2-2}$$

F_τ can further be defined by the relation presented in Eq. (2-3) where τ is the stress that is required to be overcome by the partial dislocations that move during shear while the martensite crystal is formed; V is the molar volume, and φ is the angle of shear for the γ to α transformation.

$$F_\tau = \frac{1}{2}(V\tau\varphi) \tag{2-3}$$

F_τ will be increased by the generation of obstacles to dislocation motion such as those observed under solid-solution, precipitation, and work hardening conditions [24].

M_S can further be affected by the previous mechanical and thermal history as well as the grain size [25]. Figure 2.2 shows the effect of grain size and pre-deformation on M_S [23]; illustrating that M_S increases with increasing grain size and pre-deformation.

Even though martensite starts forming spontaneously at M_S, continuous lowering of the temperature is required for the transformation to continue, Figure 2.3.

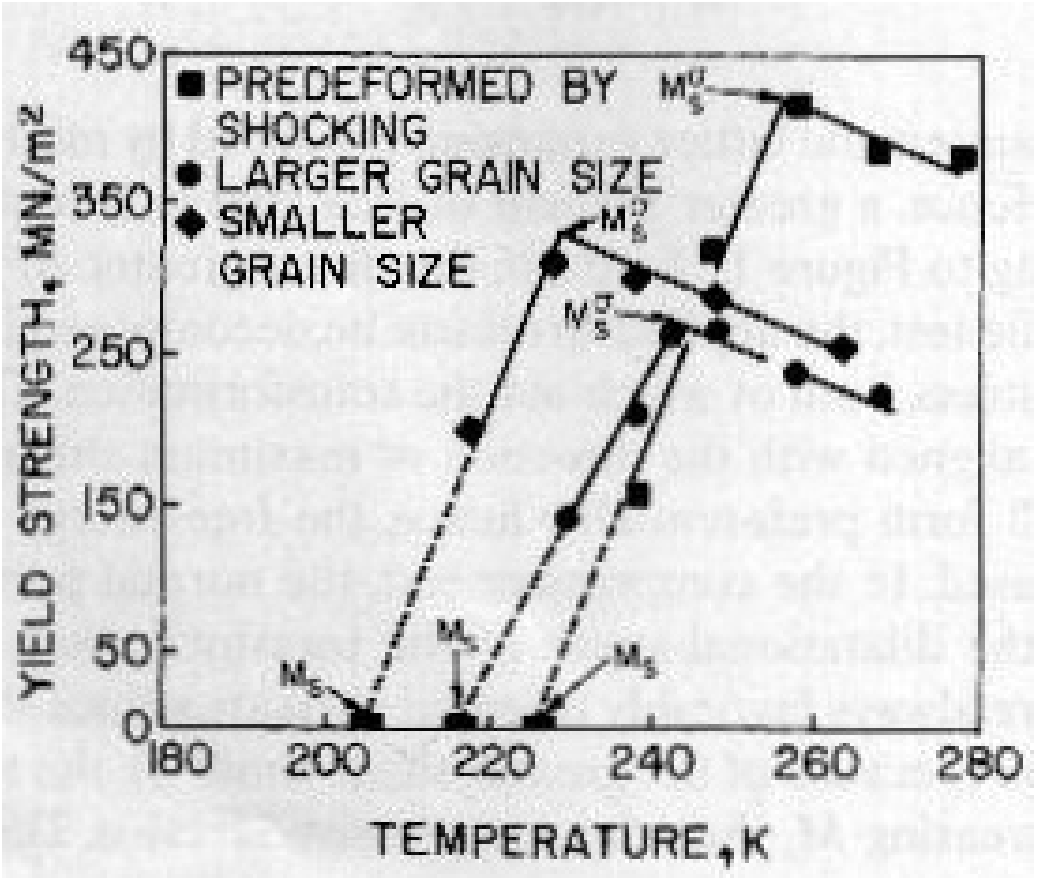

Figure 2.2. Effect of grain size and pre-deformation on the M_S and M_S^σ temperatures [23].

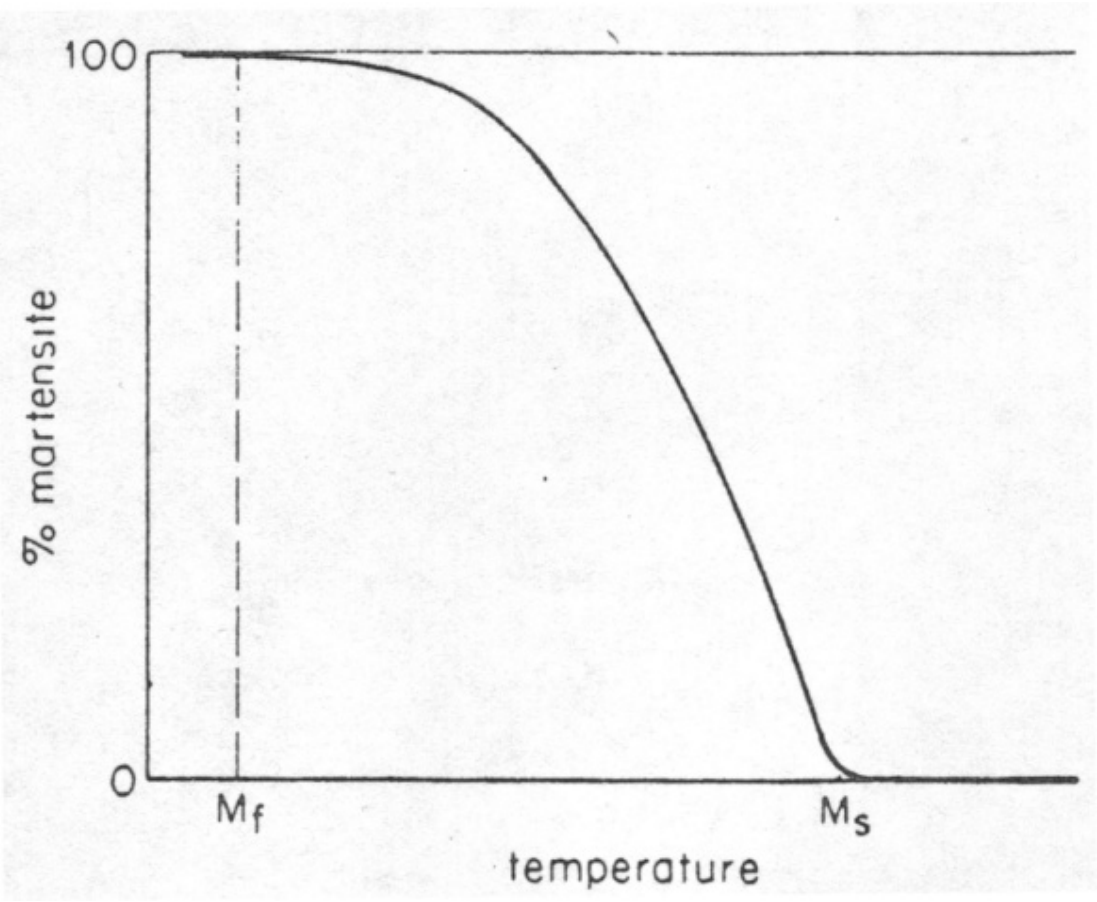

Figure 2.3. Martensitic transformation-temperature diagram illustrating the athermal martensitic transformation from start (M_S) to finish (M_F) [26].

As presented in this figure, with further lowering the temperature spontaneous transformation continues until no further reaction can take place and this cut-off temperature is defined as M_f. Overall, this type of transformation is called the athermal martensitic transformation [26].

As the transformation continues athermally, retained austenite remains in spaces between the martensite and the stress induced by the martensite during formation work-hardens the austenite thereby stabilizing it against further transformation [24]. Therefore, if isothermal holding is initiated at a temperature during cooling, the interface between the parent and the product phases is prohibited from further movement, stopping the transformation [22]. Hence, if the temperature is kept constant for a period of time, further undercooling will be required for the transformation to restart [22, 24].

The chemical driving force for the martensite to form at M_S is about 300 cal/mole and when there is not enough driving force for spontaneous transformation, the externally applied stresses or strains can aid the transformation [25]. For instance, between M_S and M_S^σ the decrease in the chemical driving force can be counterbalanced by the application of elastic stresses. However, the required stresses increase with increasing temperature since the chemical driving force decreases with increasing temperature [27].

Moreover, martensitic transformation is regarded as a deformation mechanism and therefore competes with slip. As the martensitic transformation becomes easier with lowering the temperature, yielding by slip becomes harder; and, therefore, at temperatures near M_S below M_S^σ temperature, the deformation is induced by stress-assisted transformation rather than slip [28].

On the other hand, above M_S^{σ} the transformation can only be strain-induced where plastic deformation increases the internal strains in the parent phase and makes the nucleation of martensite easier. There is however a limiting temperature where martensitic transformation can take place even when aided by applied strains and this is defined as the M_D temperature [22, 29].

Martensitic transformation does not occur randomly. They can nucleate in lattice defects where metastable atomic arrangements suitable for martensitic transformation can exist. These metastable arrangements can then transform into martensite by external forces such as thermal vibrations, e.g., cooling-induced martensite [30]. Stacking faults are considered as lattice defects and in the work of Kelly sheets of ε martensite were formed on overlapping stacking faults in a Mn-Cr-Ni steel quenched to -196 ^{o}C. Furthermore, α' martensite was observed at the intersection of ε sheets. TEM micrographs are used to illustrated these in Figures 2.4 and 2.5 [31].

The stress-assisted martensite occurs on pre-existing nucleation sites, i.e., same sites which transform spontaneously on cooling below M_S. Strain-induced martensite, on the other hand, occurs on new nucleation sites or embryos, created by the applied plastic strains [20, 26]. For example, Brooks et al. have observed hcp martensite to nucleate on overlapping stacking faults formed by deformation [32, 33]. Gey et al. has also reported hcp martensite to result from stacking faults in each second (111) plane [34]. As for bcc martensite, nucleation preferentially takes place at the intersections of localized dislocation bands, mechanical twins, hcp martensite bands, and dense stacking fault bundles; all called shear bands [20, 34].

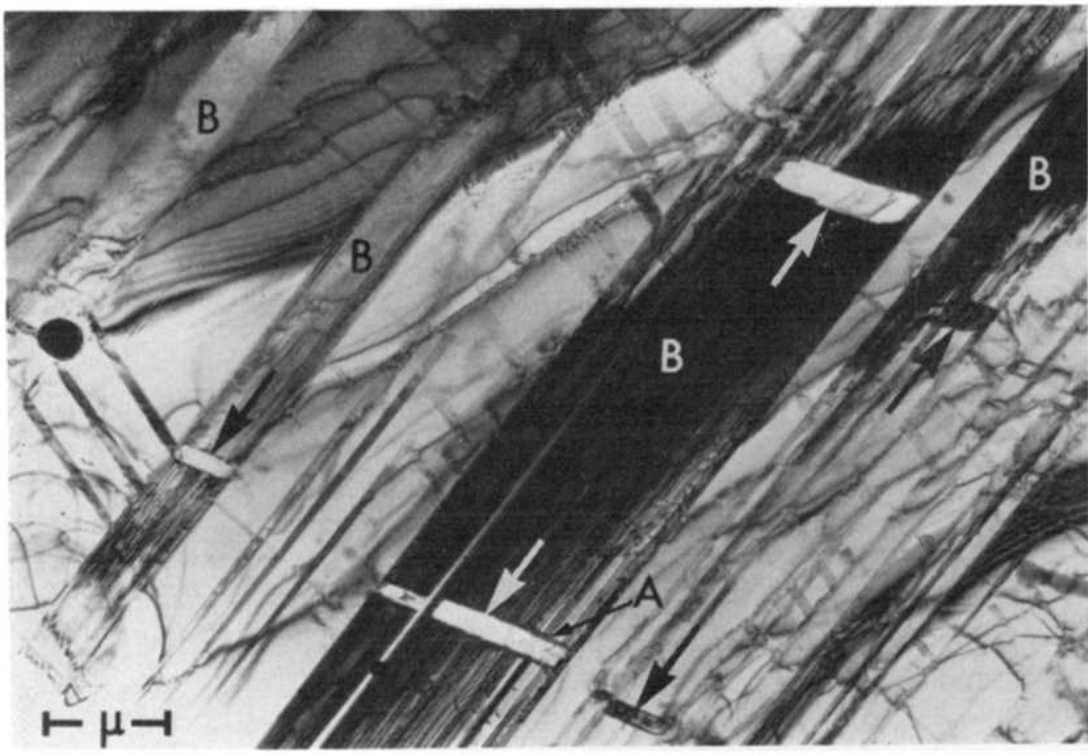

Figure 2.4. Formation of ε martensite bands (B) containing α' martensite laths (indicated by large arrows) in a Mn-Cr-Ni steel quenched to -196 ^{o}C [31].

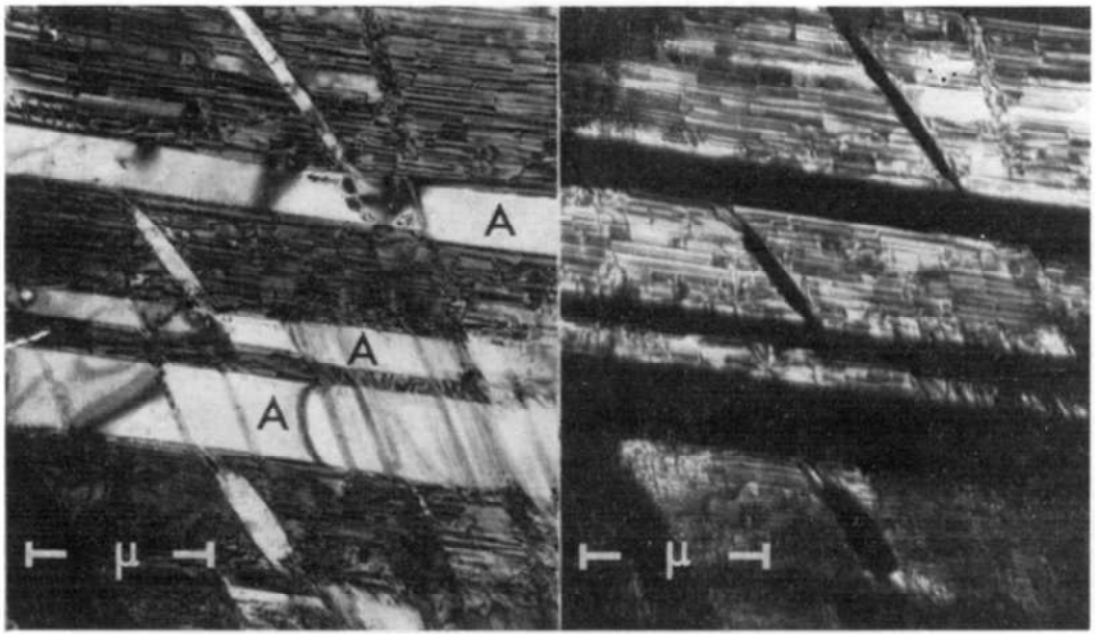

Figure 2.5. Bright field (left) and dark field (right) micrographs of the Mn-Cr-Ni steel quenched to -196 ^{o}C. The ε phase appears as dark bands in the bright field micrographs and the α' laths are contained within these bands (white laths). Retained austenite phase between the ε bands is also present (A). In the dark field micrograph the ε martensite bands appear as white with the α' laths as dark lines inside. The austenite phase is also imaged dark [31].

Examples are presented in Figures 2.6 [19] and 2.7 [35] that show bcc martensite nucleation at the intersection of hcp martensite plates and slip bands, respectively.

Furthermore, the formation of martensite plates involves a shape change in a given volume of the material and therefore is affected by the nature of the applied stresses, both shear and normal. Depending on the nature of the stress, for instance, the M_S temperature can be raised or lowered. To illustrate the effect of the stress-state in a very simplistic approach, the formation of a martensite plate associated with pure shear is given in Figure 2.8 for two opposite scenarios. Presented in Figure 2.8a, the shear stress favors the transformation when the sense of applied shear stress is the same as the strain thereby, requiring a lower driving force. On the contrary, when the stresses are opposing the strain, Figure 2.8b, it would be harder for the plate to form therefore increasing the necessary driving force [22].

The stress-temperature diagram is shown in Figure 2.9 summarizing the conditions required for various transformation modes. To begin with, the stress-assisted transformation occurs below the yield point of the material (denoted by C in the figure) which also defines the highest temperature, M_S^σ, where martensite can be induced by the application of elastic stresses. On the other hand, the strain-induced transformation occurring at temperatures higher than M_S^σ past the yield stress, follows the curve CE where E corresponds to the maximum stress that results in fracture, defining the temperature M_D. Due to the effectiveness of the strain-induced nucleation sites, the strain-induced transformation curve could also follow the curve CD for the initiation of

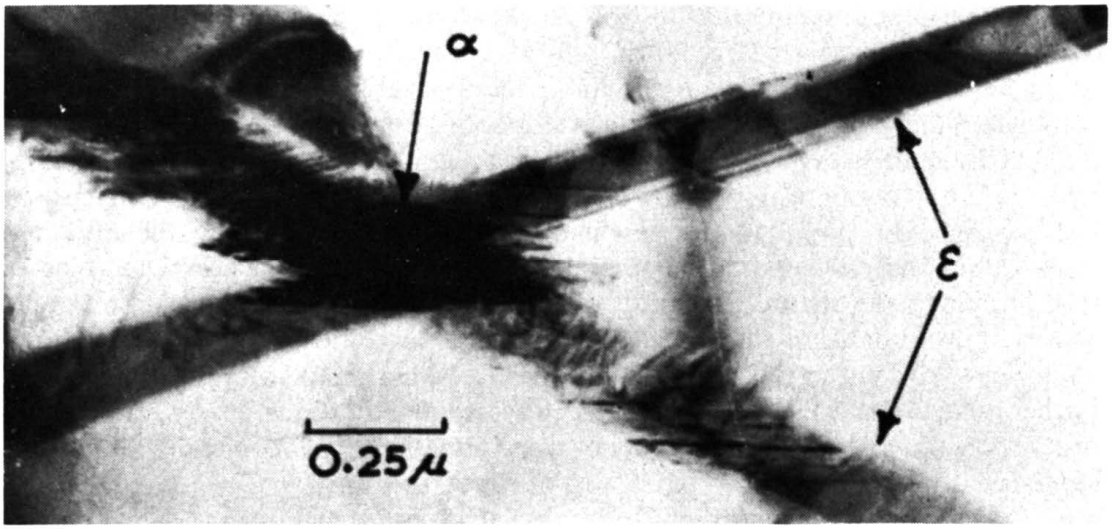

Figure 2.6. Nucleation of bcc martensite (α') at the intersection of two hcp martensite (ε) plates [19].

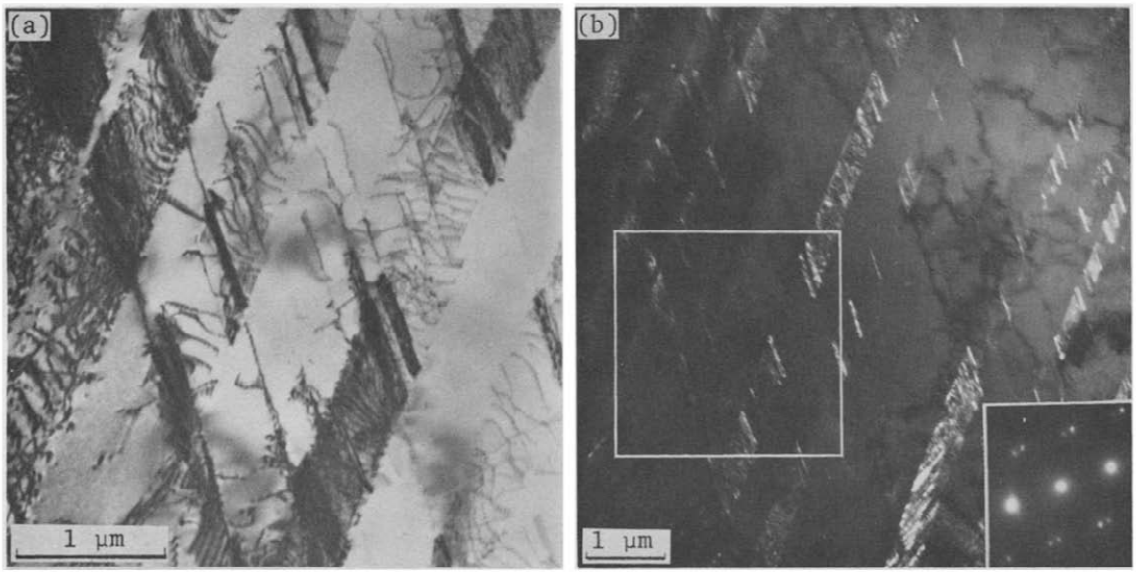

Figure 2.7. a) Bright field and b) dark field TEM micrographs showing formation of bcc martensite (α') at the intersection of two slip bands where (a) corresponds to the area marked by the white frame in (b) [35].

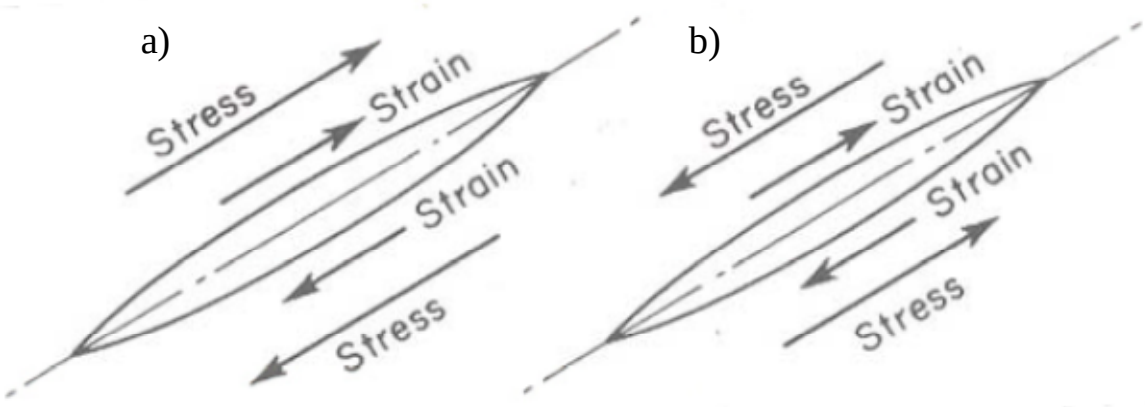

Figure 2.8. Effect of stress-state on formation of martensite [22].

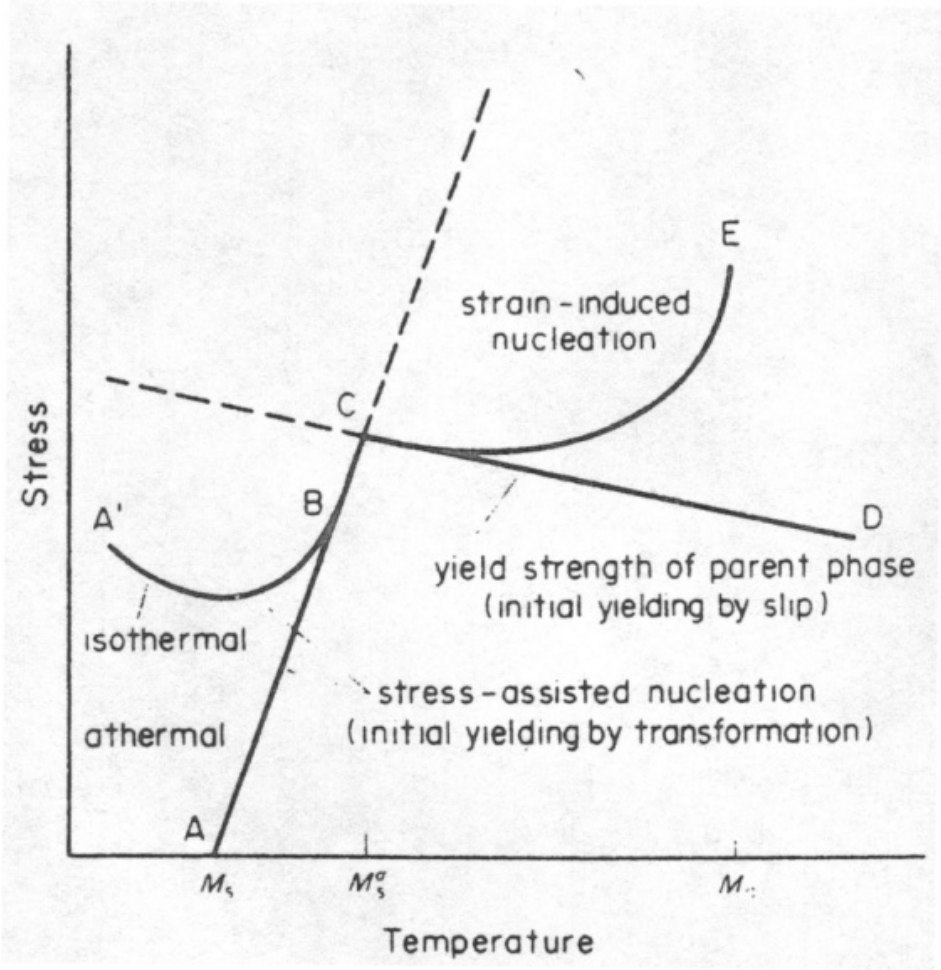

Figure 2.9. Stress-temperature diagram showing the distinct zones for various transformation modes [26].

the parent phase slip. Also, both stress-assisted and strain-induced mechanisms can be operative at M_S^σ [26].

As for the athermal martensitic transformation, the critical stress for the stress-assisted martensite formation increases linearly with an increase in temperature in the range between M_S and M_S^σ that forms the line ABC.

The difference in the transformation mechanisms between the stress-assisted and the strain-induced modes is also illustrated in Figure 2.2 regarding the temperature dependence. According to the figure, as the temperature difference between the M_S and the current temperature increases, the stress at which the martensite forms increases as well and this is designated as the increase in the yield stress (between M_S and M_S^σ) since the material yields by martensite formation at this interval. When the M_S^σ temperature is reached, yielding starts to occur by slip and the slope of the yield curve changes showing the regular decrease with increasing temperature.

2.1.1. Transformation Mechanisms

2.1.1.1. Formation of hcp Martensite

Both fcc and hcp crystals possess close packed structures with similar atomic arrangements on their close packed planes, $(111)_{fcc}$ and $(0001)_{hcp}$. When every two adjoining (111) planes of the fcc crystal are displaced towards the $[11\bar{2}]$ direction by a distance $a/\sqrt{6}$ (a is the lattice parameter), an hcp type stacking can be achieved, Figure 2.10.

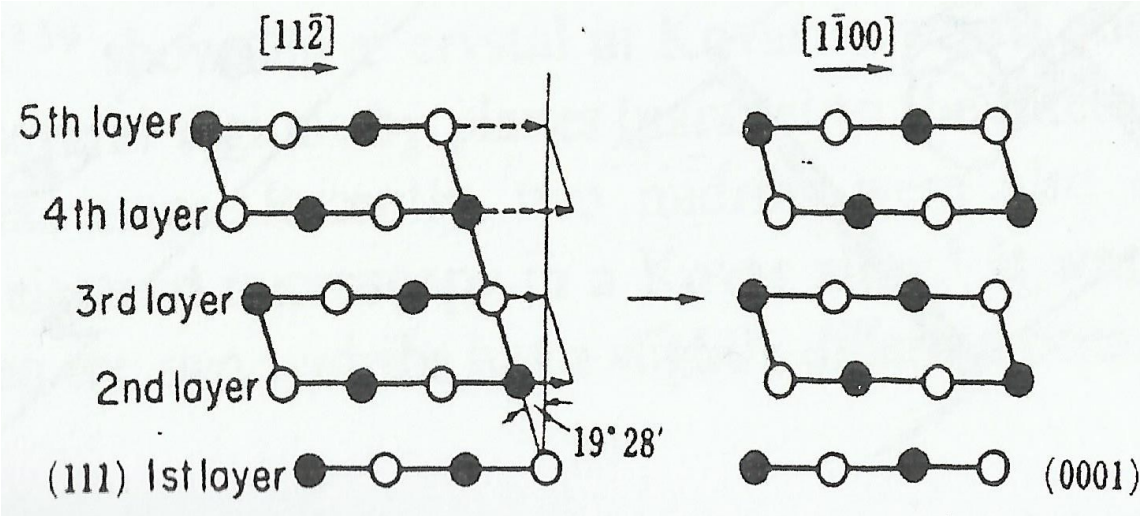

Figure 2.10. Transformation of the fcc structure into hcp structure. Here open and solid circles resemble the atoms lying on and above the plane of the paper, respectively [30].

With these successive displacements, the fcc lattice is reported to be sheared by approximately 19.5°. This transformation corresponds to the relation $(111)_{fcc}//(0001)_{hcp}$, $[11\bar{2}]_{fcc}//[1\bar{1}00]_{hcp}$, called the Shoji-Nishiyama relation [30].

The generation of hcp martensite is also considered as a stacking fault formation. According to Olson and Cohen the fault energy, γ, can be calculated according to Eq. (2-4) [36].

$$\gamma = n\rho_A(\Delta G^{chem} + E^{str}) + 2\sigma(n) \quad (2\text{-}4)$$

Here n is the thickness of the embryo in terms of the number of planes, ρ_A is the density of atoms in a close packed plane (moles/unit area), ΔG^{chem} is the chemical free energy difference between the parent and the product phases, E^{str} is the strain energy and σ(n) is the free energy per unit area of the particle/matrix interface. According to Eq. (2-4), under conditions where the volume energy change (ΔG^{chem} - E^{str}) is negative, the fault energy decreases with increasing fault thickness, n. The volume energy change will be negative when the chemical driving force is greater than the strain energy, which occurs below the equilibrium temperature T_0. When the temperature is lowered to the level of $\gamma \leq 0$, the defect becomes unstable and embryo formation can occur without a barrier.

The fault formation involves the dissociation of the dislocations into Shockley partials which reduce the total strain energy where the partials tend to repel each other. The total free energy, G(r), as a function of the dislocation separation, r, can be expressed with the Eq. (2-5).

$$G(r) = E_{\perp}(r) + \gamma.r \quad (2\text{-}5)$$

$E_{\perp}(r)$ decreases with increasing r and therefore, the counteracting force for a stable phase comes from a positive fault energy, γ. There is also an equilibrium separation of the partial dislocations, r_{eq}, where the attractive and repulsive forces are balanced. However, when $G(r) \leq 0$ the austenite phase becomes unstable and martensitic transformation can take place. The change in total free energy with increasing dislocation separation, r, as a function of fault energy, γ, is presented in Figure 2.11.

Figure 2.11 shows that for a fault energy $\gamma \leq 0$, the total free energy G(r) reduces to ≤ 0 with increasing separation distance r and the parent austenite thus becomes unstable and martensitic transformation can occur. However, for spontaneous embryo formation at $\gamma = 0$ a critical defect size, n*, has to be achieved. This can be calculated according to Eq. (2-6) at M_S.

$$n^* = \frac{2\sigma}{-\rho_A(\Delta G^{chem} + E^{str})} \tag{2-6}$$

2.1.1.2. Formation of a bcc Structure and Bain Distortion

According to Bain, a bct lattice already exists in a portion of an austenite structure, Figure 2.12. However, in order to obtain a bcc crystal (α'), this bct lattice has to be compressed in height while extended in width, Figure 2.12 [37]. This is called the Bain-distortion and it can be expressed using the lattice constants of the parent fcc (a_{fcc}) and product bcc phases (a_{bcc}) according to Eq. (2-7) and the associated volume change can be calculated using Eq. (2-8) [38, 39].

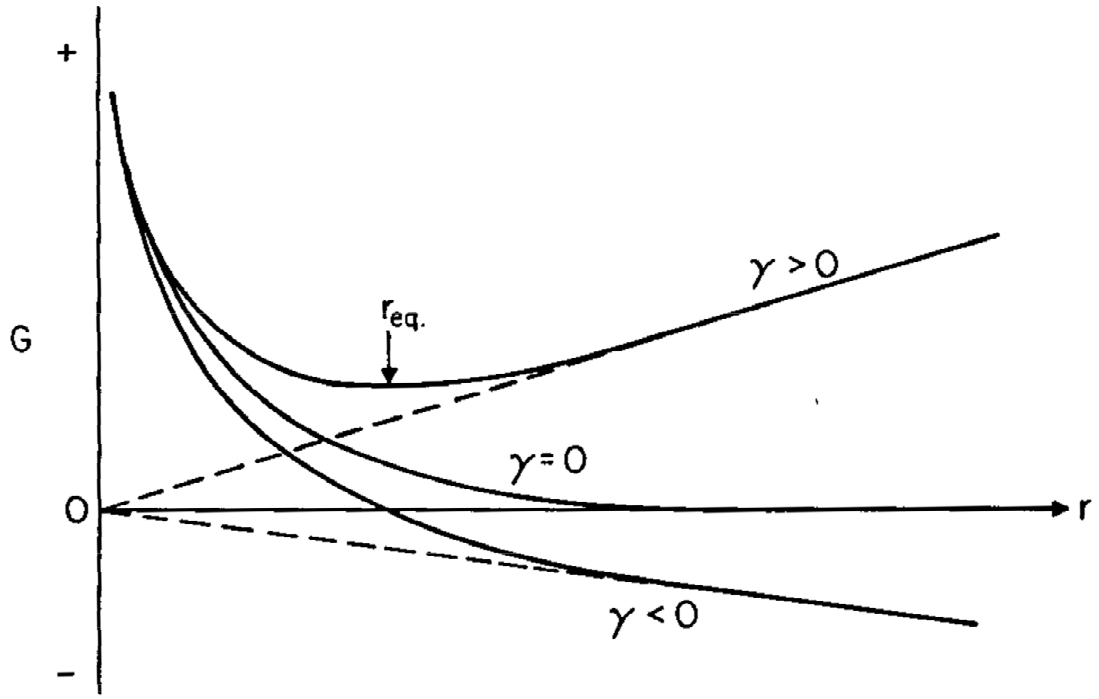

Figure 2.11. The change in chemical free energy with increasing separation distance, r, as a function of the fault energy, γ [36].

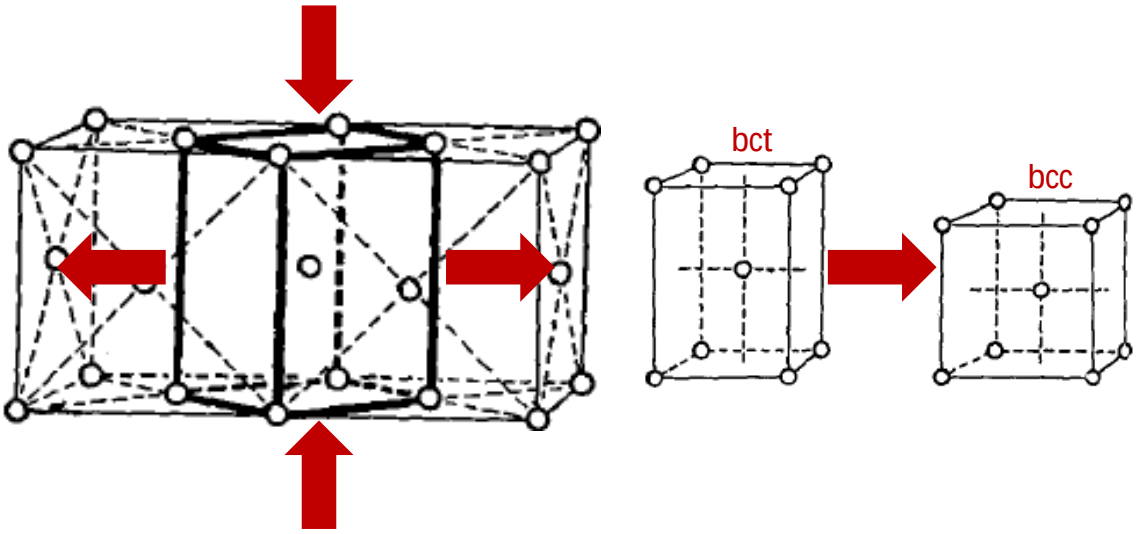

Figure 2.12. A bct lattice delineated in the fcc structure (heavy lines), and the formation of a bcc lattice from the bct lattice by contraction in the longitudinal and extension in the horizontal axes [37].

$$\underline{\underline{B}} = \begin{bmatrix} \sqrt{2}a_{bcc}/a_{fcc} & 0 & 0 \\ 0 & \sqrt{2}a_{bcc}/a_{fcc} & 0 \\ 0 & 0 & a_{bcc}/a_{fcc} \end{bmatrix} \quad (2\text{-}7)$$

$$\frac{dV}{dV_0} = \det(\underline{\underline{B}}) \quad (2\text{-}8)$$

According to Lagneborg the formation of bcc martensite is considered to be similar to the formation of hcp martensite. Where the hcp fault is formed by dissociation of the unit dislocation $(a_0/2)[101]$ into two Shockley partials $(a_0/6)[2\bar{1}1]$ and $(a_0/6)[112]$; the bcc fault is formed by the dissociation of a Shockley partial $(a_0/6)[2\bar{1}1]$ into two half Shockley partials $(a_0/12)[2\bar{1}1]$ and $(a_0/12)[2\bar{1}1]$ [40]. Accordingly, the atomic configuration in the middle of a Shockley partial resembles that of a bcc lattice, Figure 2.13. Therefore in these partials, volumes of martensite exists and the more stable the martensite than the austenite, the larger the width of these layers would grow. These plates are essentially bct in nature but can be transferred to bcc with some distortion which corresponds to (e_1,e_2,e_3) = (0.082, 0.082, -0.117), i.e., extension along the width and compression along the height of the crystal similar to the mechanism proposed by Bain; in the 18 %Ni, 8% Cr steel they studied.

2.2. Transformation Induced Plasticity (TRIP)

When the transformation is strain induced, the gradual transformation through deformation brings forth the TRansformation Induced Plasticity (TRIP) effect. The TRIP effect helps to increase the ductility while maintaining high strength as the harder bcc/bct martensite phases act as barriers to dislocation motion during straining which results in

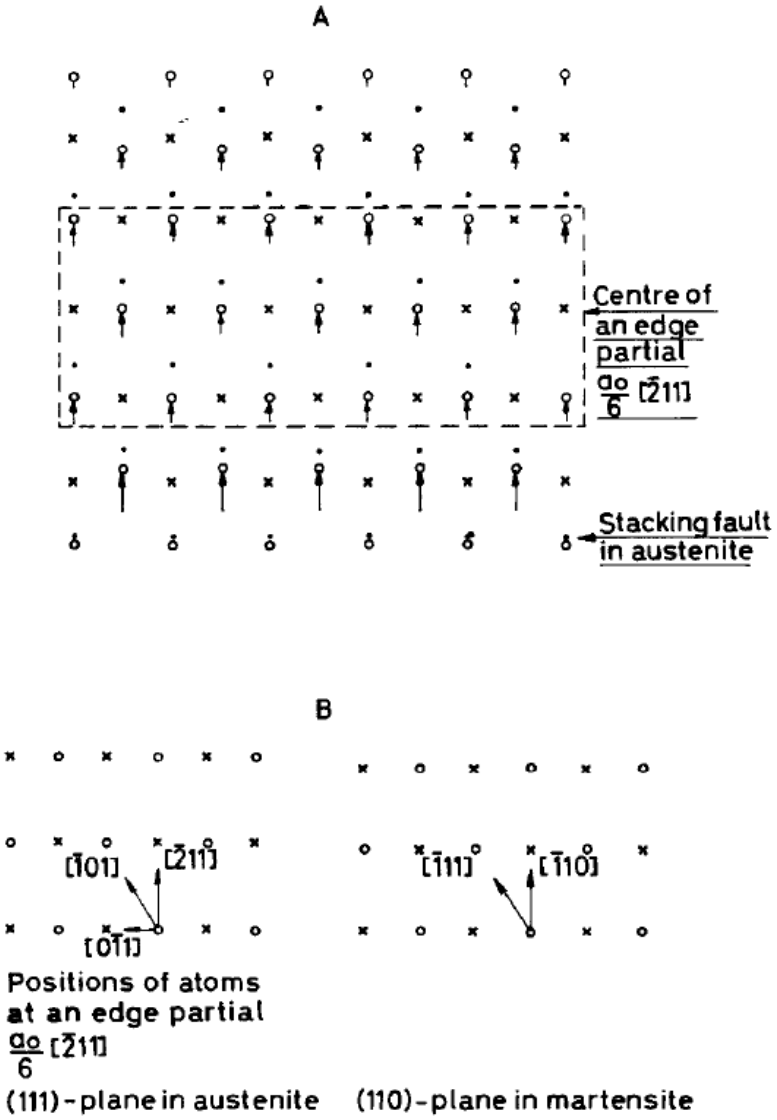

Figure 2.13. A) Position of the atoms in a Shockley partial of an edge dislocation: ·, x and o resemble the lower, intermediate and upper (111) planes. B) conversion of the martensite-like layer in the partial dislocation to a bcc martensite lattice [40].

increased strain hardening of the parent fcc austenite [9]. This phenomenon also prevents early material failure since the transformation occurs more readily at locations with the highest strain concentration. The martensite phase itself also deforms to produce greater elongation. However, for enhanced ductility gradual introduction of the martensite is essential because otherwise only the yield strength will increase if the transformation is very rapid [9, 10].

An example of how the martensite shares the load is illustrated in Figure 2.14 from the work of Tao et al. [41] where martensitic transformation results in changes in load sharing between the parent and the product phases. It can be observed that bcc phase starts to bear more load (lattice strain) with increasing applied stresses thereby playing an important role in the alloy's strengthening.

Because of these qualities, the formability of TRIP steels is greatly increased which allows them to be processed into more complex shapes during manufacturing. They are also popular in the automotive industry due to the damage absorption capabilities that comes with unique combination of high strength and ductility. Overall, as a result of these extraordinary features, the fundamental understanding of the TRIP behavior and practical applications of TRIP and TRIP-assisted steels have been of significant interest [13-15, 41-48]. As a result, the TRIP behavior, in general, is fairly well understood under the uniaxial deformation conditions such as tension or compression [2, 3, 13, 40, 49-51]. For example, Angel conducted tensile tests using a metastable 18/8 grade austenitic steel under a range of temperatures (ambient and sub-ambient) showing that the martensitic transformation increases with increasing strains

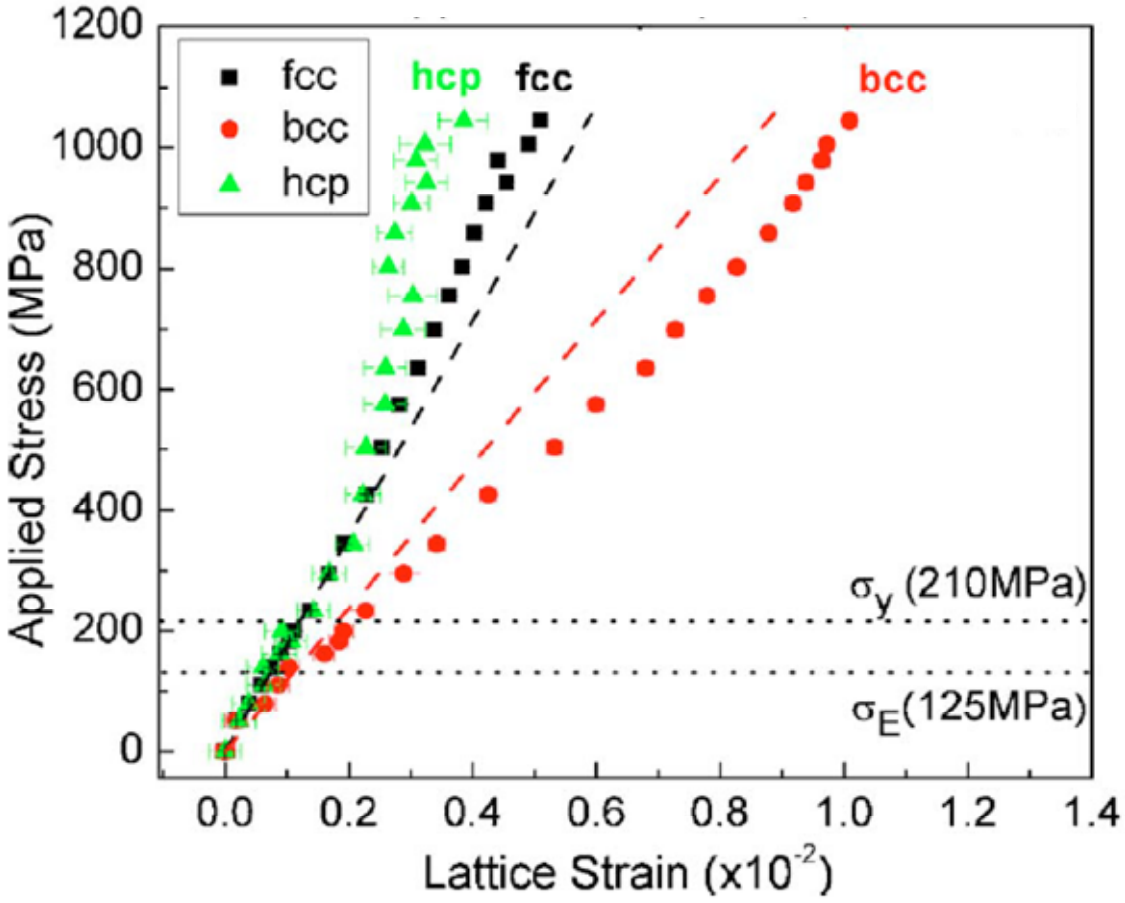

Figure 2.14. Applied Stress-Lattice Strain relation showing the load partitioning between the constituent phases: parent fcc austenite and product hcp and bcc martensites [41].

and decreasing deformation temperatures where the latter also increases the transformation rate [2]. The impact that the temperature levels have on the transformation behavior can be better explained using Figure 2.15 from this work [2], which presents the relation of applied strains with the martensitic transformation as a function of different temperatures ranging from 80 ^{o}C to -188 ^{o}C. As the figure reveals, regardless of the temperature, the martensite amount increases with increasing strain levels. Moreover, for a given strain level the transformation becomes more rapid as the temperature is reduced. This, however, is not always beneficial since the ductility is lost at the expense of increased yield strength as the martensite is introduced as a burst instead of being gradual.

Similar behavior was later observed by Hecker et al. for the 304 austenitic stainless steel deformed under tension at a temperature range of -80^{o} C and 50^{o} C [3]. For the case of compression, Tao et al. [13] conducted an in-situ neutron diffraction study at both ambient and sub-ambient temperatures using a 304L stainless steel, where measurable transformation was observed only at sub-ambient temperatures, Figures 2.16 and 2.17. Figure 2.16 shows the diffraction patterns from a) axial and b) transverse directions recorded in-situ during compressive deformation at room temperature to a strain of 11.3% true strain; with no sign of transformation as only reflections from the parent austenite phase are observed. The very weak hcp peak detected in the transverse direction was reported to be possibly inherited from the as-received material due to not having a complete reverse transformation during the austenitization treatment post-forming.

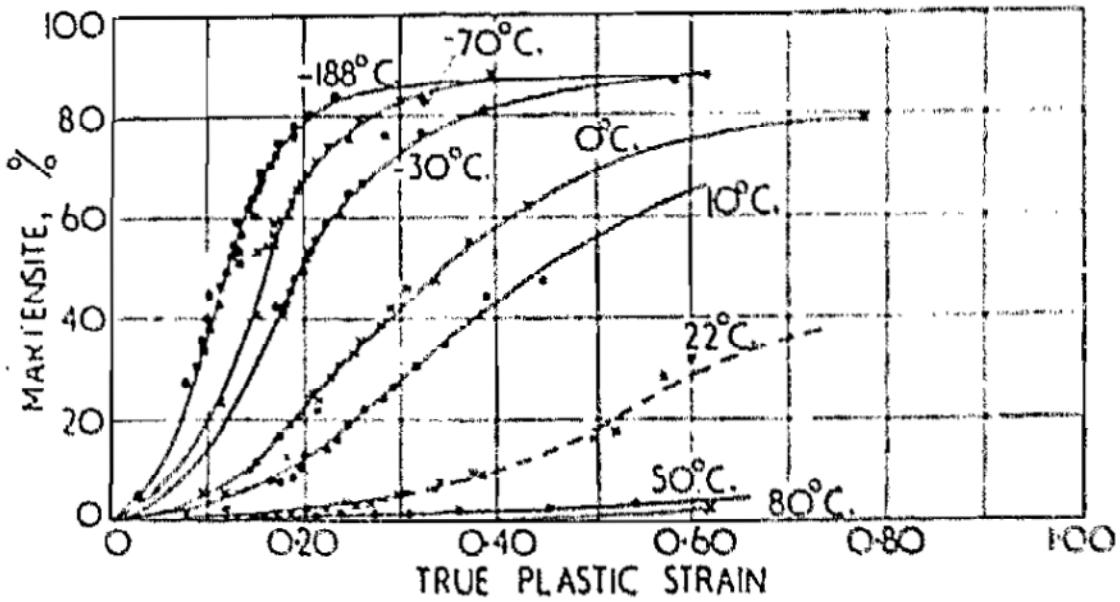

Figure 2.15. Strain-induced martensite formation as a function of temperature [2].

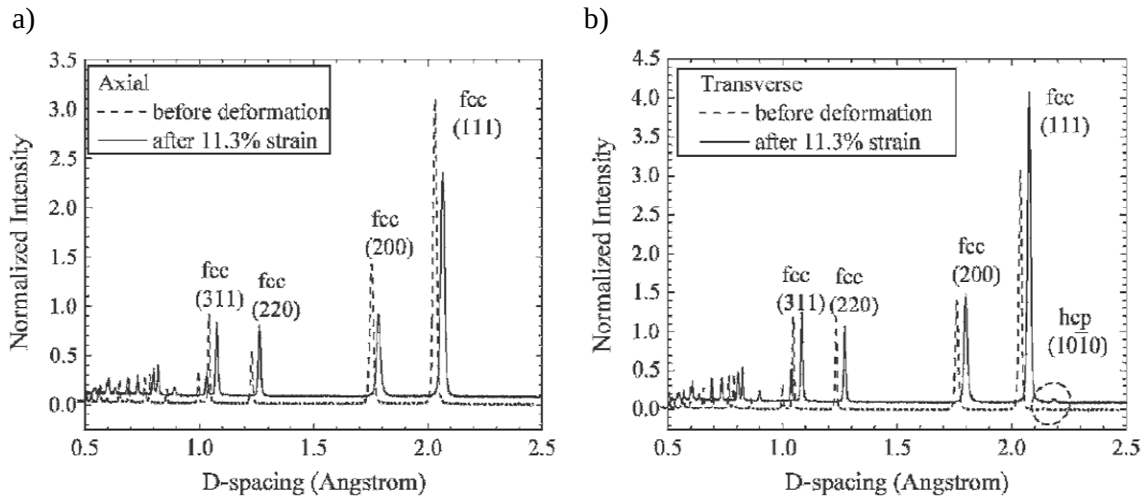

Figure 2.16. Diffraction patterns recorded in-situ during compressive deformation of 304L stainless steel at room temperature to 11.3% strain: a) in the axial direction and b) in the transverse direction. The pattern recorded at zero load is superimposed offset, for comparison [13].

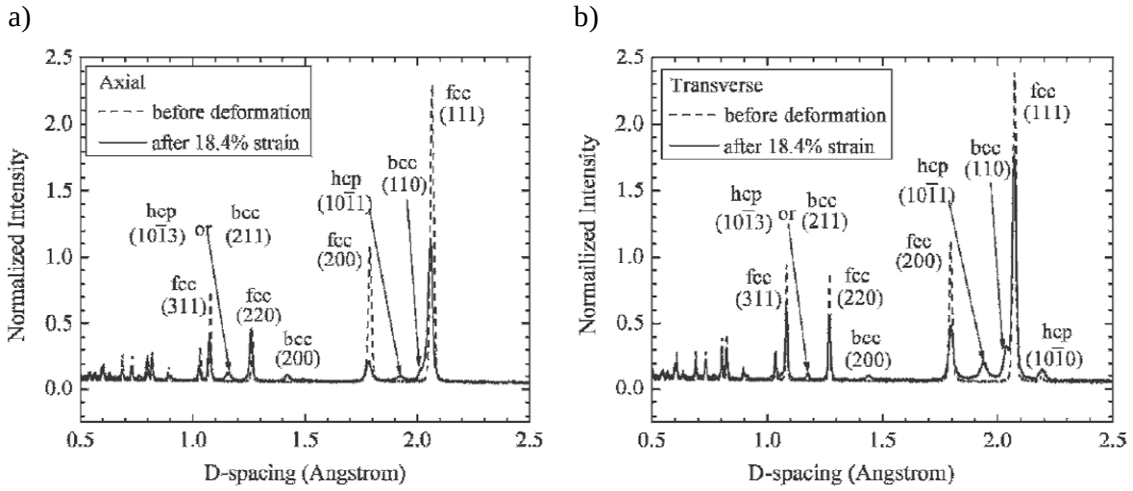

Figure 2.17. Diffraction patterns recorded in-situ during compressive deformation of 304L stainless steel at 203K to 18.4% strain: a) in the axial direction and b) in the transverse direction. The pattern recorded at zero load is superimposed for comparison [13].

On the other hand, in Figure 2.17 the in-situ recorded diffraction patterns for a sample deformed at -70 ^{o}C is presented where transformation to martensite is clearly visible.

Moreover, there are a number of recent studies focusing on the TRIP-assisted steel grades with multiple phases in the starting microstructure, e.g., a ferritic matrix and a dispersion of bainite, martensite, and retained austenite grains [42, 44, 45, 47]. The high strength of these steels is obtained by the combined strain-hardening of the ferrite, bainite and deformation-induced martensite phases. The strength depends primarily on the high yield strength of bainite and martensite phases. An SEM micrograph of the initial microstructure of a TRIP-assisted steel (TRIP 800) is presented in Figure 2.18. It can be observed that the material consists of a ferritic (F) matrix with retained austenite (A) and bainite (B) phases dispersed in it [45]. As the deformation takes place, martensite forms in the retained austenite grains with increasing strains as illustrated in the TEM micrograph from the work of Cheng et al [44], Figure 2.19.

In addition to the hardening supplied by the transformation of the retained austenite to martensite, another hardening mechanism is also effective in the TRIP-assisted steels. The martensitic transformation is accompanied by a volume increase which then results in the introduction of additional dislocations into the ferrite grains adjacent to the retained austenite; causing additional strain hardening [10, 44, 52]. Therefore, stress partitioning between these phases becomes a complex issue when the martensite is introduced.

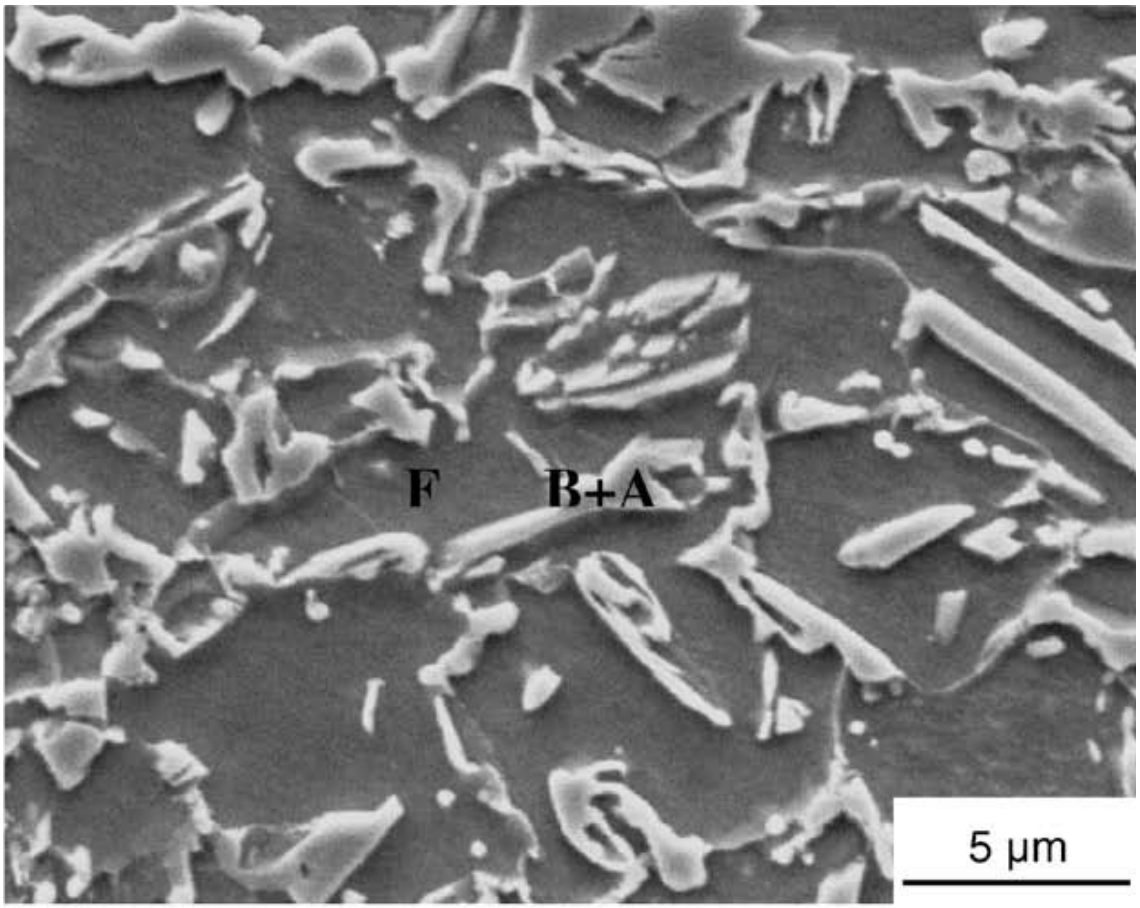

Figure 2.18. An SEM micrograph showing the microstructure in a TRIP-assisted steel (TRIP 800) consisting of a ferritic matrix (F) with Bainite (B) and Retained Austenite (A) phases embedded [45].

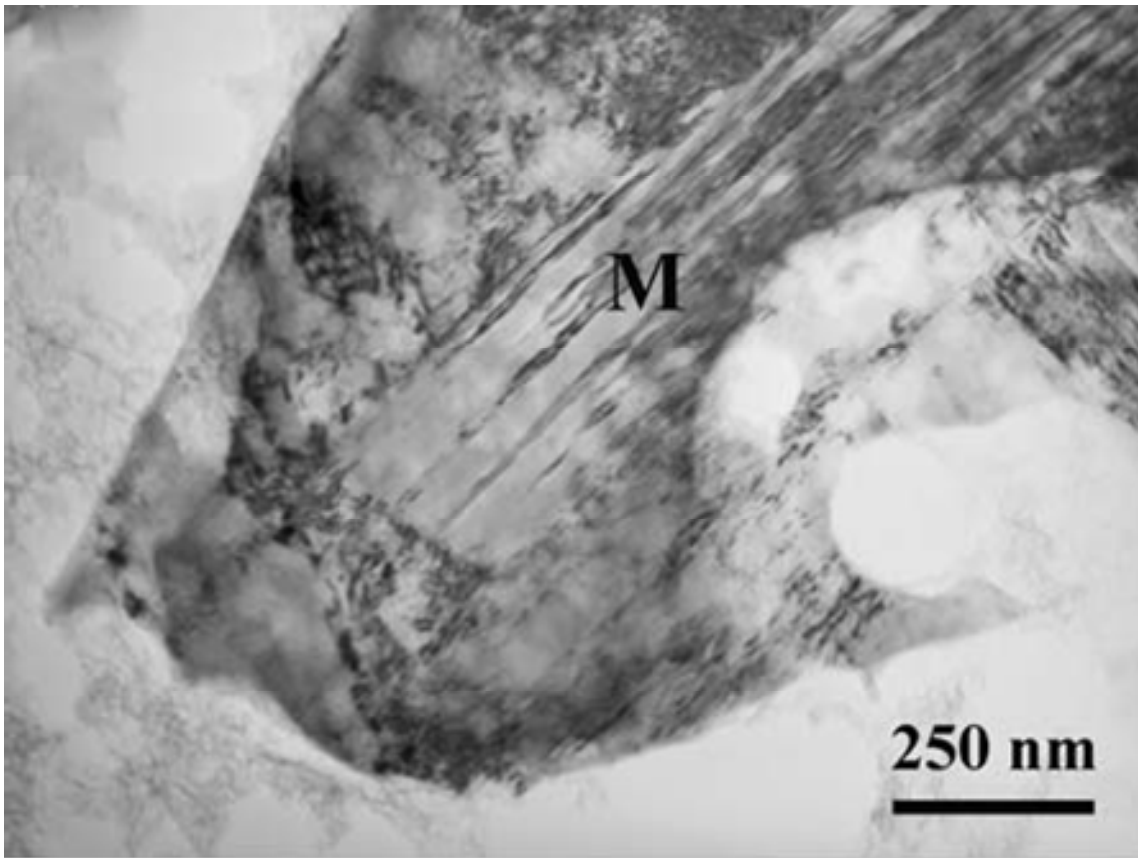

Figure 2.19. TEM micrograph showing the formation of needle-like Martensite (M) phase within the retained austenite grains [44].

2.3. Other Factors Affecting the Transformation Behavior

2.3.1. Stacking Faults and the Effect of Stacking Fault Energy

In an fcc structure the stacking sequence of atoms is given by ABC ABC ABC [53]. An fcc type stacking is illustrated in Figure 2.20a. If in the fcc packing, Figure 2.20a, the mth layer is A and the (m+1)th layer is B, slip on the (111) plane can shift the atomic arrangements above the mth layer as shown in Figure 2.20b. This creates a stacking fault between the mth and the (m+1)th layer and the resulting stacking sequence changes to AC AC in this interval creating an hcp type stacking [54]. An actual stacking fault formed during deformation of a stainless steel alloy, observed with TEM is also presented in Figure 2.21 [32].

The term stacking fault energy (SFE) defines the energy per unit area required to produce the fault [55]. SFE is one of the most important material parameters governing the material behavior and is basically determined by the composition (electron/atom ratio) and temperature [56]. For instance, the SFE of an fcc metal can critically affect its deformation behavior in terms of the active mechanisms [34, 53]; work hardening rate, fatigue and creep behavior, stress-corrosion cracking, etc [57].

According to the dislocation theory a stacking fault in an fcc structure is an extended dislocation housing a thin hcp region bounded by partial dislocations. To explain, a dislocation with a burgers vector b1 can be dissociated into two partials with burgers vectors b2 and b3, Figure 2.22. The combination of the two partials denoted with AC and AD in Figure 2.22 is known as an extended dislocation. The region between them is a stacking fault which represents a part of the crystal that has undergone slip

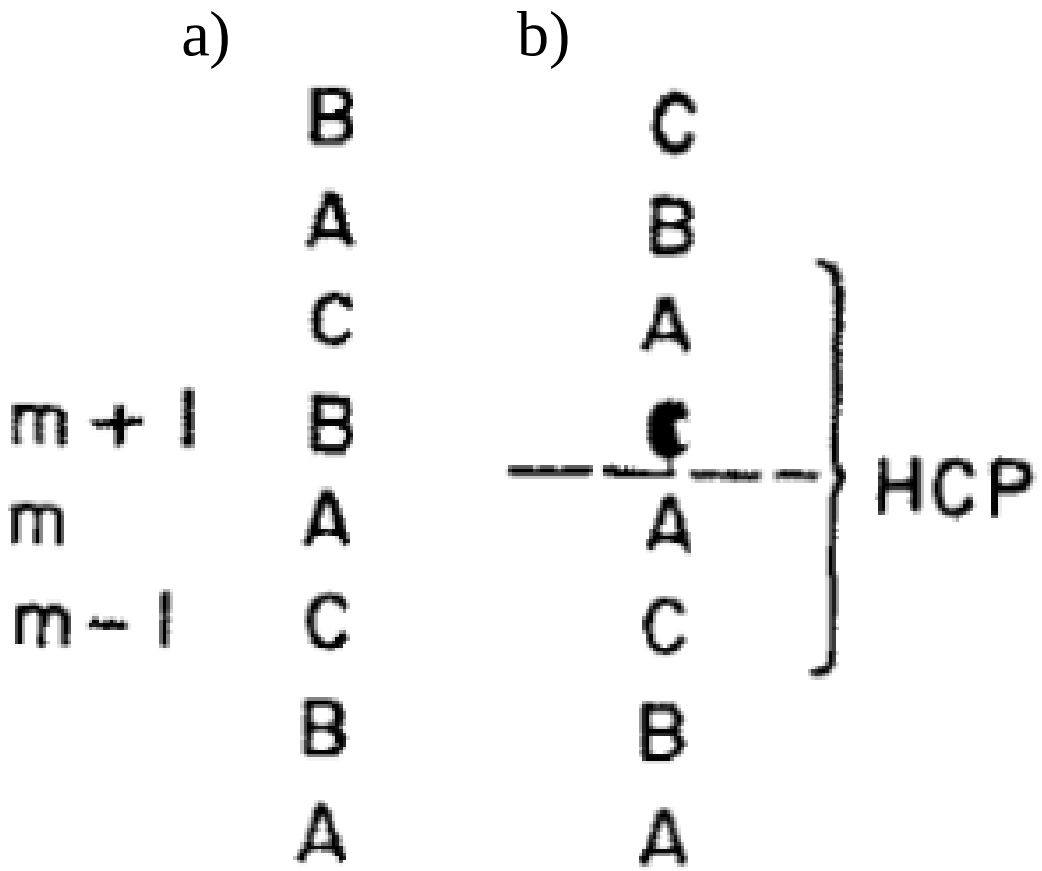

Figure 2.20. a) Illustration of an fcc type stacking and b) formation of stacking faults generating segments of hcp type stacking inside the fcc structure [54].

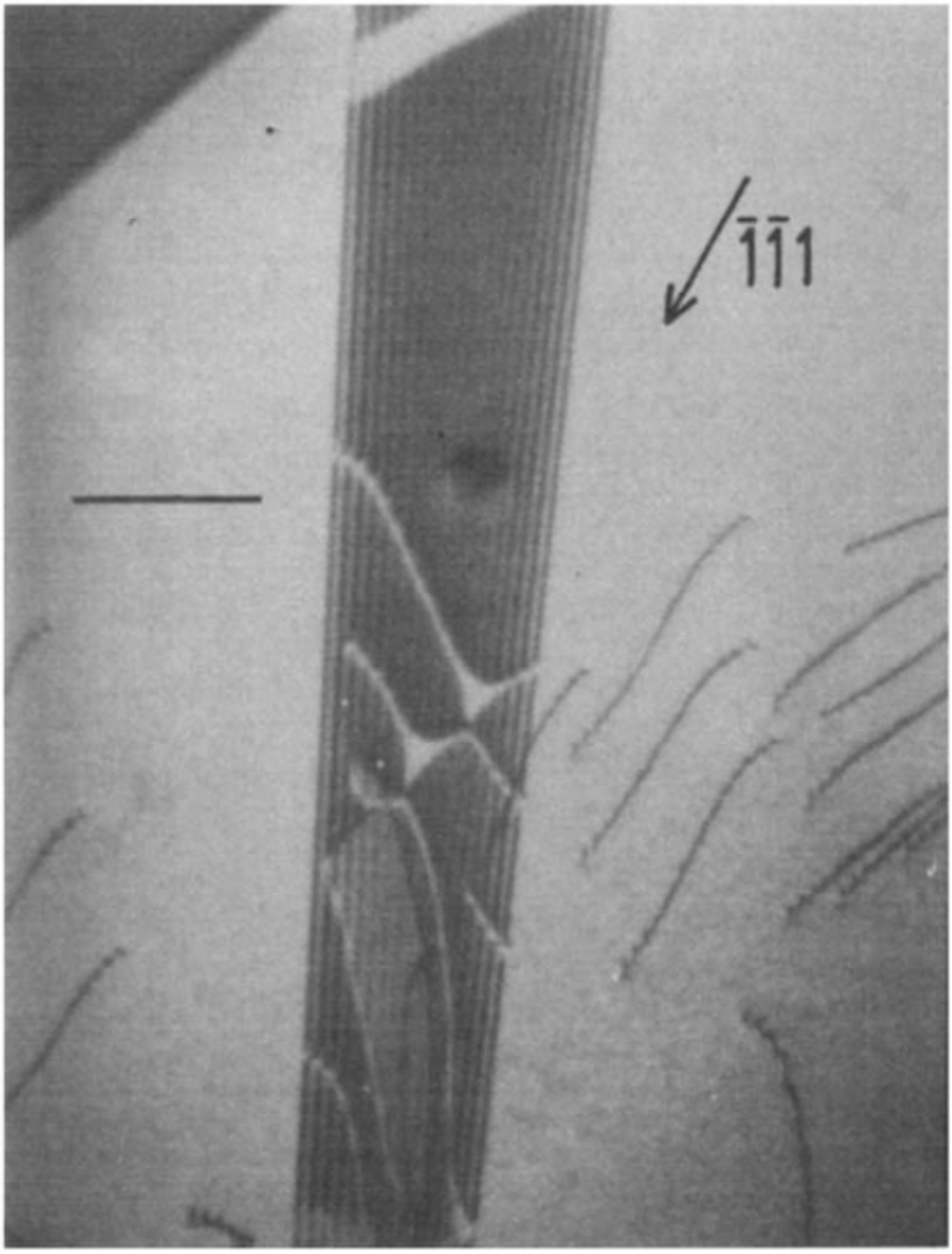

Figure 2.21. TEM micrograph showing stacking fault formed on (111) during deformation in a stainless steel [32].

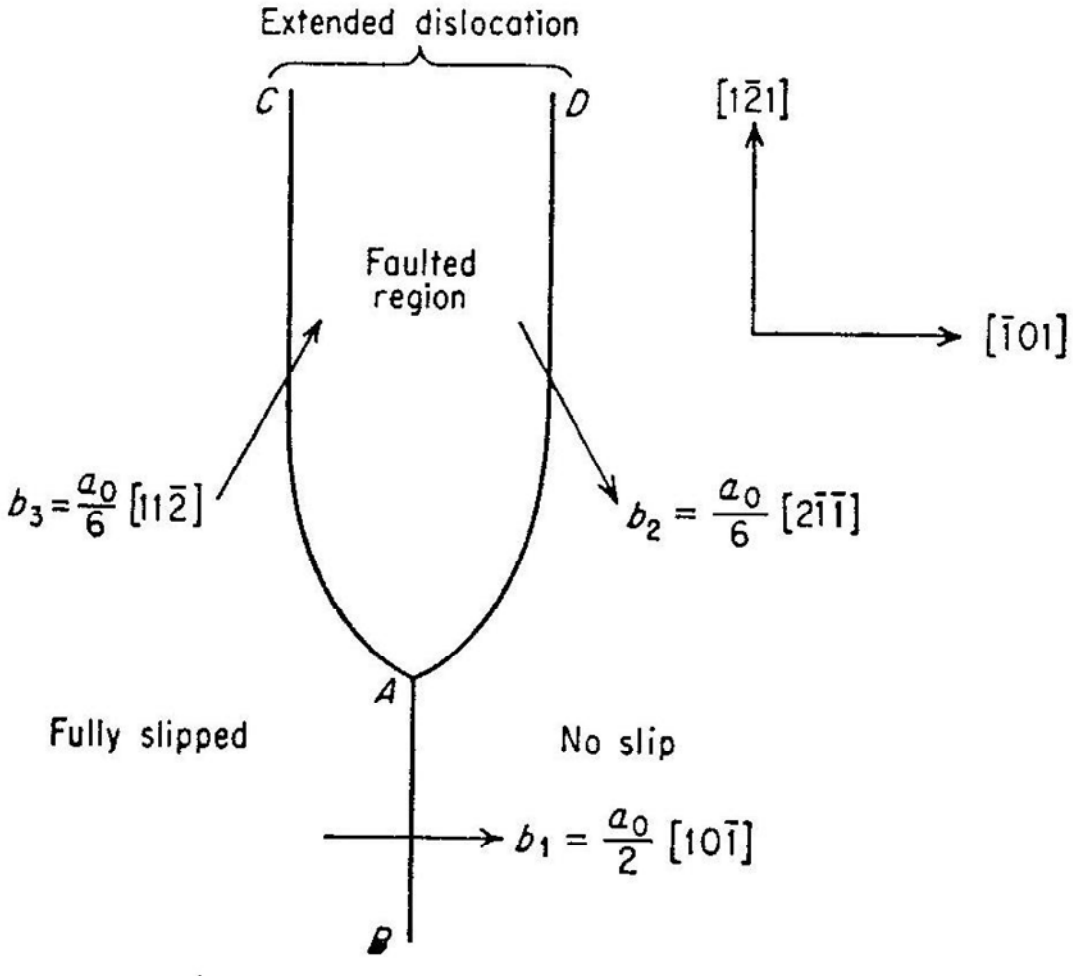

Figure 2.22. Dissociation of a dislocation with Burgers vector b1 into two partial dislocations with Burgers vectors b2 and b3; and the generation of a stacking fault between the partials [53].

intermediate between full slip and no slip. The partial dislocations will repel each other which is counteracted by the surface tension of the stacking fault as a result of which they will settle at an equilibrium separation determined by the SFE [53].

SFE has a strong influence on the dislocation movements such as cross-slip and dislocation climb. In low SFE fcc materials dislocation mobility is low and therefore processes like cross-slip and climb are difficult [58]. For instance, the partial dislocations move together with the faulted region and because of this restriction to a specific plane, partial screw dislocations cannot cross-slip unless the partials recombine into a perfect dislocation. Constrictions in the stacking fault ribbon can also allow cross slip however it requires energy and as the stacking faults get wider, i.e., SFE goes lower, it becomes more difficult to create a constriction thereby making cross slip easier in e.g. Al (SFE~200 mJ/m^2) and harder in e.g. Cu (SFE~80 mJ/m^2) [53]. This results in a homogeneous distribution of dislocations and a high dislocation density in low SFE metals compared to the high SFE ones [58].

Furthermore, at low SFE wide dissociation of dislocations into Shockley partials can hinder dislocation glide and therefore favor mechanical twinning and martensitic transformation which are competing deformation mechanisms. As the SFE is reduced the governing deformation mechanism shifts from slip to twinning and from twinning to martensitic transformation [59]. For instance, Dumay et al. state that slight changes in SFE can alter the deformation behavior such that their $Fe_{22}Mn_{0.6}C$ fcc alloy shows twinning when the SFE is around 20 mJ/m^2 which tends to disappear at higher values of

SFE whereas becomes replaced by ε martensite platelets at lower values than 18 mJ/m^2, and by α' at values lower than 12 mJ/m^2 [60].

In terms of martensitic phase transformation, the SFE defines the stability of the parent austenite phase. As the SFE of the alloy increases, the transformation becomes harder especially at room temperature and above. In essence, small additions of alloying elements can greatly influence the SFE and thereby the martensitic phase transformation. For instance 304 grade stainless steel with a 18Cr-8Ni content would transform under strain whereas the 305 grade with a 18Cr-11Ni would hardly do so [61] where 3% Ni addition changes the SFE from 20 mJ/m^2 in 304 SS [53] to 34 mJ/m^2 in 305 SS [62]. Another example is the work of Shrinivas et al. [63] where 304 and 316 grade stainless steel alloys that are in the low and medium SFE levels respectively; were rolled to different reductions. The comparison is presented in Figure 2.23 and it is observed that for a given strain, the 304 stainless steel reveals significantly higher phase transformation amounts than the 316.

2.3.2. Effect of Strain Rate and Stress State

Strain rate and stress state are other important factors that can affect the extent of the martensitic transformation. In the work Lichtenfeld et al. [64], the effect of strain rate is investigated using a 304L stainless steel. The results are presented in Figure 2.24 and the amount of transformation is observed to decrease with increasing strain rates. This is interpreted to be due to adiabatic heating introduced by the high strain rates that presents a hindering effect on the martensitic transformation.

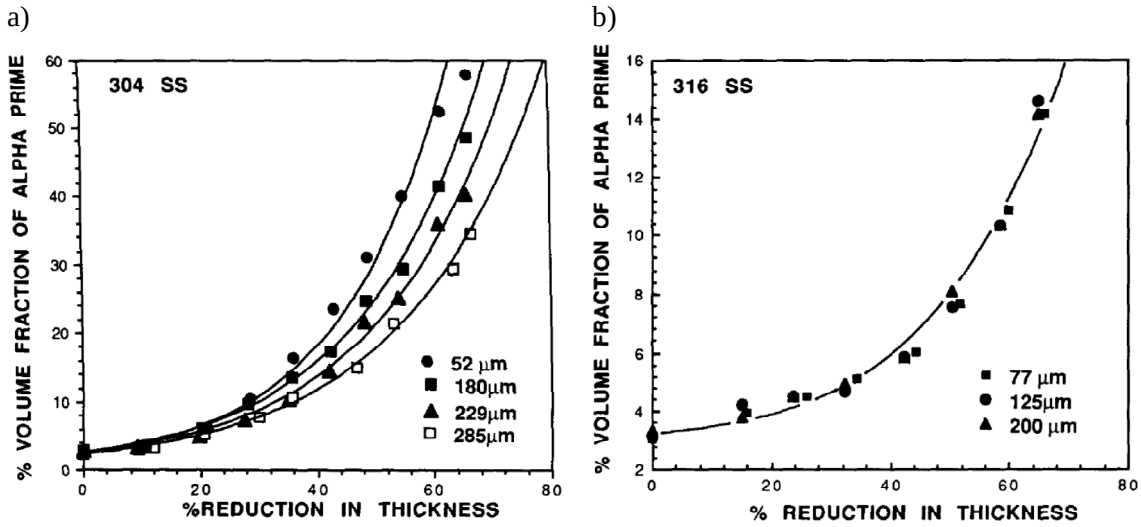

Figure 2.23. Comparison of strain-induced martensitic transformation as a function of grain size and rolling reduction for austenitic stainless steel grades a) 304 and b) 316 [63].

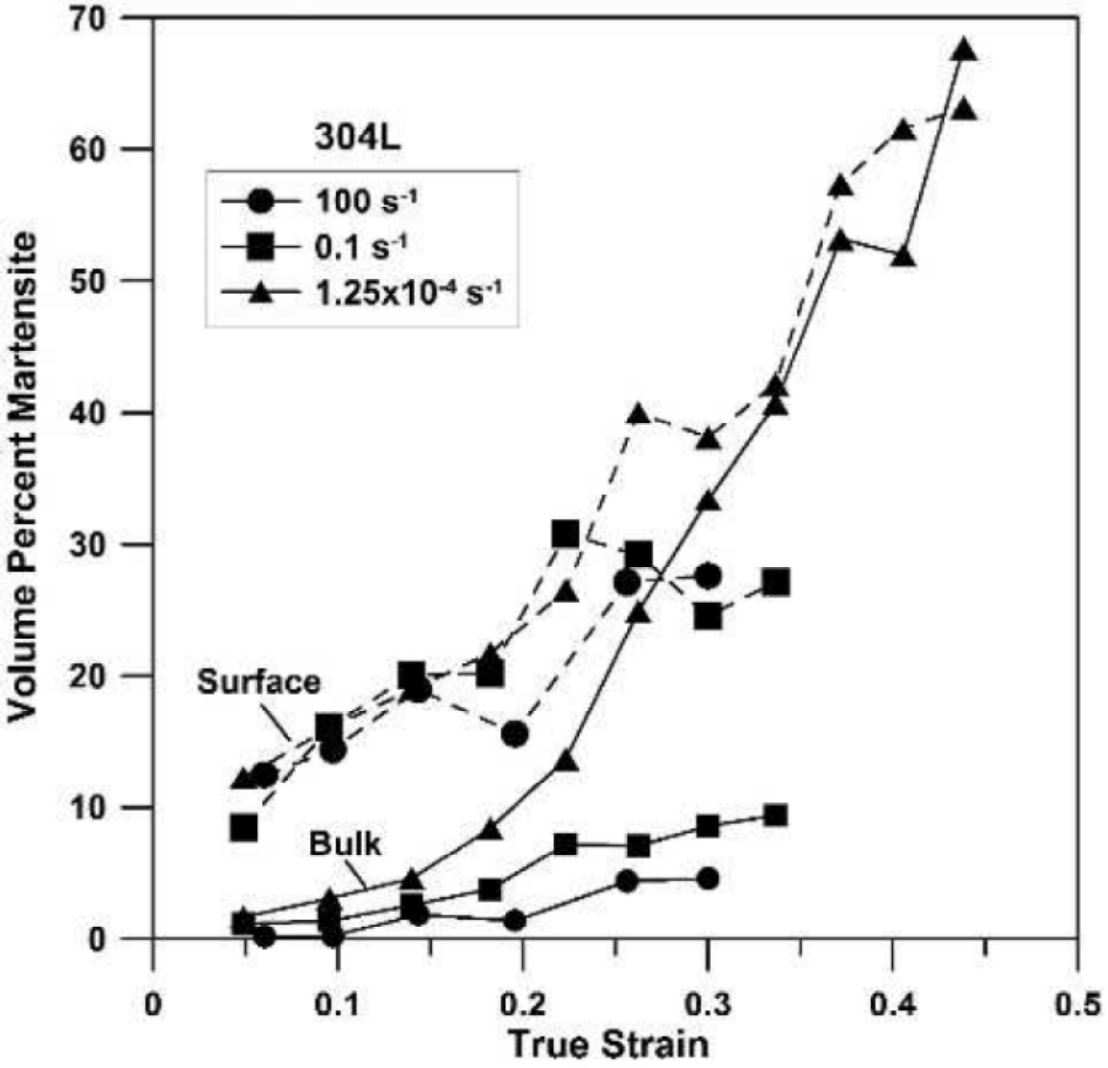

Figure 2.24. Effect of strain rate on the observed martensitic transformation in a 304L stainless steel. The results are presented for the surface and the bulk of the samples [64].

This effect is more visible in the bulk of the sample than the surface which could be related to faster cooling rates on the surface.

The effect of stress state can be presented utilizing the works of Varma et al. [65] and Shrinivas et al. [63]. In comparison to the rolling behavior of a 316 stainless steel introduced in the beginning of this section and presented in Figure 2.23 [63]; the phase transformation behavior of the same grade steel under tension was investigated in [65]. As it is presented in Figure 2.25, for the same alloys with similar grain sizes, strain-induced transformation was not observed under tension, i.e., uniaxial deformation. On the contrary, for rolling, i.e., multiaxial deformation, phase transformation took place for the same strain range studied; illustrating the importance of the strain-state on the strain-induced martensitic transformation. Furthermore, comparison of previous studies (e.g., [3, 13]) show that, for transforming austenitic stainless steels with similar compositions, tensile deformation [3] yields martensitic transformation whereas no transformation is observed under compression [13].

2.4. Torsional Deformation

Torsion test is of interest since it allows reaching high strains without inconsistencies such as necking or barreling which are commonly observed in tension and compression tests. As a mechanical testing method, the torsion test is used to determine the flow characteristics of materials at high strains and high temperatures like the ones achieved during industrial manufacturing processes such as rolling, extrusion, and

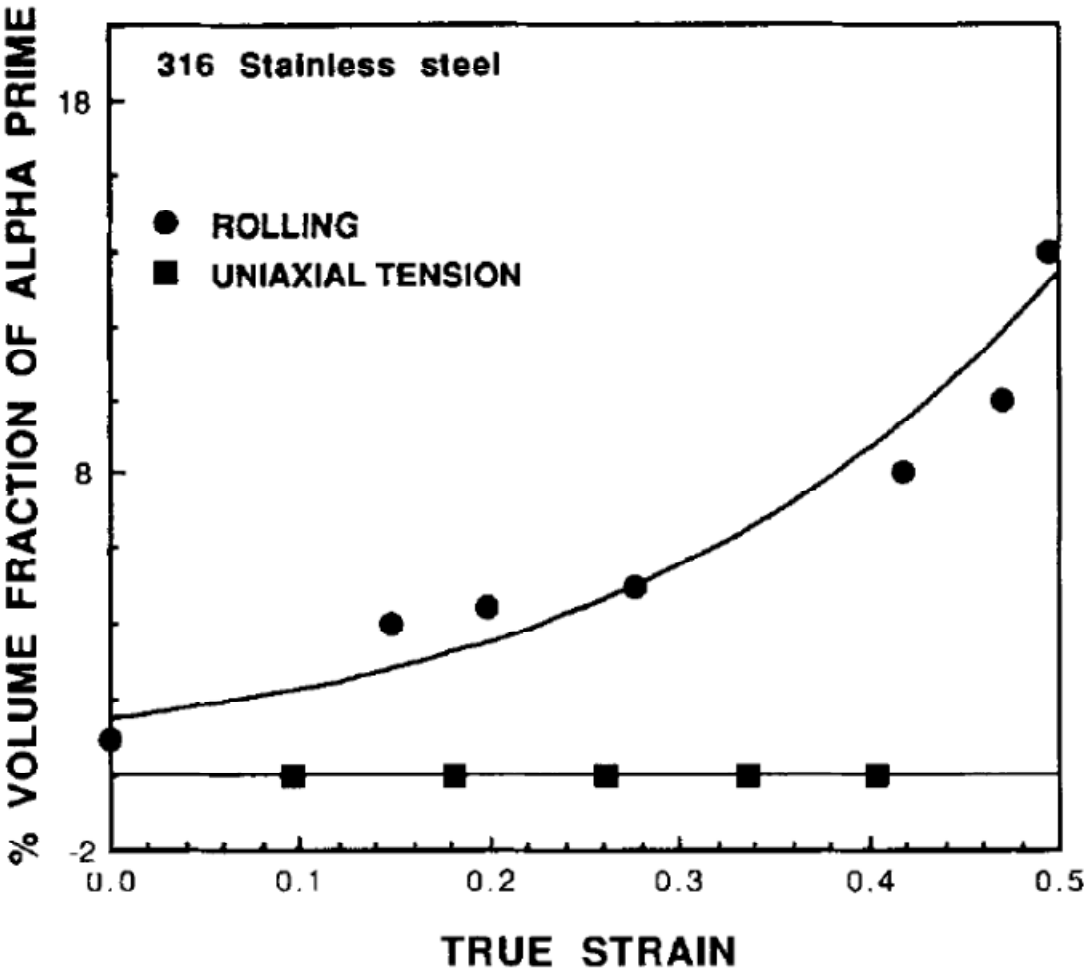

Figure 2.25. Effect of stress-state on the martensitic phase transformation in a 316 stainless steel deformed under rolling and uniaxial tension [63, 65].

forging. However, torsional deformation, overall, had not been given the same amount of attention as the simpler uniaxial deformation modes.

The stress - strain calculations for torsional deformation are not as straightforward as their uniaxial counterparts. When a solid cylindrical bar is applied torsional moment (M_T) on one end, a resisting force, i.e., the shear stress (τ) in the cross section of the bar, will counteract this, Figure 2.26. This force balance is presented in Eq. (2-9);

$$M_T = \int_{r=0}^{r=a} \tau r dA = \frac{\tau}{r} \int_0^a r^2 dA = 2\pi \int_0^a \tau r^2 dr \tag{2-9}$$

where r is the radius and r=a corresponds to the surface of the cylindrical bar [53]. The term $\int r^2 dA$ is the polar moment of inertia, J, and it is equal to $\pi D^4/32$ for a solid cylindrical specimen. Therefore, the maximum shear stress on the surface of the specimen can be expressed with Eq. (2-10).

$$\tau_{\max} = \frac{M_T r}{J} = \frac{16 M_T}{\pi D^3} \tag{2-10}$$

Again according to Figure 2.26, the shear strain, γ, can be expressed with Eq. (2-11).

$$\gamma = \tan\phi = \frac{r\theta}{L} \tag{2-11}$$

where, θ is the angle of rotation in radians, and L is the gage length. According to this relation the material is virtually strain-free in the central position (r=0).

Eq. (2-10) only applies in the elastic deformation zone where the shear stress over the cross section of the bar is linear and it does not apply when the deformation is plastic. One method of shear stress calculation in the plastic deformation zone was proposed by Nadai [66].

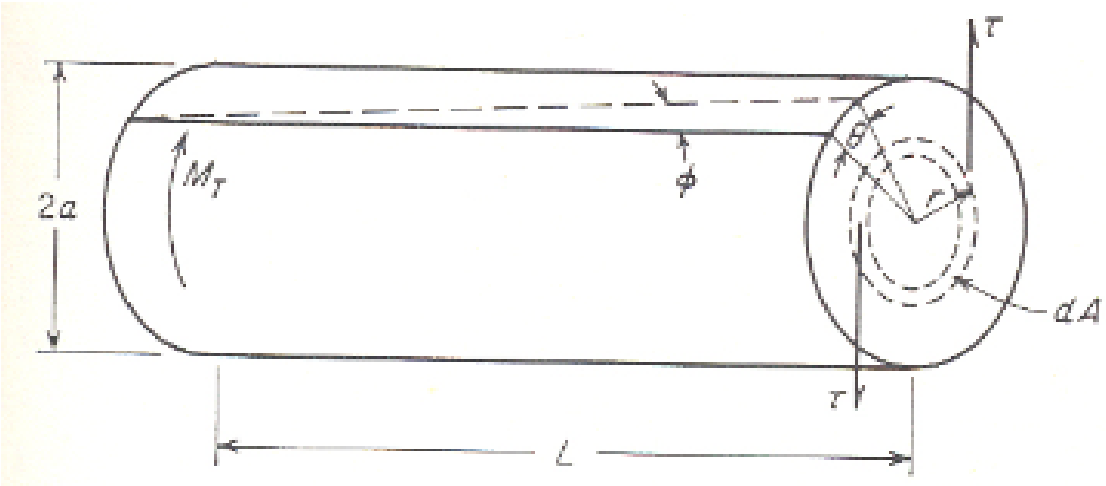

Figure 2.26. Schematic representation of a solid cylindrical bar of length, L, and diameter, 2a, subjected to torsional moment, M_T. The counteracting shear stresses, τ, at a radius, r, are also presented [53].

The shear stress is a function of the shear strain, $\tau=f(\gamma)$; and defining the shear strain as $\gamma=r\theta'$ where θ' is the angle of twist per unit length; the torsional moment in Eq. (2-9) can be redefined using Eq. (2-12).

$$M_T = \frac{2\pi}{\theta'^3}\int_0^{\gamma_a} f(\gamma)\gamma^2 d\gamma \tag{2-12}$$

Next, differentiating Eq. (2-12) with respect to θ' using $\gamma_a=a\theta'$ and $\tau_a=f(\gamma_a)=f(a\theta')$, Eq.(2-13) is obtained.

$$\frac{d}{d\theta'}(M_T\theta'^3) = 2\pi f(a\theta')a^3\theta'^2 = 2\pi a^3\theta'^2\tau_a \tag{2-13}$$

From Eq. (2-13) then Eq. (2-14) can be obtained;

$$\tau_a = \frac{1}{2\pi a^3\theta'^2}\frac{d}{d\theta'}(M_T\theta'^3) \tag{2-14}$$

where,

$$\frac{1}{\theta'^2}\frac{d}{d\theta'}(M_T\theta'^3) = \theta'\frac{dM_T}{d\theta'} + 3M_T \tag{2-15}$$

Finally combining Eq.s (2-14) and (2-15) the maximum shear stress at the surface can be defined with (2-16).

$$\tau_a = \frac{\left(\theta'\frac{dM_T}{d\theta'} + 3M_T\right)}{2\pi a^3} \tag{2-16}$$

Other than the shear strains being radial position dependent, torsional deformation has another well known peculiarity which is the length changes and the otherwise induced axial forces when the ends of the specimen are left free to move or kept fixed, respectively. The general trend is lengthening/compression at room temperature and

shortening/tension at high temperatures for free/fixed end cases [67]. The lengthening at room temperature was first introduced by Poynting [68] for small (elastic) strains and later by Swift [69] at large strains which resulted in this phenomenon to be named as the Swift Effect.

2.5. Texture Evolution

In terms of the distribution of grain orientations in a polycrystal, it is seldom that a material will have randomly distributed orientations. Instead, in most of the engineering materials the grain orientations follow a pattern that are induced by the forming/manufacturing processes such as crystallization from the melt or other thermo-mechanical processes. This pattern is known as the preferred orientation or, more generally, texture. The importance of texture arises from the fact that it affects critical properties of the material including, Young's Modulus, Poisson's ratio, strength, ductility, and toughness during and after the manufacturing processes [11].

The texture measurements have been most commonly conducted using X-ray diffraction with a special apparatus named as the texture goniometer that is used to obtain the volume fraction of a particular family of grains such as {111}, {200} etc. that are suited for diffraction. The results are presented in several generally accepted forms including the pole figures (PF), inverse pole figures (IPF), and the orientation distribution functions (ODF).

A pole figure can be used to present the distribution of a specific set of crystallographic directions relative to certain specimen directions such as rolling

direction, shear direction, and tensile direction. An inverse pole figure, on the other hand, is used to show the distribution of a selected direction in the specimen relative to the crystal axes, e.g., (100), (110), (111). Finally, an orientation distribution function shows the orientation of a given crystal relative to the sample coordinate system in a 3d space, where the coordinates are defined by three Euler angles (φ_1,ϕ,φ_2); and it is the most detailed way of representing the texture [70].

2.5.1. Typical Deformation Textures

Processes that involve the uniaxial deformation such as tension, drawing, extrusion, and rod rolling of wires or rods; the fiber textures are reported to best describe the distribution of the grain orientations. In the case of bcc metals this texture is stated to develop in the <110> axis in the direction of the extension whereas in the case of fcc there are two main fiber axes that are the <111> and <100> parallel to the axis of extension [71].

When the load direction is reversed, i.e., as the sample is compressed, the major fiber components are also switched between fcc and bcc type textures such that bcc metals tend to develop a mixture of (111) and (100) fibers whereas fcc forms the (110) type fiber texture. However, some low SFE fcc metals also show the (111) type fiber along with the (110) fiber, e.g., the 70:30 brass in which twinning is regarded as an important deformation mechanism [71]. The IPF representation of fiber textures developed under compression and tension are shown in Figures 2.27 and 2.28, respectively.

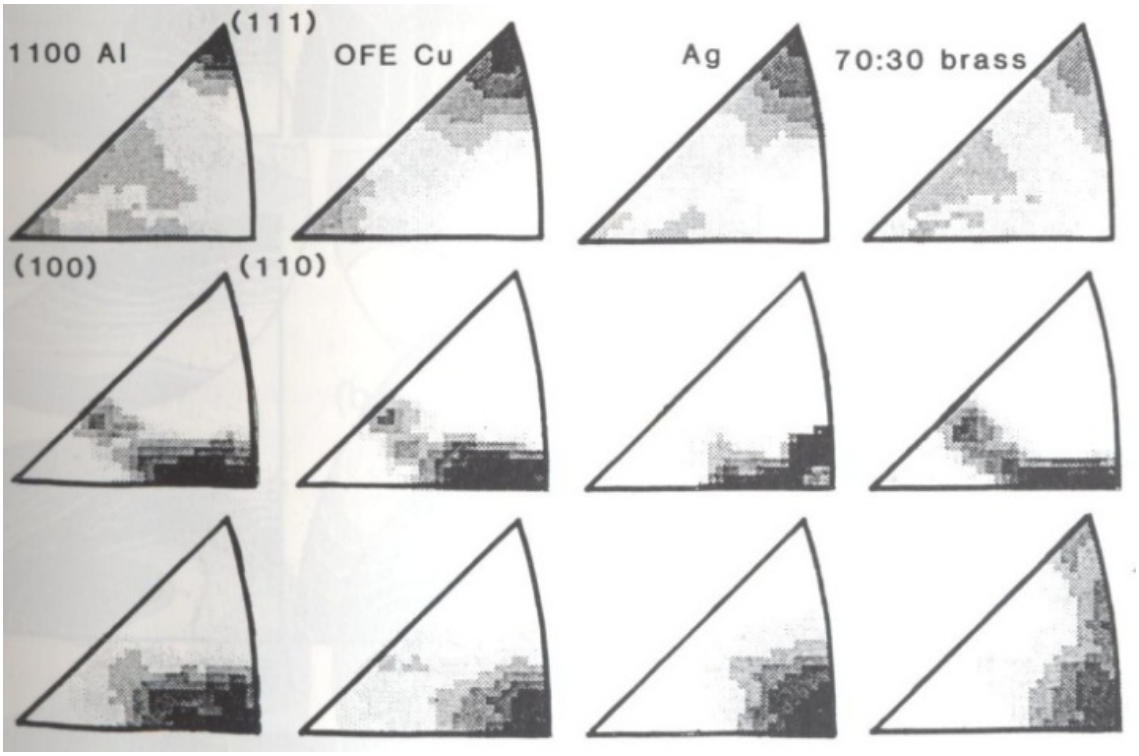

Figure 2.27. Inverse pole figures from the compression direction of several fcc materials showing the fiber texture evolution under compressive deformation: 1st Row: initial textures, 2nd Row: simulation results, 3rd Row: experimental results [72].

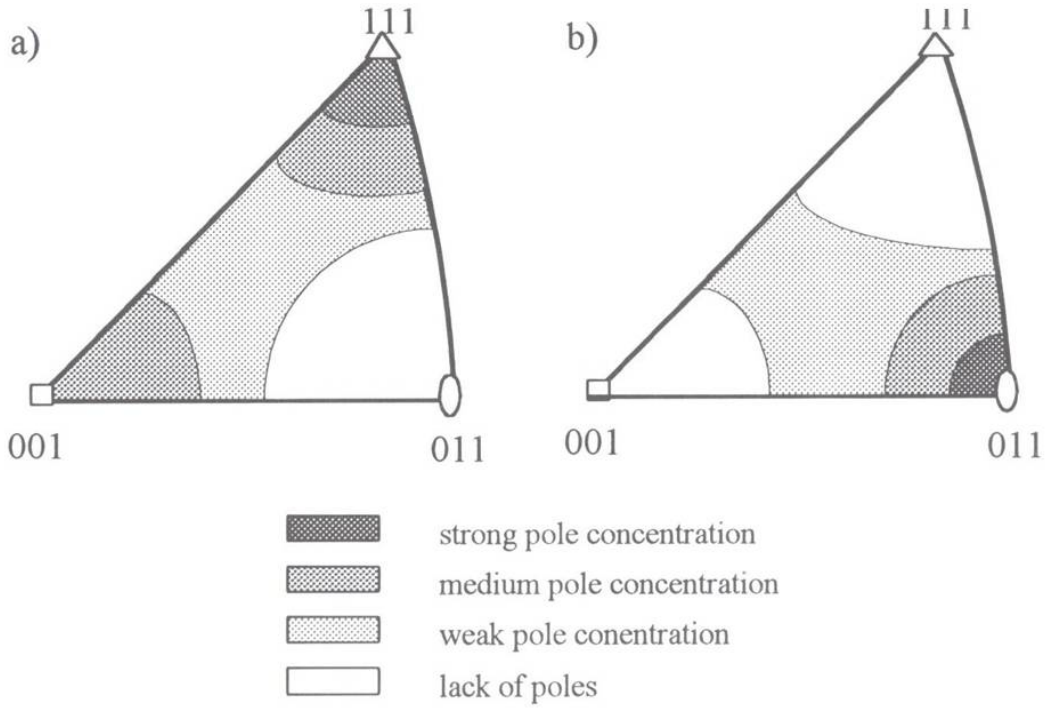

Figure 2.28. Inverse pole figures from the tensile direction showing the fiber textures for a) fcc and b) bcc metals observed under tensile deformation [73].

Figure 2.27 shows the IPFs of Al, Cu, Ag and 70:30 brass for initial textures (first row), simulated deformation behavior (second row) and the experimentally obtained textures after compression. As can be observed, consistent with the statement above, all the pure metals tend to develop a (110) type fiber texture under compression whereas, the brass additionally develops a (111) type fiber, as also stated before.

Figure 2.28 shows the IPFs for texture development under tension for a) fcc and b) bcc metals. In agreement with the previous statement, the fcc metals show a mixture of (111) and (100) fibers whereas, the bcc metals have developed a (110) type fiber texture.

Rolling is one of the most common manufacturing processes for engineering materials and produces rather more complex textures than uniaxial deformation. In the case of rolling textures the general assumption is that the texture will eventually be the same for low and high levels of rolling reduction with the exception that the texture intensities will be stronger with increasing degree of reduction [74].

Several ideal texture components are identified for both fcc and bcc materials under rolling. The major ideal texture components and their orientation relations for fcc texture evolution under rolling is presented in Figure 2.29 in terms of ODF φ_2 sections 0^o, 45^o, and 65^o [75]. These are known as the Goss (G), Brass (Bs), Copper (Cu), and S components. Bcc metals tend to develop fiber type textures during rolling [76] and several ideal components have been identified but unlike fcc components they have not been given specific names. In this work, the nomenclature given in the work by Raphanel and Van Houtte [77] for the description of ideal bcc rolling texture components is used. These components are presented in Figure 2.30 using ODF φ_1 sections of 0^o and 30^o.

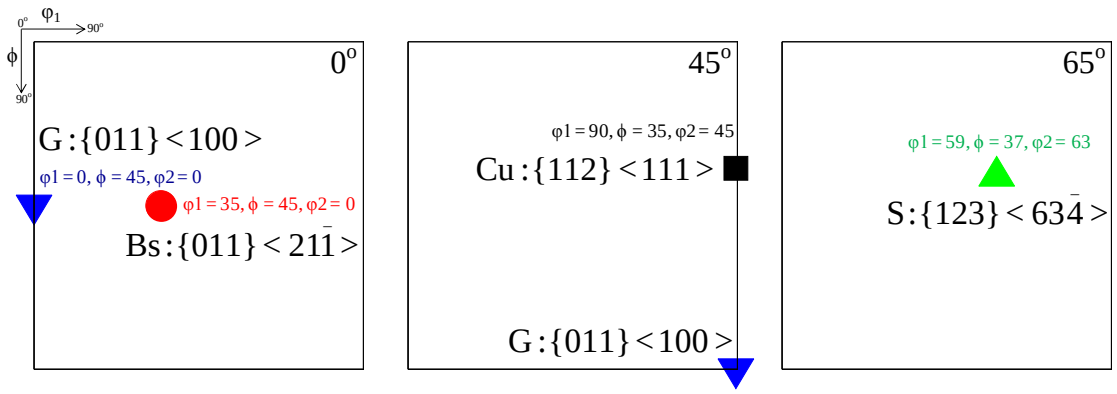

Figure 2.29. ODF φ_2 sections of 0^o, 45^o, and 65^o showing the ideal fcc rolling texture components, Goss (G), Brass (Bs), Copper (Cu), and S with their Euler angles in Bunge notation [75].

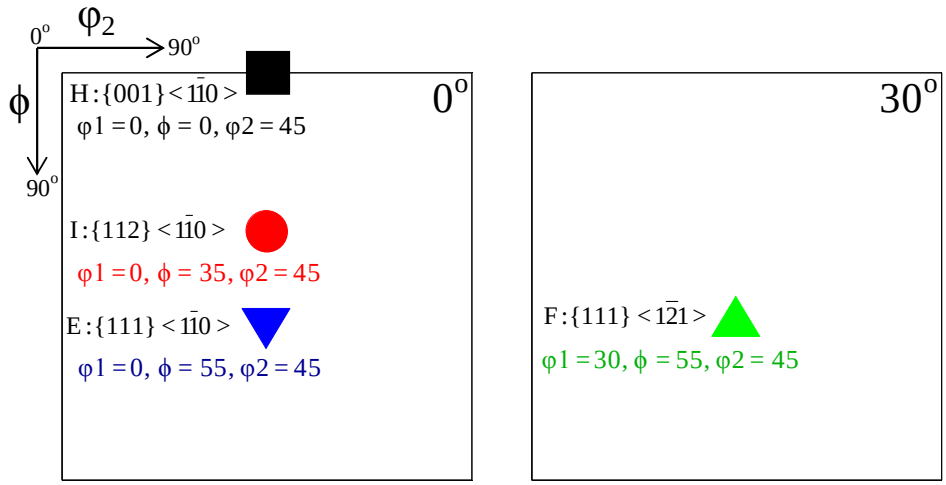

Figure 2.30. ODF φ_1 sections of 0^o and 30^o showing the ideal bcc rolling texture components, H, I, E, and F with their Euler angles in Bunge notation [77].

The two well known texture types to represent the pure metal and the alloy behavior for fcc metals under rolling are named as the copper and brass type textures respectively. The shift from copper to brass type texture is presented in Figure 2.31; which shows the (111) pole figures of Cu-Zn alloys, with increasing Zn content from a) to f); cold rolled to 96% reduction [78]. The increasing Zn content reduces the SFE and therefore results in the observed shifts in the texture evolution. Further information on the effect of SFE on texture evolution will be given in the following section. This distinction can be particularly related to the evolution of the characteristic texture components Cu and Bs. For instance, a copper type texture characterized by a very strong Cu component, is presented in Figure 2.32 from the work of Suwas et al. where pure copper was cold rolled to 90% reduction [79]. A brass (alloy) type texture on the other hand is characterized by a strong Bs component, as presented in the ODF of a 304 stainless steel in Figure 2.33 from the work of Kumar et al. [80], with the Cu component absent.

A bcc type rolling texture is presented in Figure 2.34 from the work of Raabe where the texture is characterized by a strong α fiber ranging from the H component to I and E components. The F component is also present but rather weak [81].

2.5.2. Torsion Texture Evolution

Texture evolution under torsional deformation is more complex when compared to uniaxial deformation conditions where fiber textures are generally observed [72, 73]. The main reason for this type of behavior is the high rigid body rotation rate observed

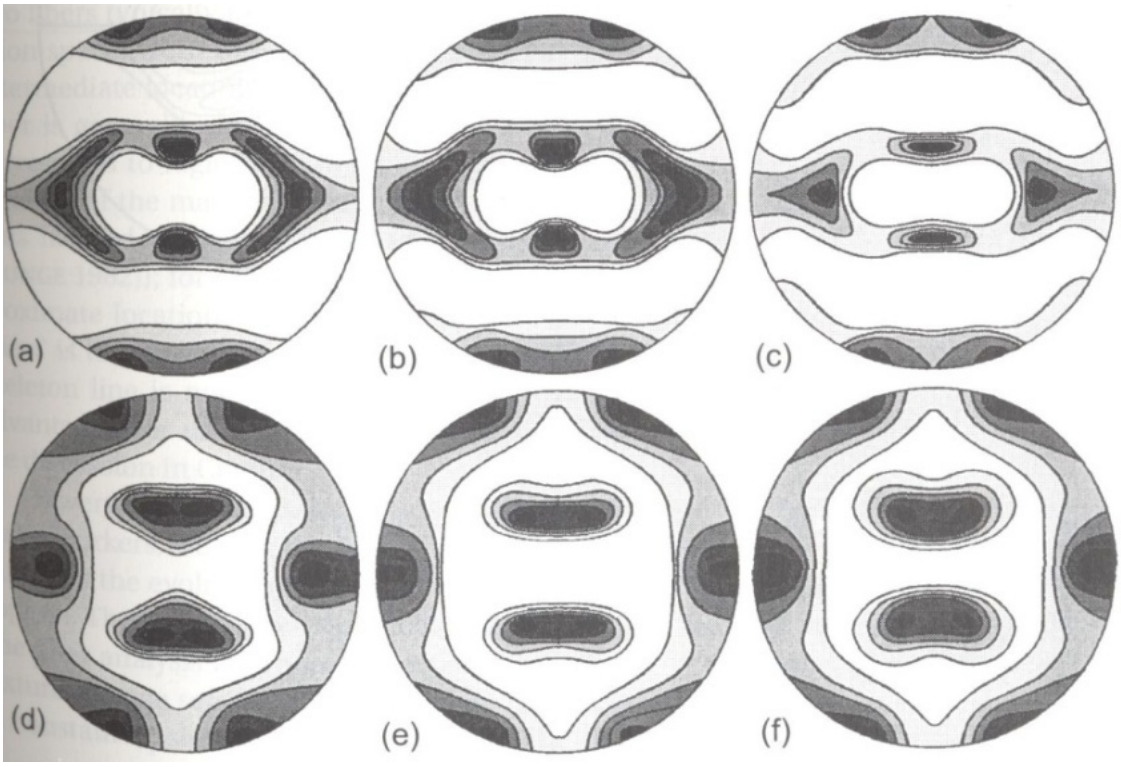

Figure 2.31. (111) pole figures for a cold rolled Cu-Zn Alloy with increasing Zn content from a) to f). The north pole denotes the rolling direction (RD) and east, the transverse direction (TD). The textures can be classified as a) Copper Type Texture, f) Brass Type Texture [78].

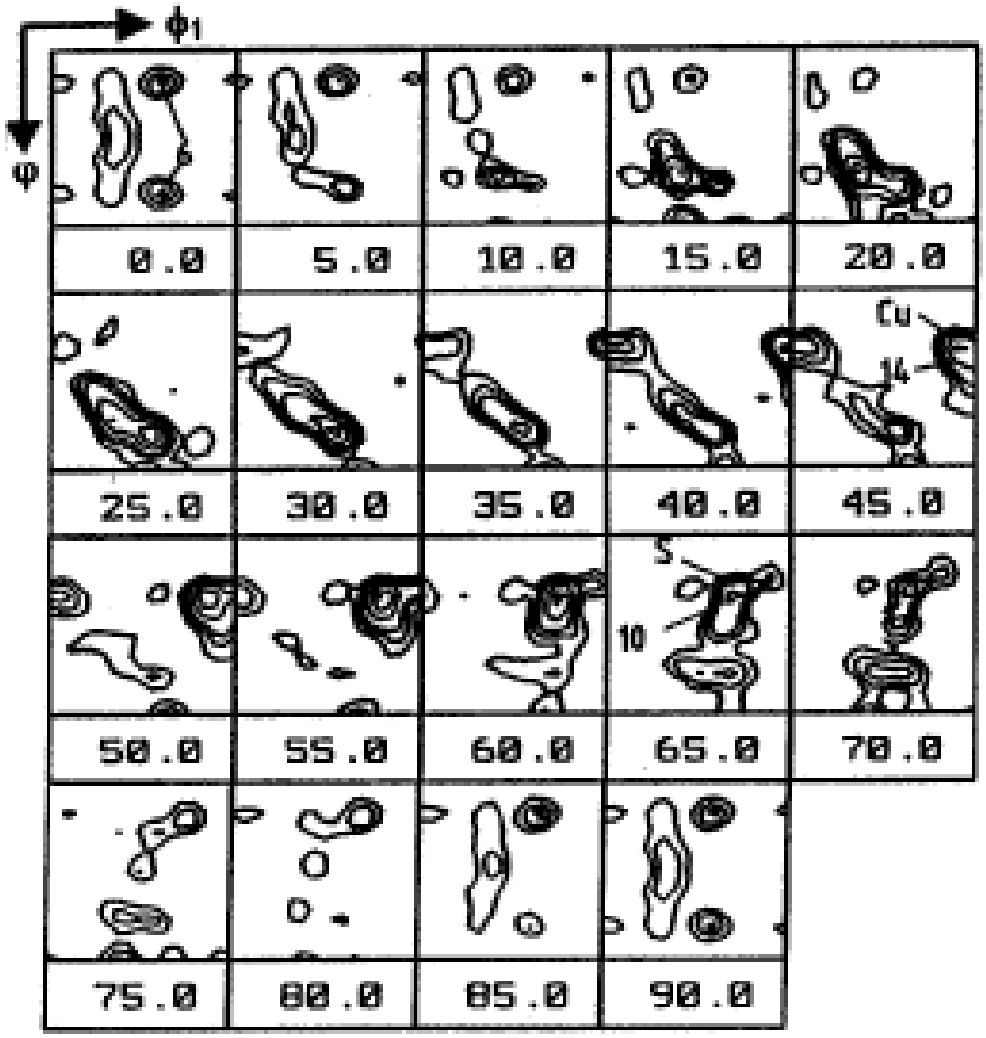

Figure 2.32. The ODF φ_2 sections (from 0^o to 90^o with 5^o intervals) of fcc pure copper rolled to 90% reduction [79].

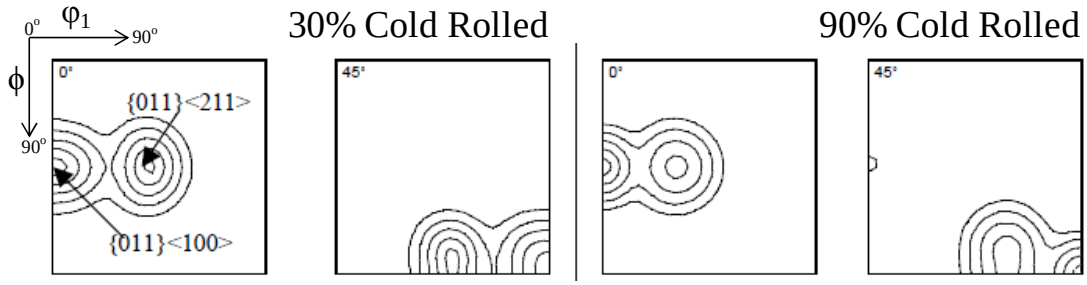

Figure 2.33. ODF sections (φ_2=0° and 45°) of an fcc 304 stainless steel cold rolled to 30% and 90% reduction, with major texture components Goss (G) {011}<100> and Brass (Bs) {011}<211> pointed out [80]. Notice that the Copper (Cu) component is missing.

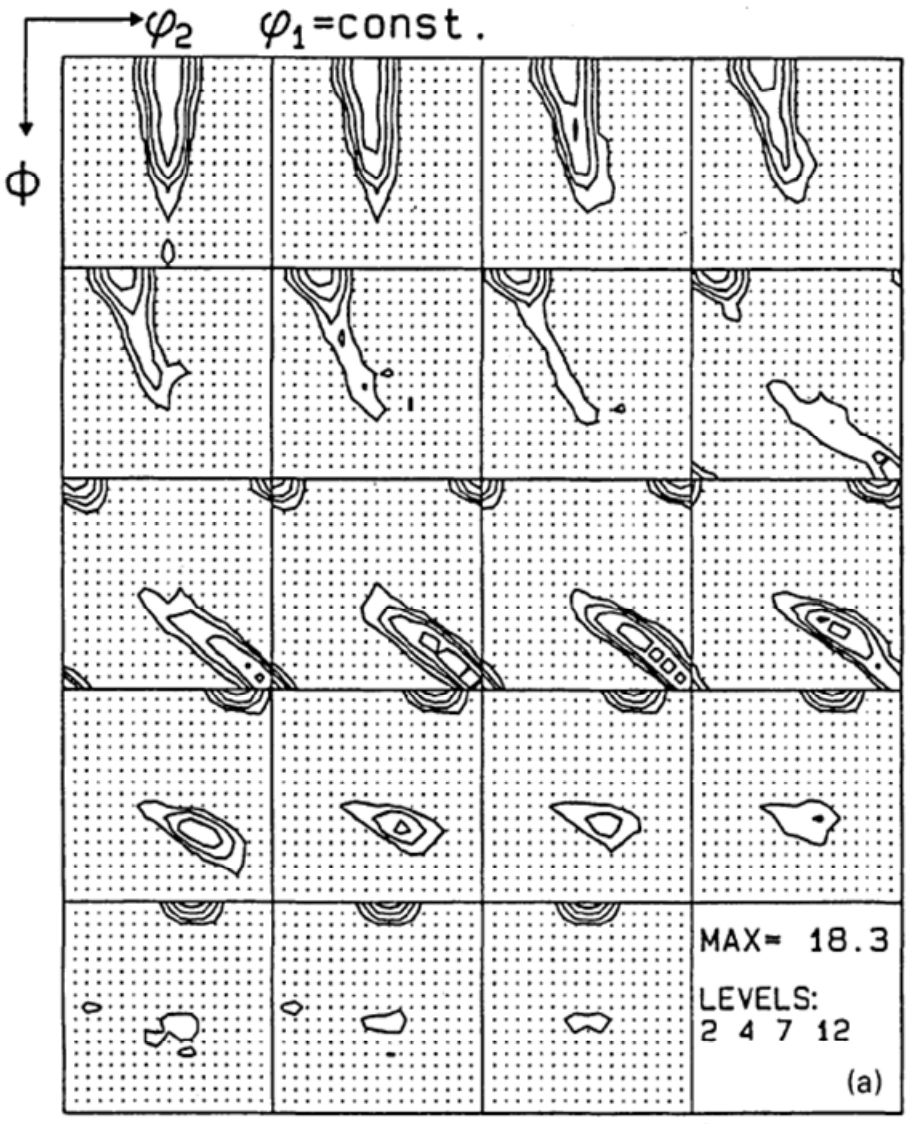

Figure 2.34. The ODF φ_1 sections (from 0^o to 90^o with 5^o intervals) of bcc Fe-11 wt.% Cr steel rolled to 70% reduction [81].

under torsional deformation as opposed to uniaxial cases [82, 83]. To explain this, first the lattice rotation rate, $\dot{\underset{\sim}{\Omega}}$ can be defined with Eq. (2-17) shown below:

$$\dot{\underset{\sim}{\Omega}} = \dot{\underset{\sim}{B}} - \dot{\underset{\sim}{\omega}} \tag{2-17}$$

where $\dot{\underset{\sim}{B}}$ is the rigid body rotation rate, and $\dot{\underset{\sim}{\omega}}$ is the glide rotation rate. For the ideal orientations $\dot{\underset{\sim}{\Omega}} = 0$ which means that the rigid body rotation rate and the glide rotation rates are equal to each other. Since the rigid body rotation rate under torsion is high, texture stability demands countervailing high glide rotation rates [83]. Therefore, unlike uniaxial deformation cases where the final textures are obtained when the glide rotation rate drops to zero, torsion textures naturally become more complex, introducing several ideal texture components instead of simple fiber textures [82]. Also, these ideal components may be stable at a given strain range but unstable at another which can result in the rotation of hierarchy between these components instead of accumulation, i.e., intensifying an initial component. Torsion texture evolution studies consisting of single phase materials (mostly fcc) has been conducted extensively in the past [67, 82, 84-90].

Most of the previous torsional behavior studies were focused on texture evolution using single phase materials. The major work in the understanding of torsion texture development of fcc materials was performed by Canova et al. [84]. Other major texture work involves the relation of the Swift Effect with texture evolution [67, 85, 89, 91, 92]. For instance, Montheillet et al. related the induced axial forces to the ideal texture components and their rotations with respect to the shear direction [67, 91]; Toth et al.

related the length changes in fcc materials to certain texture components, i.e., $\mathbf{A}_1^*$ and $\mathbf{A}_2^*$ [92]; and Baczynski and Jonas related the length changes again to a certain component, namely **D2**, using several bcc materials [89].

The ideal orientations of fcc and bcc materials observed under torsional deformation are summarized in Figures 2.35a and b in terms of (111) and (110) pole figures, respectively. The orientation relationships of these components are presented in Tables 2.1 and 2.2 for the fcc and bcc cases, respectively [82, 89], where the planes, {hkl}, are aligned with the shear plane normal (Z) and the directions, <uvw>, are aligned with the direction of the applied shear (θ).

SFE affects the critical material properties such as the slip behavior, twinning, and phase transformations which are all competing deformation mechanisms. Therefore, the texture evolution, could also be greatly dependent on the SFE of the material and this can change the appearance or disappearance of the ideal components such as the shifts observed from copper type to brass type textures with decreasing SFE values [87, 88]. The SFE-dependent texture evolution in nickel alloys was also shown by Hughes et al. [86]. Copper and brass type texture evolutions under torsional deformation are shown in Figures 2.36 and 2.37, respectively, as examples using ODFs.

For the case of copper vs. brass type textures: copper is a medium SFE material (80 mJ/m^2) [53] and its end texture evolution under torsional deformation is characterized by a dominant **C** component at room temperature, Figure 2.36 [67]. Brass on the other hand is classified as a low SFE material (~10 mJ/m^2) [53]. Given the lower SFE, the reported texture evolution is different from that of copper's as expected.

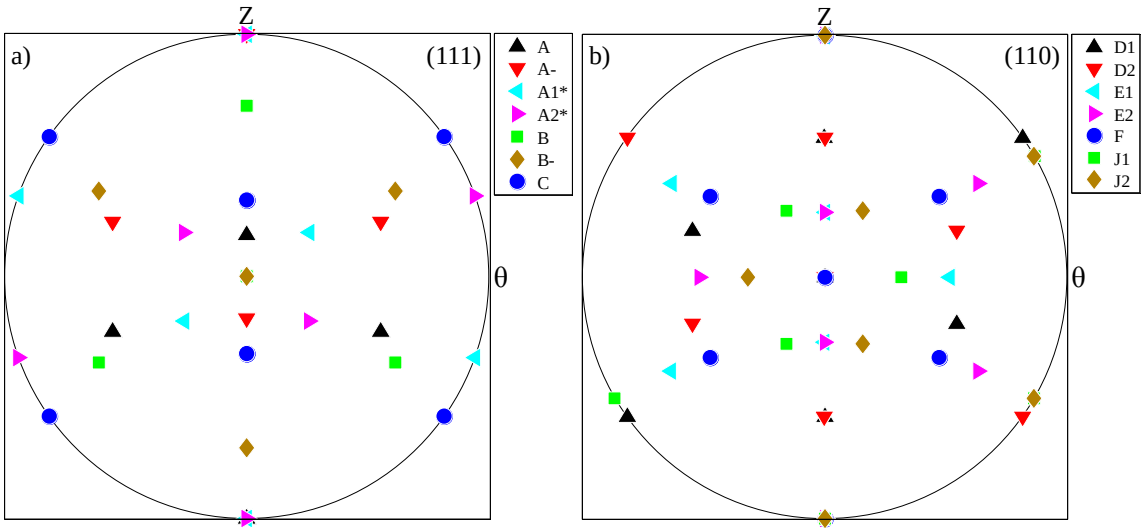

Figure 2.35. a) (111) pole figure showing the ideal fcc torsion texture components, b) (110) pole figure showing the ideal bcc torsion texture components. Z and θ denote the axial and shear directions of the specimen, respectively.

Table 2.1. Ideal components of fcc torsion textures with their orientations and Euler angles [82].

Component	**Orientation**	**Φ_1**	**Φ**	**Φ_2**
A	$(11\bar{1})[1\bar{1}0]$	0	35.26	45
$\overline{\text{A}}$	$(\bar{1}\bar{1}1)[\bar{1}10]$	180	35.26	45
A_1^*	$(11\bar{1})[2\bar{1}1]$	35.26	45	0
A_2^*	$(1\bar{1}1)[\bar{2}\bar{1}1]$	144.7	45	0
B	$(11\bar{2})[1\bar{1}0]$	0	54.74	45
$\overline{\text{B}}$	$(\bar{1}\bar{1}2)[\bar{1}10]$	180	54.74	45
C	$(100)[0\bar{1}1]$	90	45	0

Table 2.2. Ideal components of bcc torsion textures with their orientations and Euler angles [89].

Component	**Orientation**	**Φ_1**	**Φ**	**Φ_2**
D1	$(11\bar{2})[111]$	125.3	45	0
D2	$(\bar{1}\bar{1}2)[111]$	54.7	45	0
E1	$(01\bar{1})[111]$	39.2	65.9	26.6
E2	$(0\bar{1}1)[111]$	90	35.3	45
F	$(110)[001]$	180	45	0
J1	$(0\bar{1}1)[\bar{2}11]$	30	54.7	45
J2	$(1\bar{1}0)[\bar{1}\bar{1}2]$	90	54.7	45

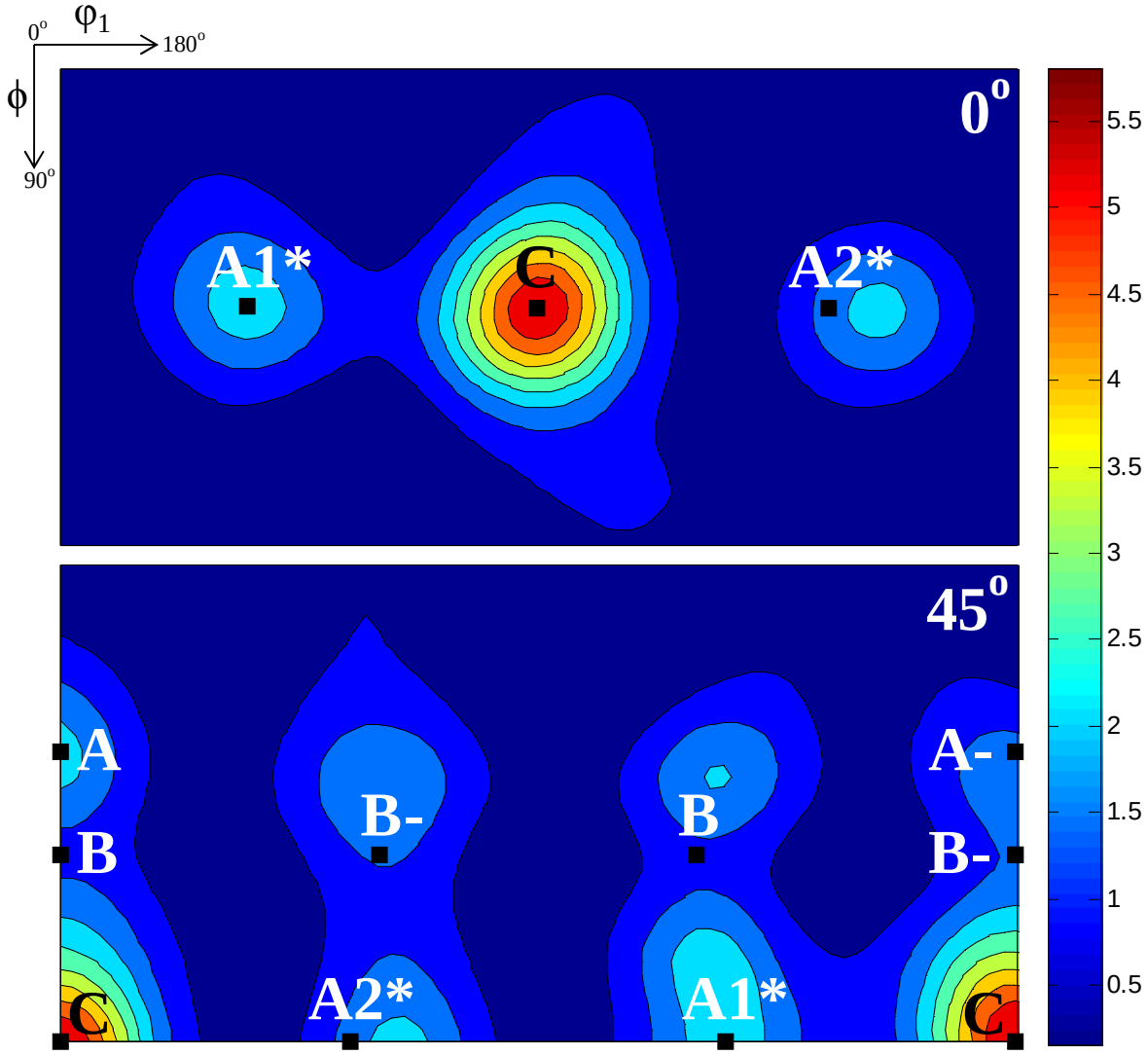

Figure 2.36. Orientation distribution function (ODF) sections (φ_2 = 0° and φ_2 = 45°) showing the characteristic texture evolution of pure copper deformed under torsion to a shear strain of 5.

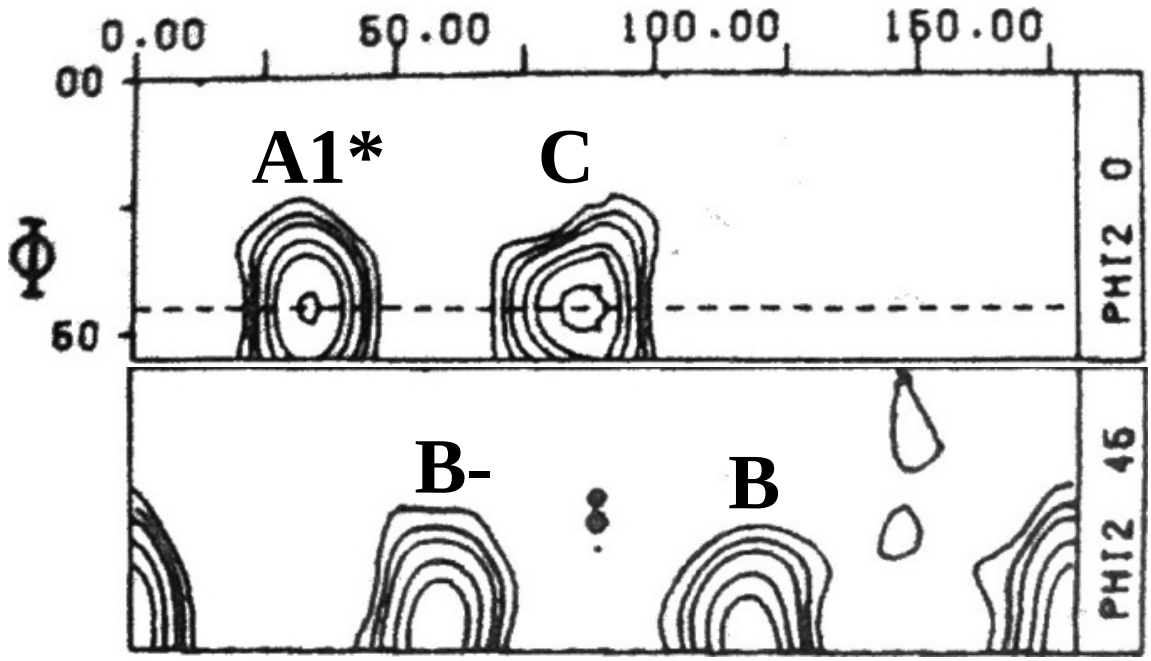

Figure 2.37. Orientation distribution function (ODF) sections ($\varphi_2 = 0^o$ and $\varphi_2 = 45^o$) showing the characteristic texture evolution of brass deformed under torsion to a shear strain of 8 [88].

In this alloy system, a more uniform distribution of ideal components are reported instead of a single dominant one [88], with usually the **B** component being the strongest, Figure 2.37 [87].

2.5.3. TRIP and Texture Evolution

Texture evolution is an important part of TRIP studies and it is suggested that due to the parent austenite being textured, the resultant martensite is also expected to be textured [13-15]. The crystallographic orientation relationship between the parent and the product is given in the general form: $\{h_1k_1l_1\}//\{h_2l_2k_2\}$, $\langle u_1v_1w_1\rangle//\langle u_2v_2w_2\rangle$. Four such relations have been employed in the case of transforming steels and these are known as the Bain [37], Kurdjumov-Sachs [93], Nishiyama-Wasserman [94, 95], and Greninger-Troiano [96] relationships. In terms of the texture relation between the parent and the product phases, the transformation in austenitic stainless steels is stated to follow the Kurdjumov-Sachs (KS) relationship which offers 24 variants, with an orientation relationship: $\{111\}\gamma//\{011\}\alpha'$, $\langle 110\rangle\gamma//\langle 111\rangle\alpha'$. However, it was also shown that not all the variants are favored in this mechanism that lead to the various variant selection studies [18, 34, 97-99].

Humbert et al. [18] conducted local texture analysis using EBSD which allowed them to probe the individual texture components separately. Using this approach the variant selection mechanisms taking place is demonstrated with an example texture evolution using the parent austenite grains belonging to the Cube component, $\{100\}\langle 100\rangle$, Figure 2.38.

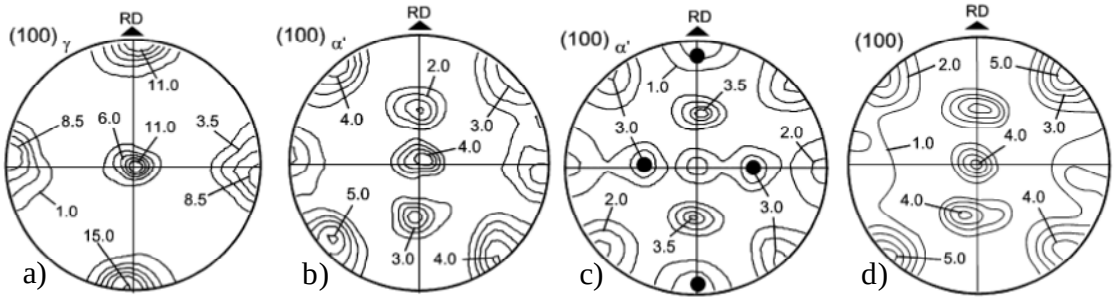

Figure 2.38. (100) pole figures of a 304 stainless steel deformed under uniaxial tension to 10% strain at -60^{o}C: a) measured austenite texture belonging to the Cube component; b) the measured α' martensite orientations formed in these austenite grains; c) α' martensite orientations predicted without variant selection; and d) α' martensite orientations predicted using variant selection [18].

The results show that without the variant selection the texture is over-predicted and the extra components are marked with the black circles, Figure 2.38c. Overall, this particular study is not complete and gives the main features of the experimental texture components as can be observed from the predicted texture shown in Figure 2.38. The selected variants in this model are the ones assisted by the most favorable stresses corresponding to the highest potential mechanical works at each step of the transformation, i.e., from γ to ε and from ε to α'.

Another work by Wittridge et al. uses the dislocation reaction model which is based on the presence of dislocations in the deformed austenite relying on the correspondence between the 24 possible Bishop-Hill slip systems and the 24 K-S transformation products [99]. The slip system based criterion selects the systems with positive/active shear i.e., systems that provide slip in the direction of the resolved shear stress. However, this slip activity criterion fails to select the additional variants necessary for an accurate prediction of the product texture. To overcome this issue the reaction variants were introduced into their model which allows for the acceptable reaction products of the two different Burger's vectors that were previously rejected by the positive slip criterion. Overall, by combining the two approaches they were able to obtain decent predictions [99].

A different approach is applied by a study of ButronGuillen et al. that combines a residual stress based growth condition, a slip activity based selection rule, and a growth rule based on the grain aspect ratio [98]. According to the residual stress criteria, the variants which reduce the residual stress in the matrix will be more preferred over the

others and the ones that increase it will be eliminated. Effect of slip activity criterion is based on the relative activities of the slip systems that define the variants which are grouped in four categories: 1) most active, 2) second most active, 3) low activity, and 4) no activity. The variants with the most active slip systems will be more preferred over the others based on this criteria. Finally, according to the grain aspect ratio parameter, when the grain shape is highly directional such as the case in pancaked grains, so is the transformation. Therefore, orientations associated with the growth direction such as RD in rolling, will be more favored over the others and by the same logic orientations related with the directions that are not favored such as ND will be retarded through the variant selection.

However, there are also other factors affecting the texture evolution of both the parent and the product phases especially in the case of deformation induced transformation. For instance, it is rather difficult to distinguish between the transformation and the deformation textures since the new martensite phase can also form a deformation texture [14]. Several studies also suggest that some parent grains could be more preferred for transformation over the others depending on their orientations [13, 21, 43]. The stored energy in each parent orientation also plays an important role in the transformation as it is suggested that the nucleation of the martensite embryos will be more frequent in the grains with the higher amount of stored energy [14]. These call for preferential transformation that can significantly affect the texture evolution especially in the parent phase.

For instance, Tao et al. has claimed that the (200) fcc grains in the loading direction were preferentially transforming to martensite under cryogenic compressive deformation at 203K [43]. To show the difference between the deformation texture related intensity changes and the changes resulting from the preferential phase transformation he has presented the relative intensity change in the (200) reflection under compression at room temperature where there was no transformation and the only intensity changes were due to texture rotations, Figure 2.39. However for compressive deformation at 203K where transformation was observed, the relative intensity changes were found to be even lower, i.e., more than expected from the texture rotations, Figure 2.39; signifying the possibility of preferential phase transformation.

Finally, even though preferential transformation and variant selection are not the same, both approaches suggest that the newly formed martensite should be textured either due to preferred transformation of certain austenite grains or because of the proposed variant selections taking place thereby making this a complex problem.

2.6. TRIP under Complex Loading

2.6.1. TRIP Behavior under Torsion

Phase transformation studies under torsional deformation are quite limited [17, 29, 100] when compared to the vast amount of knowledge under uniaxial tension or compression [41-43, 46-48, 64]. Amongst these studies, Miller and McDowell [100] discuss the macroscopic aspect of the transformation by comparing the stress-strain behavior of a 304L stainless steel under various deformation modes involving torsion,

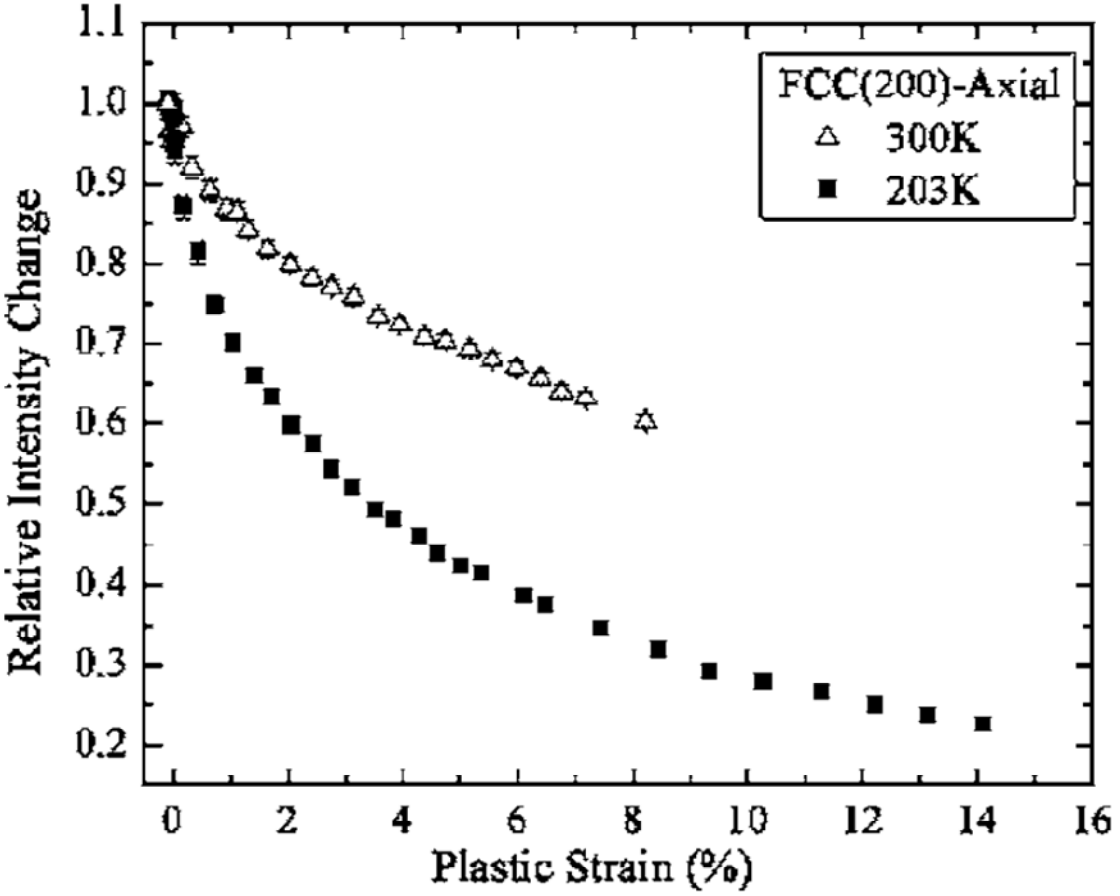

Figure 2.39. Relative intensity changes in the fcc (200) reflection as a function of applied plastic strain for samples deformed under compression at 300K and 203K [43].

compression, torsion followed by tension, and compression followed by torsion. The resultant phase transformations were also measured by using magnetization measurements even though the phase fractions obtained from this technique are not as accurate as the ones obtained using diffraction. This is mainly because diffraction offers a more sensitive means of probing the phase evolutions as will be explained in more detail in Chapter 4. Lebedev and Kosarchuk [29] conducted similar experiments using an Fe-Ni-Cr austenitic stainless steel; comparing bcc and hcp martensite phase evolutions under tension, compression, and torsion. However, the microscopic understanding of the relationships between the phase transformation kinetics and texture evolution was not investigated in these studies.

In the work by Wittridge and Jonas [17], an Fe-30% Ni alloy was used and was initially deformed at high temperature, above M_D, and then subjected to martensitic transformation by quenching the specimens in liquid nitrogen. So, the interaction between the deformation and transformation textures were separated. However, the main purpose of this study was to test a variant selection model and not the interaction between the different phase transformation kinetics and resultant texture evolutions regarding the relation between the deformation and transformation textures.

In essence, a basic research on the transformation kinetics and its relations with the resultant texture evolutions including the complexities that could arise between the interaction of deformation and transformation textures under torsional deformation is still lacking.

2.6.2. Multi-axial Deformation

Multi-axial deformation studies are even rarer than torsional studies even though these cases represent the most realistic real world working conditions of engineering materials. Multi-axial deformation can be applied in several forms such as, biaxial stretching [3], combination of axial strains and internal pressure [101], combination of torsional and axial strains [100, 102-104], etc. Even amongst these studies, the complexities involved in the micro-mechanical behavior lack proper explanation since most of the studies are conducted from a more macroscopic perspective.

Moreover, studies involving phase transformations under complex loads are even more scarce [3, 47, 100, 105]. Amongst these studies, Hecker et al. [3] has investigated the transformation behavior of a 304 stainless steel under balanced biaxial tension in comparison to tension again from a more macroscopic perspective, with basic martensite phase fraction evolutions obtained from magnetic measurements which revealed higher yield of martensite for biaxial tension. This was followed by a more thorough microscopic study by Murr et al. [105] where they have conducted extensive TEM work on these samples. Their results revealed that more shear band intersections, i.e., more nucleation points for martensite embryos, took place under biaxial tension compared to uniaxial tension, Figure 2.40, that caused the elevated martensitic transformation. Jacques et al. [47], on the other hand, have demonstrated the effect of deformation mode on martensitic phase transformations by performing simple shear, Marciniak, uniaxial tension and equibiaxial tension tests on TRIP-assisted steels. Using a combination of image analysis, dilatometry, x-ray diffraction and Mössbauer spectroscopy they have

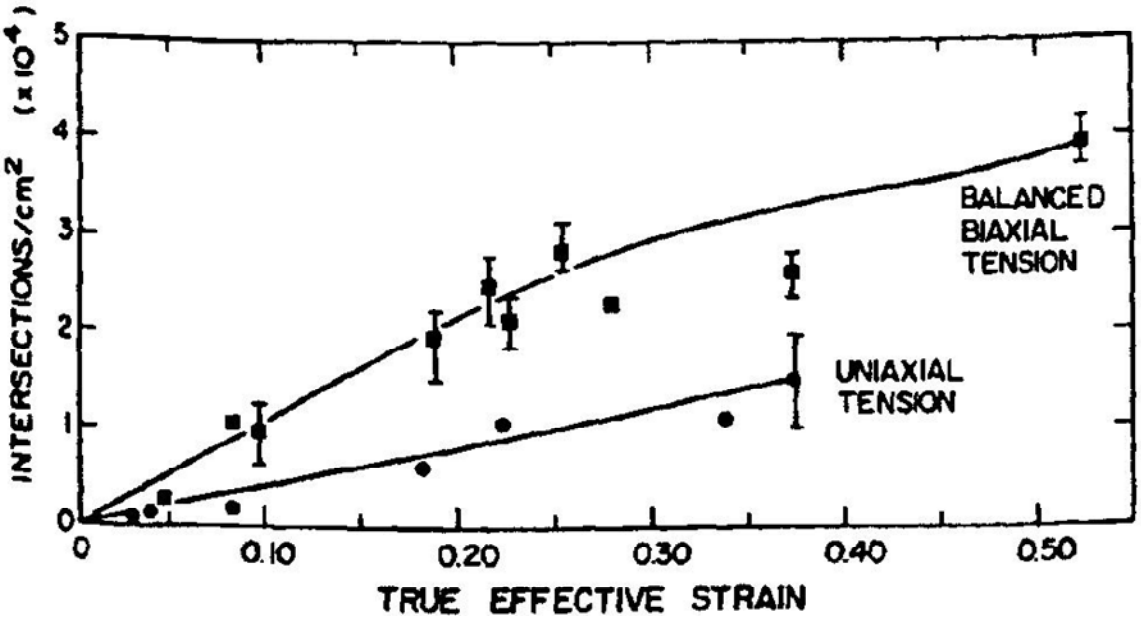

Figure 2.40. Number of shear band intersections measured from TEM micrographs as a function of applied true strains for samples deformed under balanced biaxial tension and uniaxial tension [105].

shown the strain-path dependent phase transformations with the highest transformation observed under the Marciniak test followed by equibiaxial stretching, tension and simple shear.

Multi-axial deformation modes are not standard test methods unlike the more common uniaxial ones, therefore even obtaining a proper testing equipment is not an easy task. Moreover, due to the inherent complexities the results are harder to analyze. Even these seemingly basic reasons could help explain why these deformation modes have been mostly overlooked.

Chapter 3 Radial Distribution of Martensitic Phase Transformation in a TRIP Steel under Torsional Deformation

This chapter is written based on a paper published by Ercan Cakmak et al.:

Ercan Cakmak, Hahn Choo, Ke An, and Yang Ren, "Radial Distribution of Martensitic Phase Transformation in a Metastable Stainless Steel under Torsional Deformation: A Synchrotron X-ray Diffraction Study", Materials Letters, 65 (2011) 3013-3015.

As the first author, my primary contributions include (1) proposing the study and identifying its importance, (2) design and conducting most of the experiments, (3) data analysis and interpretation, and (4) writing the paper.

Abstract: The strain-induced martensitic phase transformation in a metastable 304L stainless steel under torsional deformation was investigated using synchrotron x-ray diffraction. The measured radial distribution of the martensite phase fraction in a solid cylindrical specimen agrees well with the prediction based on a combination of transformation kinetics and a radial plastic strain distribution equation.

3.1. Introduction

During a pure torsion test, large strains can be applied to the material due to the mechanical and geometrical stability of the test. However, the torsion test has also its drawback in that the shear strains show significant radial gradient in a solid-cylindrical specimen, i.e., highest on the surface and zero at the center [53].

The radial strain gradient is prone to cause significant inhomogeneities that can affect the materials' performance under load. However, amongst torsional deformation studies, the radial-position dependency issue has been mostly overlooked except for few [106]. In the simplest case, the effects could be in the form of variations in the strain hardening behavior if the material consists of a single phase as in [106]. Such effect can become more complicated in the case of TRIP steels, where the strain gradient through the radius results in a variation in phase transformations. In this study, a series of torsion tests was conducted on a metastable 304L stainless steel that exhibits the TRIP effect when strained at ambient temperature; covering a wide range of shear strains using solid-cylindrical specimen geometry. Then, the radial gradients in the phase transformations within the torsion specimens were investigated using high-energy synchrotron x-ray diffraction (s-xrd) [45]. Finally, the measured gradient in the martensite phase fractions are compared to a calculation based on a combination of transformation kinetics established using an Olson-Cohen model [20] and a linear radial plastic-strain variation equation [53].

3.2. Experimental Details

A cylindrical bar of commercial-grade 304L stainless steel was prepared by extrusion followed by an austenitizing heat treatment resulting in a weak initial extrusion texture of a mixture of (111)/(100) fibers and an average grain size of 50 microns. The nominal composition (in weight %) of the material used in this study is 0.022 C, 0.03 Co, 18.18 Cr, 0.14 Cu, 1.54 Mn, 0.11 Mo, 0.076 N, 8.55 Ni, 0.026 P, 0.0117 S, 0.29 Si and balance Fe.

The torsion testing specimens were machined with a length of 5 mm (parallel to the extrusion direction) and a diameter of 10 mm in the gage section. The reason for a relatively short gage length used in this study was to maximize the achievable shear strains as the amount of shear strain per degree of rotation is inversely related to the gage length according to Eq (2-11) [53]. Eq. (2-11) also assumes that the shear strain is proportional to the radial position, r. The torque data is converted to shear stress, according to Eq. (2-16).

$$\gamma = \tan\phi = \frac{r\theta}{L} \tag{2-11}$$

$$\tau_a = \frac{\left(\theta' \frac{dM_T}{d\theta'} + 3M_T\right)}{2\pi a^3} \tag{2-16}$$

The torsion specimens were deformed at an equivalent strain rate ($\dot{\varepsilon}$) of $5\text{x}10^{-3}$ s^{-1} at room temperature, under fixed-end torsion condition to different strain levels as summarized in Table 3.1, using the servo-hydraulic MTS multi-axial load frame of the VULCAN instrument at Oak Ridge National Laboratory.

Table 3.1. List of the torsion specimens deformed to different levels of shear strain, and the resulting phase fractions measured near the surface.

Sample Code	**Shear Strain**	**fcc wt.%**	**bcc wt.%**	**hcp wt.%**
T0	0	100	0	0
T1	0.17	93.1	0.8	6.1
T2	0.35	90.9	3.9	5.2
T3	0.52	84.4	8.0	7.6
T4	0.70	78.2	12.6	9.2
T5	1.04	64.4	25.9	9.7
T6	1.40	51.7	39.7	8.6
T7	1.74	41.0	48.3	10.7
T8	2.09	37.8	56.0	6.2
T9	2.55	31.6	63.5	4.9

After a series of torsional deformations to varying degrees of total shear strains ranging from 0.17 to 2.55 (Table 3.1), pins of 3 mm diameter were extracted from the central portions of each deformed specimen along the radial direction for subsequent synchrotron x-ray diffraction (s-xrd) measurements. Electric discharge machining (EDM) was used for the extraction in order not to heat the pin samples that can cause reverse transformation during the machining. A schematic showing the pin extraction and the radial s-xrd scans along the specimen diameter (i.e., pin length) is given in Figure 3.1.

The diffraction experiments were conducted using high-energy synchrotron radiation at the Advanced Photon Source (APS), Beamline 11-ID-C, Argonne National Laboratory. The wavelength employed was 0.107841 angstroms with a sample to detector distance of 1120 mm which covered eleven reflections each for the fcc (111 to 440) and the bcc (110 to 420) phases. The beam size was 300 μm by 300 μm, which allowed us to illuminate approximately 2000 grains through the pin diameter; and a Perkin-Elmer area detector was used to obtain the Debye-Scherrer rings using the transmission geometry. The radial position scans were performed on the pins starting from the outer surface (P5, Figure 3.1b) through the center (P0, Figure 3.1b) with a step size of 1 mm. An as-received sample was also measured to obtain the initial phase fractions. Data collection was performed in the form of a complete texture measurement since the strain-induced martensitic phase transformations can be strongly orientation dependent [13, 107]. The diffraction data was analyzed using Material Analysis Using Diffraction (MAUD) [108] software to derive phase weight fractions.

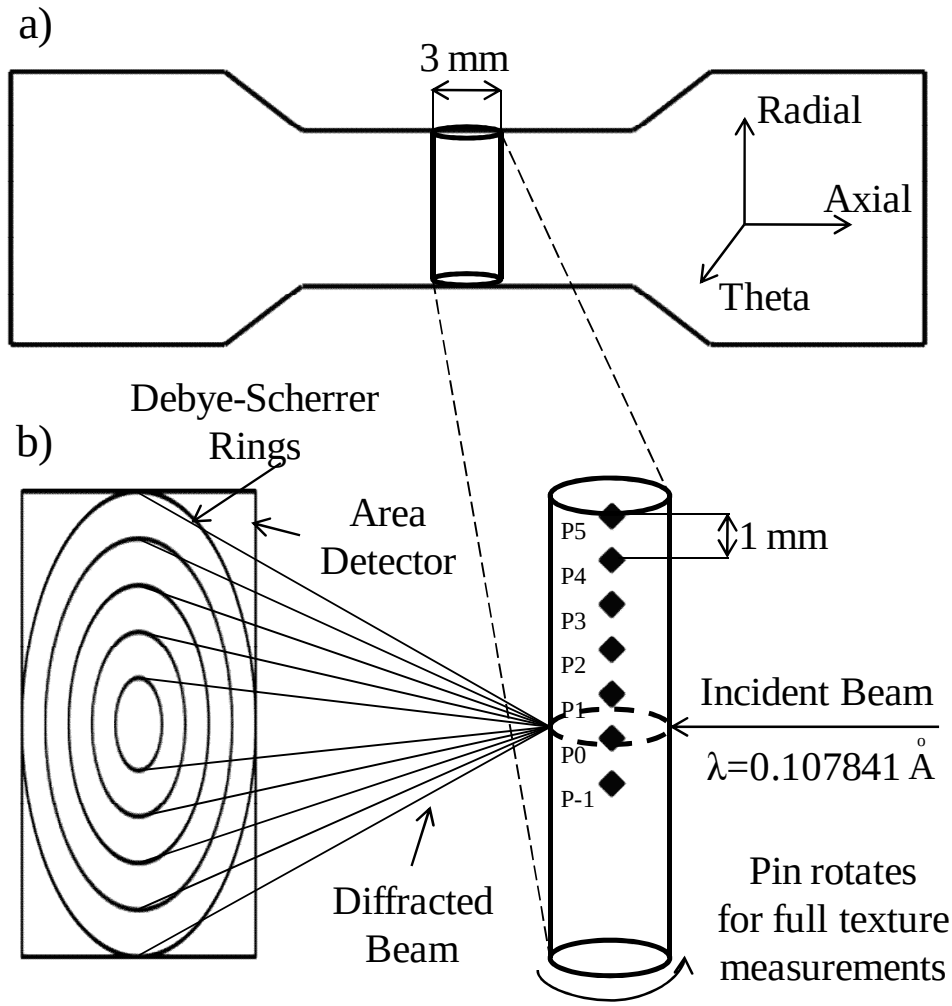

Figure 3.1. a) A schematic of the torsion specimen showing the location of the pin, extracted for s-xrd measurements. Also shown is the orientation relation of the pin with respect to the torsion specimen. b) A schematic of the diffraction measurement setup in transmission geometry.

3.3. Results and Discussion

The shear stress-shear strain curve is presented in Figure 3.2. The material shows significant hardening, reaching a maximum shear stress value of 730 MPa; combined with a high shear ductility of 2.55 at failure due to the enhanced ductility through the TRIP effect and the stability of the torsion test. The evolutions of the fcc, bcc, and hcp phase fractions measured near the surface of all nine specimens are presented in Figure 3.3 and Table 3.1 as a function of applied shear strains. The fcc phase fraction continuously decreases with increasing shear strain due to the strain-induced martensitic phase transformation [45]. The bcc transformation starts as low as γ = 0.17. The transformation becomes more rapid with increasing strains up to a point around γ = 1.25, and, then the transformation slows down gradually; reaching a total of 63.5 wt.% bcc fraction for the specimen T9. For the hcp martensite, the phase fraction also increases at the early stages of deformation; even surpassing the bcc phase fraction. However, this transformation then follows a plateau; finally starting to decrease towards the end of the deformation consistent with the results from the tensile deformation of the same material [19, 41, 109].

The Olson-Cohen model [20] was used to fit the bcc martensite evolution. The original model is based on a curve fitting procedure described with the formula below:

$$f^{\alpha'} = 1 - \exp\left\{-\beta\left[1 - \exp(-\alpha\varepsilon)\right]^n\right\} \tag{3-1}$$

where, $f^{\alpha'}$ is the bcc martensite fraction, α is a parameter representing the rate of shear band formation with respect to strain, β is related to the probability that a shear-band

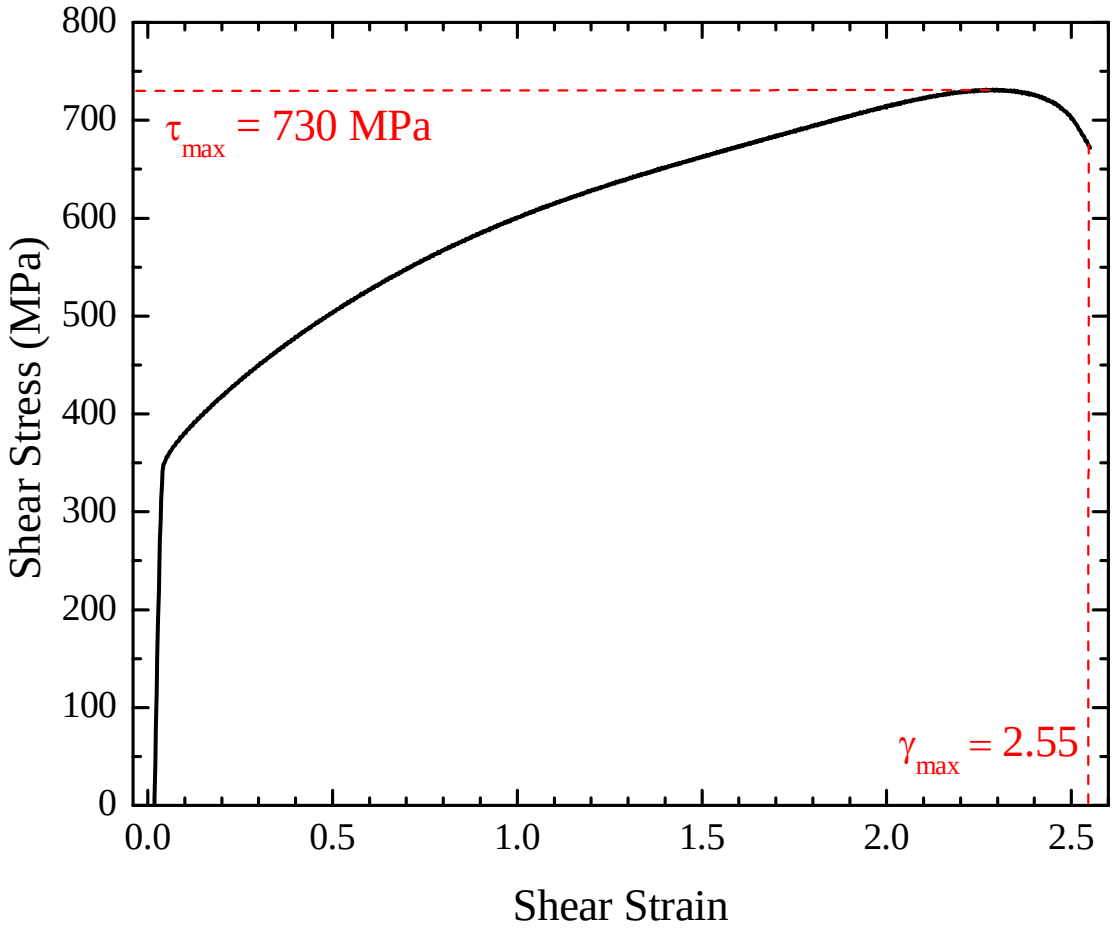

Figure 3.2. Shear stress - shear strain curve of the 304L stainless steel tested until failure at room temperature. The sample failed at a shear strain of 2.55 resulting in a maximum shear stress of 730 MPa.

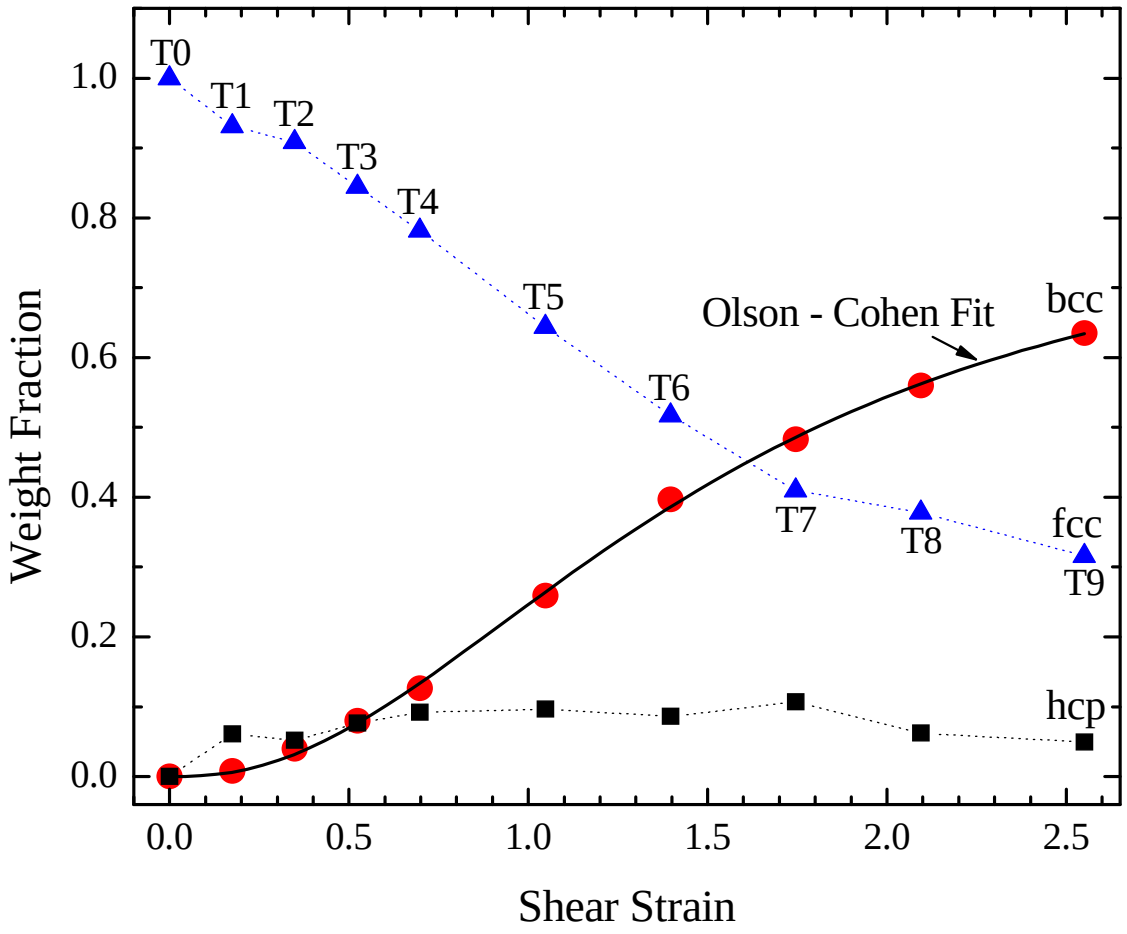

Figure 3.3. Evolution of phase fractions, measured at position P5, as a function of applied shear strains for austenite (fcc) and martensite (bcc and hcp) phases from the as-received condition, T0, to sample failure at $\gamma = 2.55$, T9. The bcc martensite phase evolution was fitted using the Olson-Cohen model, shown as a solid curve over the measured data points.

intersection will generate a martensitic embryo, ε is the true stain, and n is an exponential constant.

The shear strain (γ) was used in Eq. (3-1) instead of the true strain (ε) and the bcc transformation curve in Figure 3.3 is best fitted with constants of $\alpha = 0.73$, $\beta = 1.55$, and $n = 2.59$ (with R^2 of 0.999). These parameters are found to be the same except for α which would increase to 1.27 if equivalent strain values were used. The fit result is shown in Figure 3.3 as the solid line through the data points.

The fit parameters are different compared to the tension case reported in [20] due to many reasons. For one example, the different loading path leads to a different slip mode as well as the number of active slip systems that influence the transformation kinetics. But, it should be noted that the discussions of the transformation kinetics in comparison to the tensile deformation is beyond the scope of the current chapter. Instead, the fit parameters established here will be used to understand the radial distribution of the phase transformation during the torsional deformation of the solid cylinder.

The radial distributions of bcc martensite phase fractions measured from the radial scans (from P5 to P-1, Figure 3.1b) of each deformed specimen are presented as symbols in Figure 3.4. Note that the bcc martensite amount decreases systematically moving inwards from the surface (P5); reaching near zero values at the center (P0) for all specimens. This is in agreement with the theory that no strain is present at $r = 0$ (Eq. (2-11)) and therefore, no strain-induced transformation. Moving to the bottom of the sample (P-1) it can be seen that the bcc martensite starts to increase again with increasing radial strain, showing the expected symmetry.

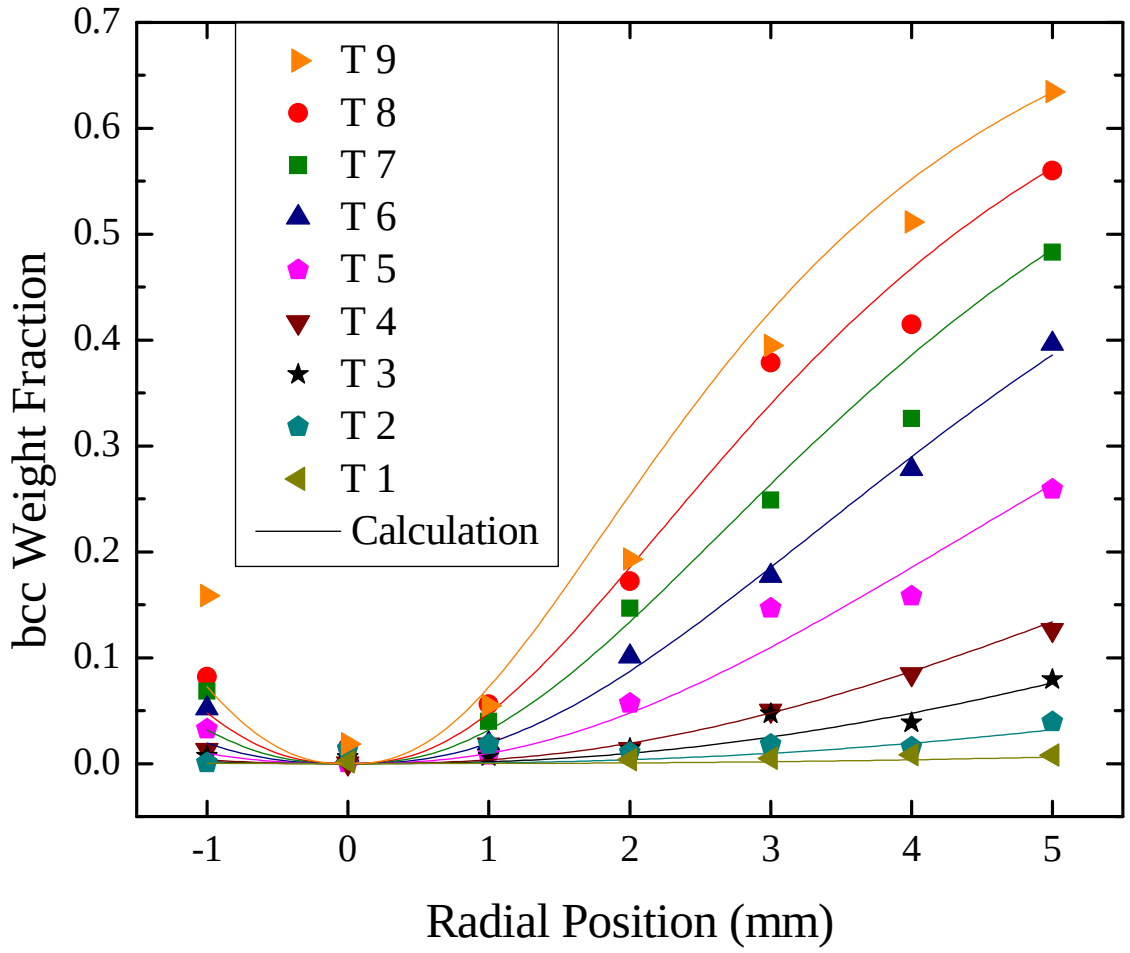

Figure 3.4. The bcc phase distributions plotted as a function of radial position. The lines represent the calculated phase fraction distributions obtained using the Olson-Cohen model with the fit parameters established earlier using the surface data (Figure 3.3).

Also shown in solid lines in Figure 3.4 are the calculated radial distributions of the bcc phase fractions for each specimen. For this calculation, first the radial positions (r = 0 to 5) are converted to shear strains using Eq. (2-11). Then, the calculated shear strains were used in the Olson-Cohen model, Eq. (3-1) with the parameters of α, β, and n, already established in Figure 3.3, to calculate the radial distribution of the bcc martensite phase fractions. The calculated line agrees quite well with the s-xrd data for all cases.

Overall, it was found that there is a good agreement between the bcc martensite phase fractions measured from the radial scans for all specimens, and the calculations based on the Olson-Cohen model using the shear strains calculated from the radial positions according to Eq. (2-11) as the input. Therefore, the results suggest that the approximation of linear strain variation through the radius is valid even at large strains (inhomogeneous plastic deformation for solid cylindrical samples) and that the radial strain distribution can be readily defined with an acceptable accuracy using the simple shear strain relation, Eq. (2-11). Also, the accompanying phase transformations can be estimated as a function of γ (shear deformation) or r (radial positions) for a given alloy system using the Olson-Cohen parameters established for a given condition.

3.4. Conclusions

A series of torsion tests were carried out on a metastable 304L stainless steel to study the strain-induced phase transformations as a function of the radial position in a solid-cylinder specimen using synchrotron x-ray diffraction (s-xrd). Using the transformation kinetics established following Olson-Cohen, the radial distribution of

martensite fractions was calculated assuming the linear radial plastic strain distribution. The assessed radial phase distribution matches well with the s-xrd measurements implying that, in a solid-cylindrical specimen under torsion, the approximation of linear variation of plastic strain across the radius is reasonable and the volumetric distribution of strain-induced martensite phase fractions can be calculated once the Olson-Cohen parameters are established for the given alloy system.

Chapter 4 Phase Transformation Kinetics and Texture Evolution in a TRIP Steel Under Torsional Loading

This chapter is written based on a paper published by Ercan Cakmak et al.:

Ercan Cakmak, Hahn Choo, Ke An, and Yang Ren, "A Synchrotron X-ray Diffraction Study on the Phase Transformation Kinetics and Texture Evolution in a TRIP Steel Subjected to Torsional Loading", Acta Materialia, 60 (2012) 6703-6713.

As the first author, my primary contributions include (1) proposing the study and identifying its importance, (2) design and conducting most of the experiments, (3) data analysis and interpretation, and (4) writing the paper.

Abstract: The martensitic phase transformation kinetics and its relations with texture evolutions in the constituent phases were studied for a transformation induced plasticity (TRIP) steel under a torsional loading condition at ambient temperature. Synchrotron x-ray and electron back-scatter diffraction techniques were used to investigate the phase transformation-microstructure-texture evolution relations. The effects of the deformation texture development in the parent austenite phase on the observed phase transformation kinetics are discussed in terms of preferred transformation mechanisms. The texture evolution in the product martensite phase is also discussed in terms of a possible texture inheritance from the parent austenite phase and its own deformation texture.

4.1. Introduction

As it was stated in Chapter 2, phase transformation studies under torsional deformation are quite limited [17, 29, 100]. As a result, the basic microscopic understanding of the relationships between the phase transformation kinetics and texture evolution during torsional deformation lacks. In this chapter, we will present the phase transformation behavior and the texture evolution of the constituent phases, measured using synchrotron x-ray and electron back-scatter diffraction techniques, during torsional deformation of a metastable austenitic stainless steel that exhibits the TRIP effect at ambient temperature. Furthermore, the phase transformation kinetics-microstructure-texture evolution relations will be discussed in the context of texture-dependent preferential phase transformation and possibility of texture inheritance in the product martensite phase from the parent austenite.

4.2. Material and Torsion Testing

The properties of the 304L stainless steel used for this chapter were already presented in Chapter 3 along with the details of the torsion test conditions.

4.3. Texture and Phase Fraction Measurements Using Synchrotron X-ray Diffraction

The sample extraction process for the phase and texture evolution measurements and the S-XRD setup is the same as described in Chapter 3 with the exception that here the measurements were performed at the tip of the pins, Figure 4.1.

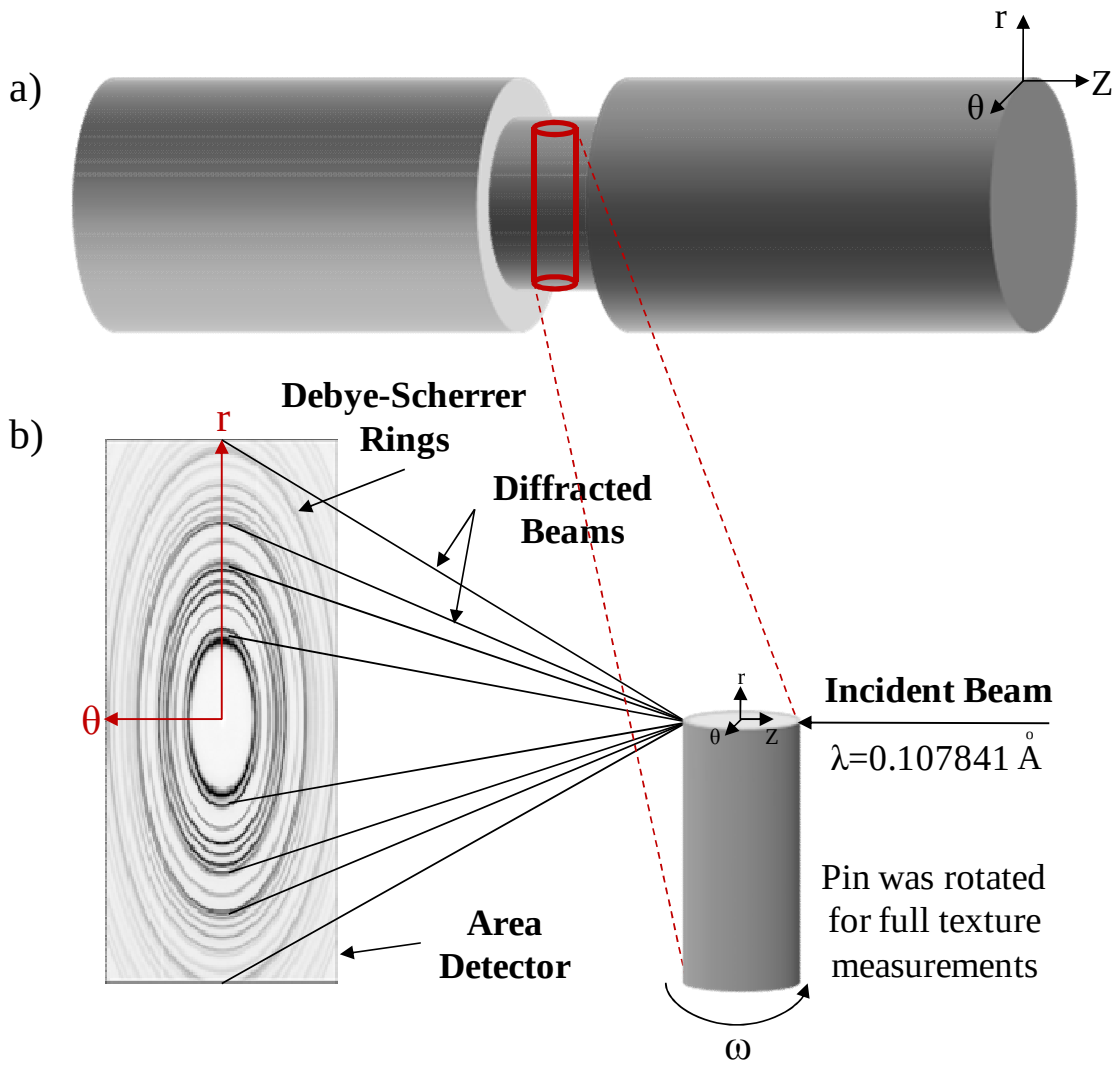

Figure 4.1. a) A schematic of the mechanical testing specimen showing the location of the pin extracted for S-XRD and EBSD measurements. Also shown is the orientation relation of the pin with respect to the bulk specimen. b) A schematic of the S-XRD measurement setup in transmission scattering geometry. r, θ, and Z refer to the radial, shear, and axial directions of the bulk specimen, respectively. ω corresponds to the rotation axis for the S-XRD measurements.

In addition, the texture data was collected by mounting the pin samples on a rotary stage and by rotating ω from 0 to 180 degrees with a 30-degree step size; obtaining full pole coverage. For the evaluation of phase and texture evolutions, the Debye-Scherrer rings obtained from the S-XRD scans were converted into diffraction patterns using the Fit2D software with 10-degree 'caking'. The diffraction data was then analyzed for phase fractions and texture by performing Rietveld Refinement using the Material Analysis Using Diffraction (MAUD) software [108] and using the E-WIMV algorithm for the texture analysis. The raw pole figure data were processed further using the MTEX quantitative texture analysis software [110] for texture rotations, plotting PFs, and calculating ODFs.

S-XRD [16, 45, 48] plays an important role in this study for three main reasons. First, the high energy, i.e., low wavelength, enables complete pole coverage and collection of many {hkl} reflections from multiple phases. Second, the high angular resolution enables a clear separation of the overlapping peaks from multiple phases (fcc, bcc, and hcp) and also enables detection of the weaker peaks at the early stages of transformation; resulting in detailed observations of the changes in weight fractions of each phase. Finally, the high energy and parallel beam allow us to define a very fine beam window for a high spatial resolution, which enables us to probe the phase evolutions without a significant volume averaging over the sharp gradient in strain and phase fraction across the radius in the torsionally deformed solid cylinder specimens [111].

4.4. Microstructural Characterization Using Electron Back-scatter Diffraction

Following S-XRD measurements, select samples from torsion (T3-T6) were characterized using electron back-scatter diffraction (EBSD) to investigate the microstructure-phase transformation-texture evolution relations. The same pin specimens used for the S-XRD measurements, Figure 4.1, were used for the EBSD measurements. The pins were mounted in conductive resin exposing the Z-θ plane to the electron beam, Figure 4.1.

The EBSD measurements were performed on an AZTEC system with a NordlysNano detector provided by OXFORD Instruments. The applied beam energy (acceleration voltage) was 20kV with a probe current of 2nA, and the scan step size was 0.5 μm. Five different areas were scanned for each specimen to improve the statistics. The measured band contrast images were post-processed to obtain the phase, grain orientation, and texture component maps. As the name suggests, the phase maps show the distribution of the phases in the microstructure. The orientation map, on the other hand, shows the alignment of the (hkl) plane normals of the grains with a given specimen direction such as Z, Figure 4.1. Finally, the texture component map reveals which ideal texture component the grains belong to.

4.5. Results

4.5.1. Phase Transformation Kinetics

Figure 4.2 shows example diffraction rings (at $\omega = 0^{o}$) and the corresponding diffraction patterns at three different shear strains; T1, T5, and T9. Figure 4.2 qualitatively illustrates the phase evolution with increasing shear strains during the torsional deformation. At the beginning of the plastic deformation, T1, the material is almost fully austenitic with a small amount of hcp phase, Figure 4.2a. The bcc martensite in this case is not yet resolved. At the intermediate strain, T5, the bcc martensite grows in intensity and becomes much better resolved, Figure 4.2b. Finally, at T9 the bcc phase is the dominant one when the peak intensity levels are compared to the other phases, Figure 4.2c.

The results of the phase evolutions during the torsional deformation were already summarized in Figure 3.2 and Table 3.1, Chapter 3; with a bcc phase fraction increasing up to 63.5 wt.% at T9.

4.5.2. Texture Evolution

4.5.2.1. Austenite Texture Evolution

For the analysis of the texture evolution in the fcc parent austenite phase, the ideal texture components of a single-phase fcc observed under torsional deformation were shown in Figure 2.35a in terms of a (111) pole figure. The orientation relationships of these components were also presented in Table 2.1 [82], where the planes, {hkl}, are

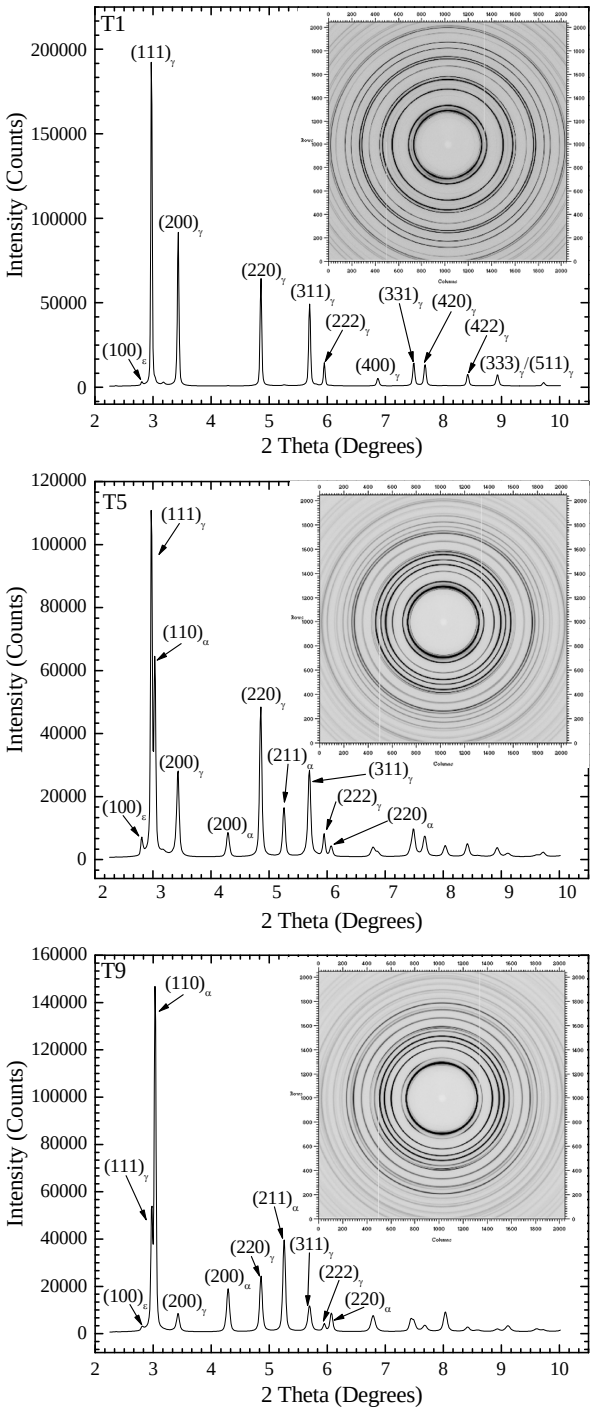

Figure 4.2. Selected diffraction patterns (rθ plane, at ω=0^o) obtained from the 360^o integration of the Debye-Scherrer rings for three different applied shear strains after the torsional deformation: a) T1 (γ = 0.17), b) T5 (γ = 1.04), and c) T9 (γ = 2.55).

aligned with the shear plane normal (Z), and the directions, <uvw>, are aligned with the direction of the applied shear (θ) as shown in Figures 4.1 and 2.35.

The measured fcc austenite (111) pole figures are shown in Figure 4.3 as a function of the applied shear strain. There are two stages of texture evolution: first, from T0 to T4 and second, from T5 to T9 in terms of qualitative texture intensity changes. In the 'initial stage', a breakdown of the pre-existing weak extrusion texture is observed from T0 to T2, which is followed by the settling of the torsional deformation texture from T3 to T4. At T4, a distinct torsional deformation texture for an fcc material is established. Subsequently, the 'second stage' of texture evolution results in the weakening of several components as evident from the pole figures of T5 to T9. However, each of the texture components cannot be clearly identified since several components overlap in pole figure representations of the texture. In order to analyze the texture evolution and identify the vanishing (and strengthening) components, ODFs are obtained as a function of the shear strain (T0-T9), Figure 4.4.

The ODFs reveal a more detailed texture evolution as the overlap of ideal components that occurs in PFs is avoided. First, the breakdown of the initial texture is observed from T0 to T2 followed by an initial strengthening of the **C** component with increasing shear strains from T2 to T4. After reaching its maximum intensity at T4, the **C** component shows a continuous decrease in intensity, approaching almost the random level at T9. Another component that shows a decreasing trend is the $\mathbf{A}_2^*$ component which reaches the random level at T9.

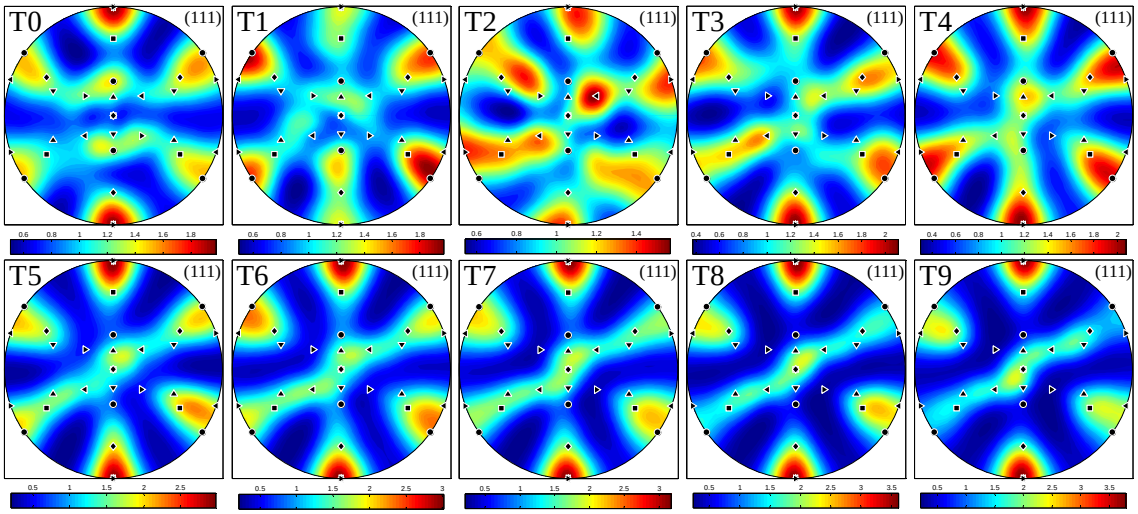

Figure 4.3. (111) pole figures (PF) showing the fcc austenite texture evolution as a function of the applied shear strain (T0 to T9). Note that each PF has its own scale bar and provides a qualitative observation of the texture evolution. In all PFs the north pole denotes the axial direction (Z) and east, the shear direction (θ).

Figure 4.4. Orientation distribution function (ODF) sections ($\varphi_2 = 0^o$ and $\varphi_2 = 45^o$) showing the qualitative texture evolution of the fcc austenite as a function of shear strain from T0 to T9.

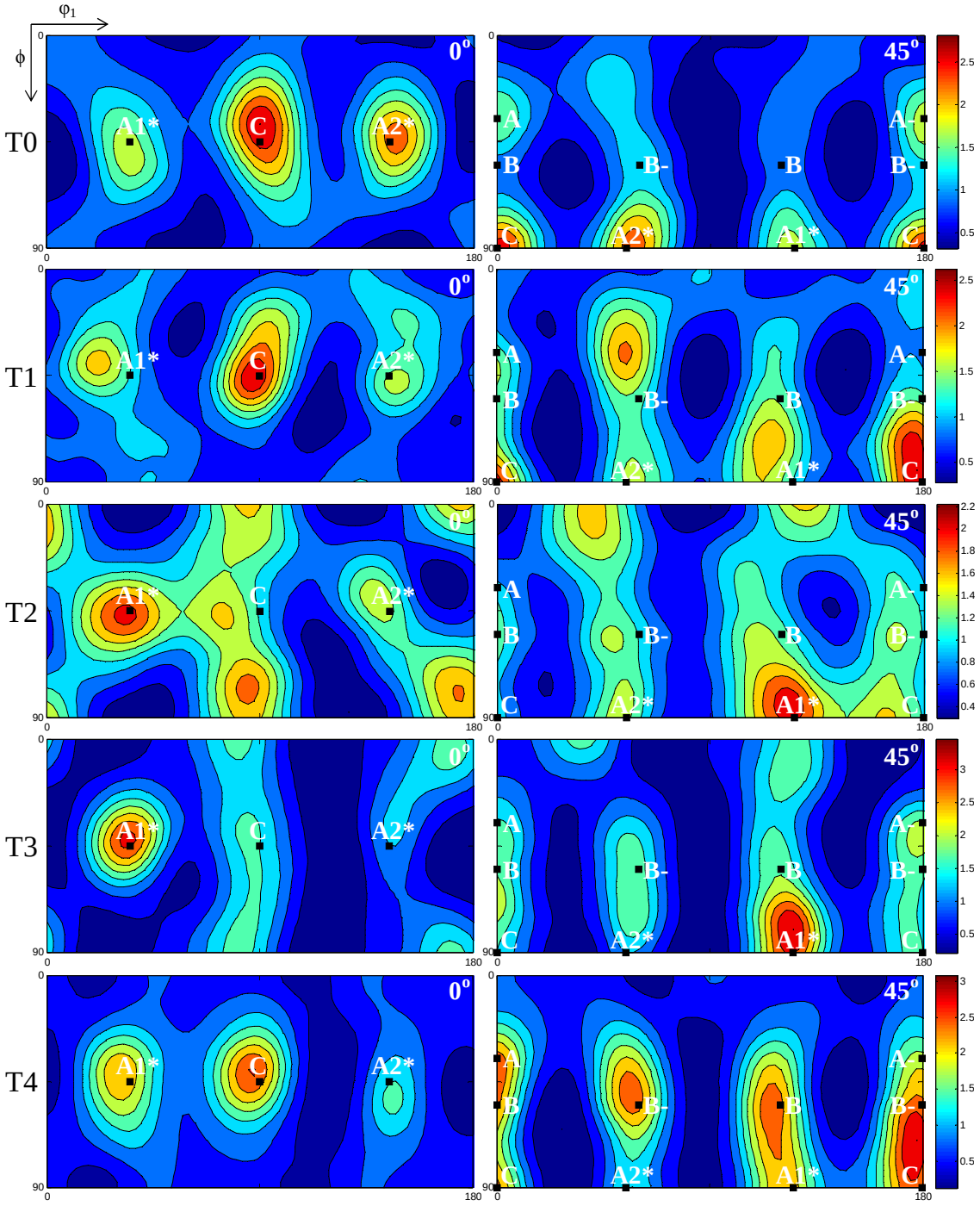

Figure 4.4. Continued.

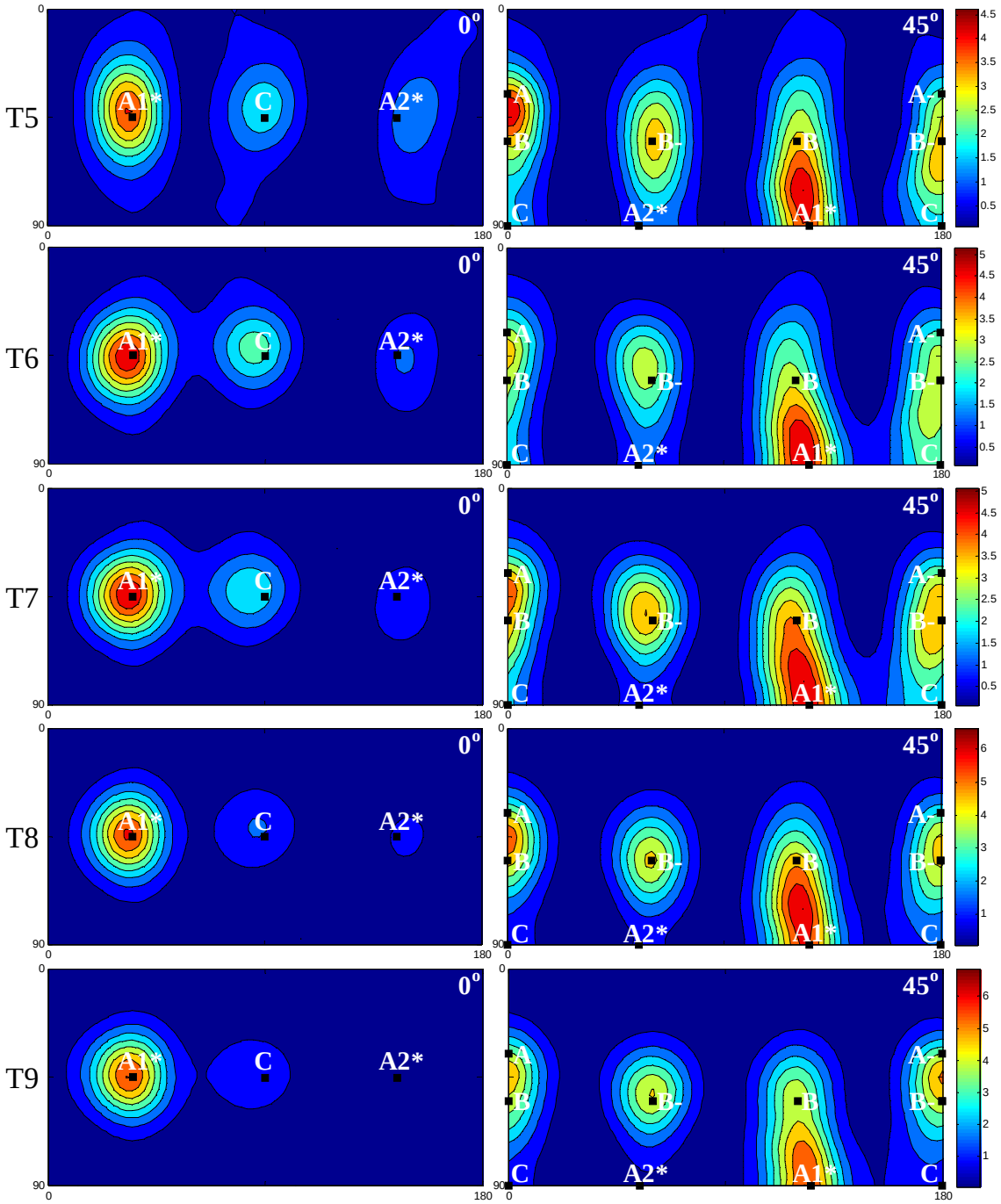

Figure 4.4. Continued.

The main difference between the $\mathbf{A}_2^*$ and **C** components is that, unlike **C**, the $\mathbf{A}_2^*$ never shows an increasing trend throughout the entire deformation history. This particular behavior of the **C** component suggests a possible selective transformation mechanism and will be discussed further in Section 4.6.2.

The quantitative evolutions of the ideal components derived from the ODFs are summarized in Figure 4.5 in terms of the texture component intensity as a function of the applied shear strain. After the breakdown of the initial texture from T0 to T2 ($\gamma = 0.35$), all components, except **C** and $\mathbf{A}_2^*$ show a continuous increase in intensity with increasing shear deformation. At T9 ($\gamma = 2.55$), the intensity hierarchy of the components are $\mathbf{A}_1^* > \mathbf{B} \geq \mathbf{A} >> \mathbf{C} > \mathbf{A}_2^*$.

Finally, the Visco-Plastic Self-Consistent (VPSC) model [112] was used to calculate and illustrate the distribution of the Taylor factors in the fcc phase during the torsional deformation. The modeling was carried out with 14,400 grains under the fixed-end torsion using secant linearization with fcc slip on the {111}<110> system. Since the Taylor factors are grain-orientation dependent, the model calculates the Taylor factors of each grain based on the predicted texture. For this procedure, the experimental texture from T4 was used as an input. In order not to cause additional texture evolution, minimal straining on the order of γ=0.01 was applied. The calculated Taylor factor data for 14,400 grains is then used as input to the MTEX software and the Taylor factor map is plotted covering all of the ideal fcc texture components, Figure 4.6.

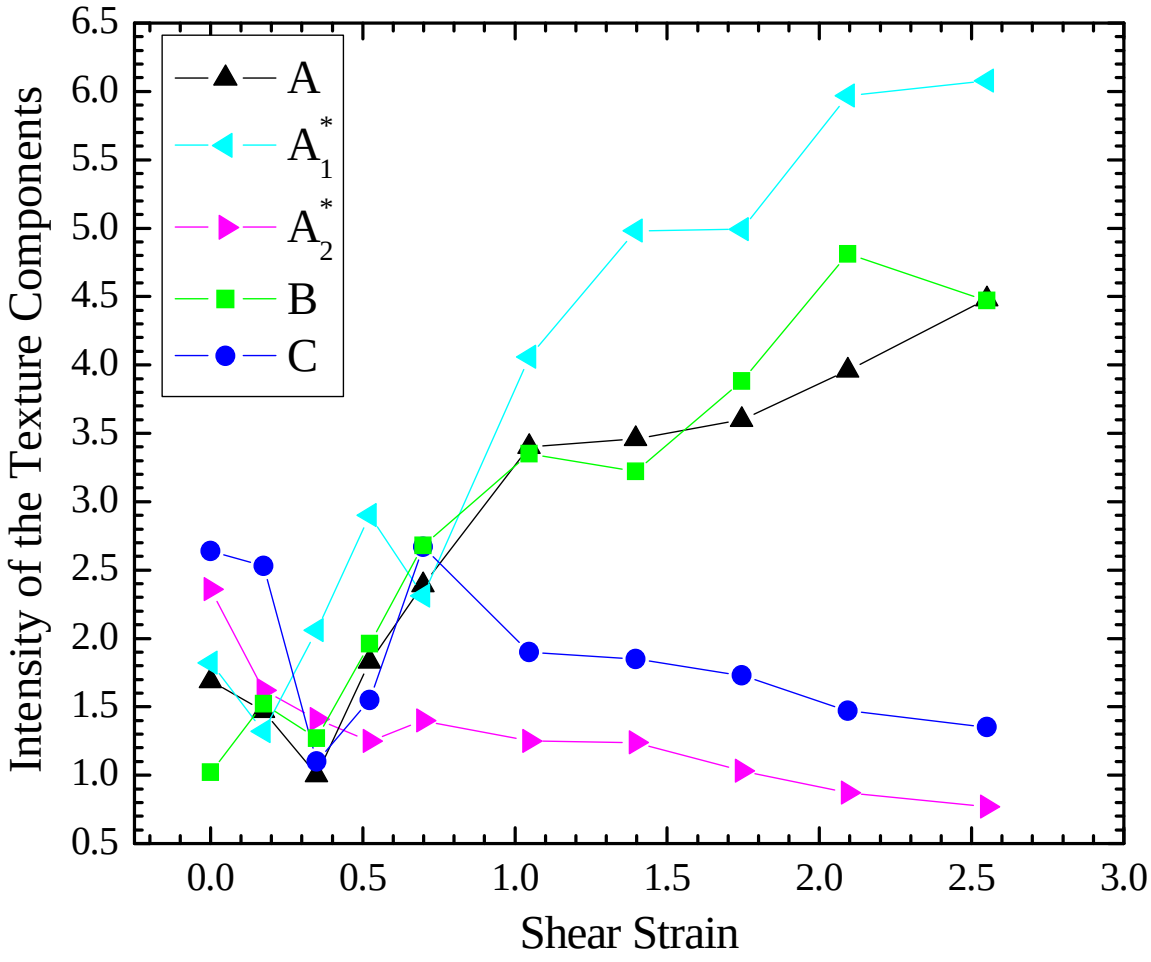

Figure 4.5. The intensity evolutions of the ideal fcc torsion texture components in the austenite phase measured as a function of the applied shear strain.

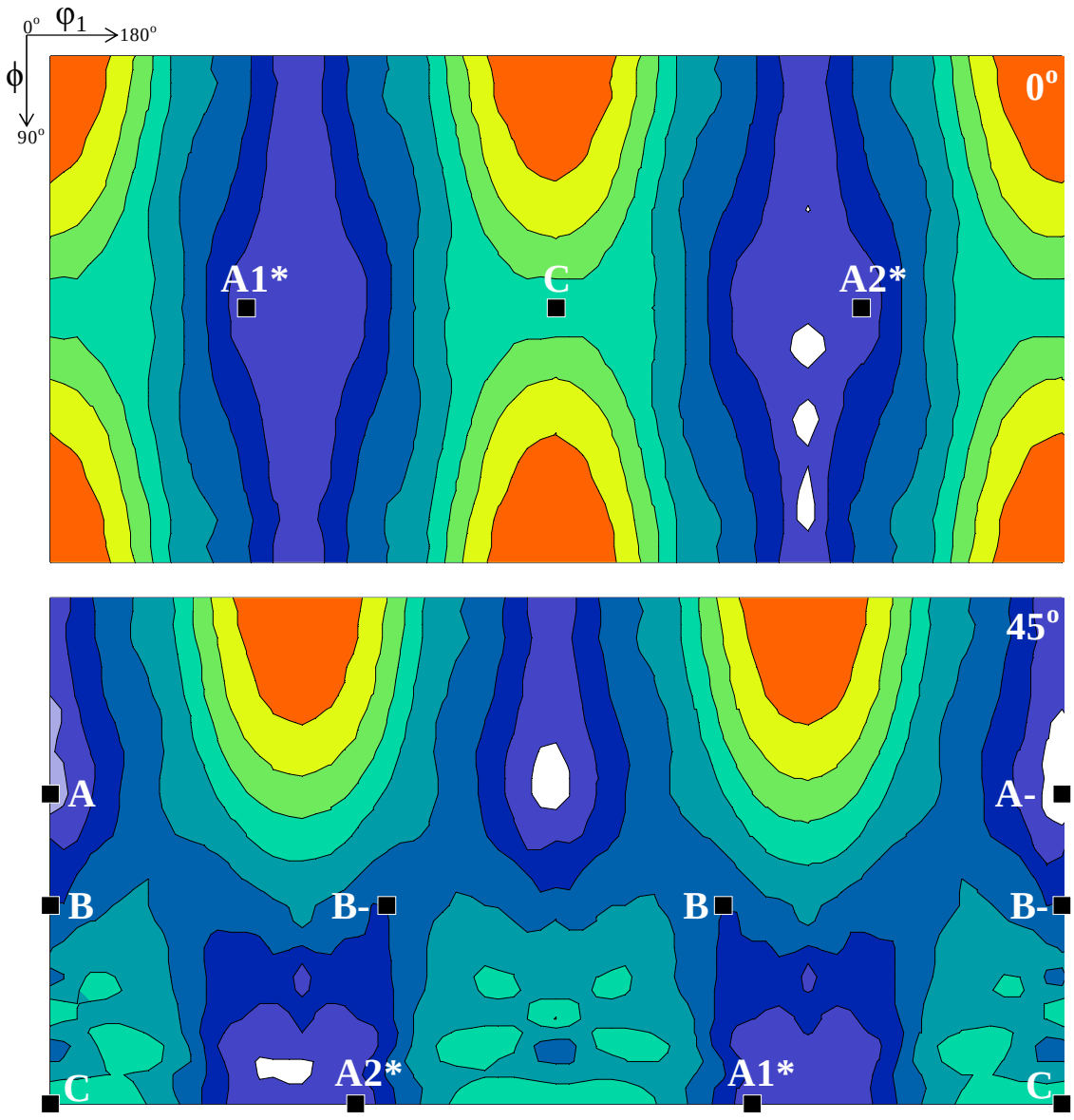

Figure 4.6. Taylor factor map showing the initial distribution of Taylor factors as a function of grain orientation for the austenite phase under torsion using ODF sections φ_2 = 0° and 45°.

The results show that the C component bears the highest Taylor factor amongst all ideal fcc components followed by $B/\overline{B}$, A_1^*/A_2^*, and $A/\overline{A}$ components; showing the hierarchy in a good agreement with the literature data [113, 114].

4.5.2.2. Martensite Texture Evolution

The ideal texture components of a bcc phase observed under torsional deformation were shown in Figure 2.35b in terms of a (110) PF for comparison to the measured texture evolution of the bcc martensite phase. The orientation relationships of these components were also presented in Table 2.2 [89]. The measured bcc martensite (110) PFs are presented as a function of the applied shear strain from T3 to T9 in Figure 4.7. T3 was selected as the lowest deformation level due to the fact that the martensite content below this level was too small to obtain meaningful texture data. These PFs present a clear evolution of bcc torsional deformation texture with increasing shear strains [67, 89].

Similar to the case of austenite, ODFs are calculated for the bcc martensite and presented in Figure 4.8 for a more detailed observation of the texture evolution. Subsequently, the texture intensity evolutions of the ideal bcc texture components are extracted from the ODFs and the results are summarized in Figure 4.9.

The texture intensity changes shown in Figure 4.9 display a more homogeneous distribution of the ideal components at the shear strain of 2.55 (T9) compared to the fcc austenite texture evolution shown in Figure 4.5. Of these components, the **D2** component,

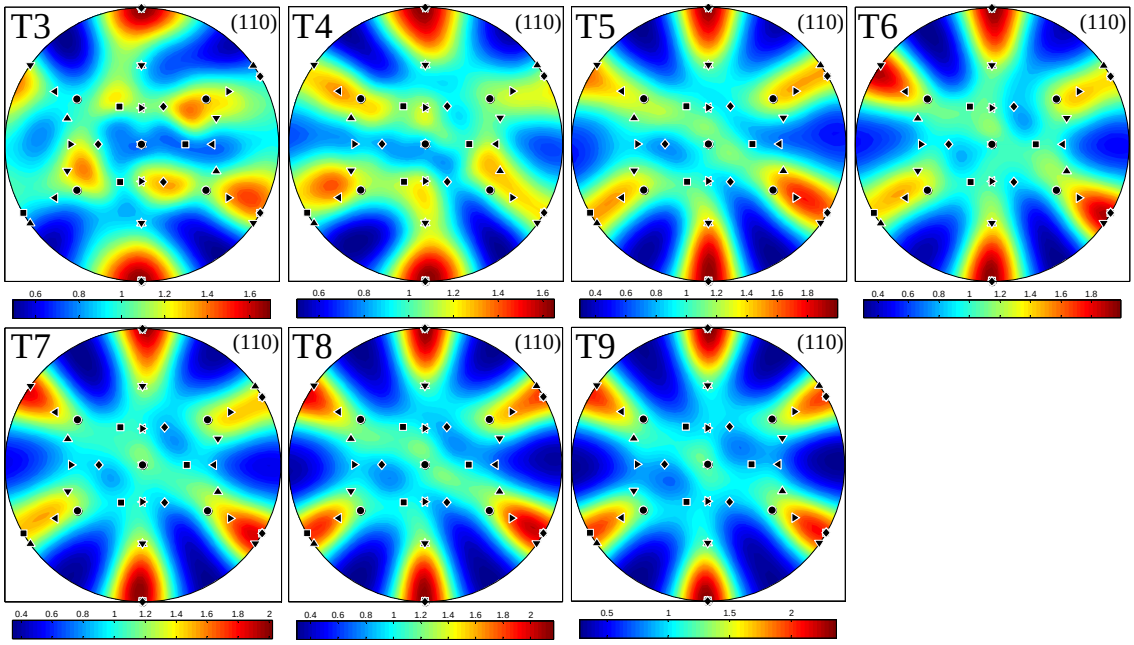

Figure 4.7. (110) pole figures showing the measured bcc martensite texture evolution as a function of the applied shear strain (T3 to T9). The north pole denotes the axial direction (Z) and east, the shear direction (θ).

Figure 4.8. Orientation distribution function (ODF) sections ($\varphi_2 = 0^o$ and $\varphi_2 = 45^o$) showing the qualitative texture evolution of the bcc martensite as a function of shear strain from T3 to T9.

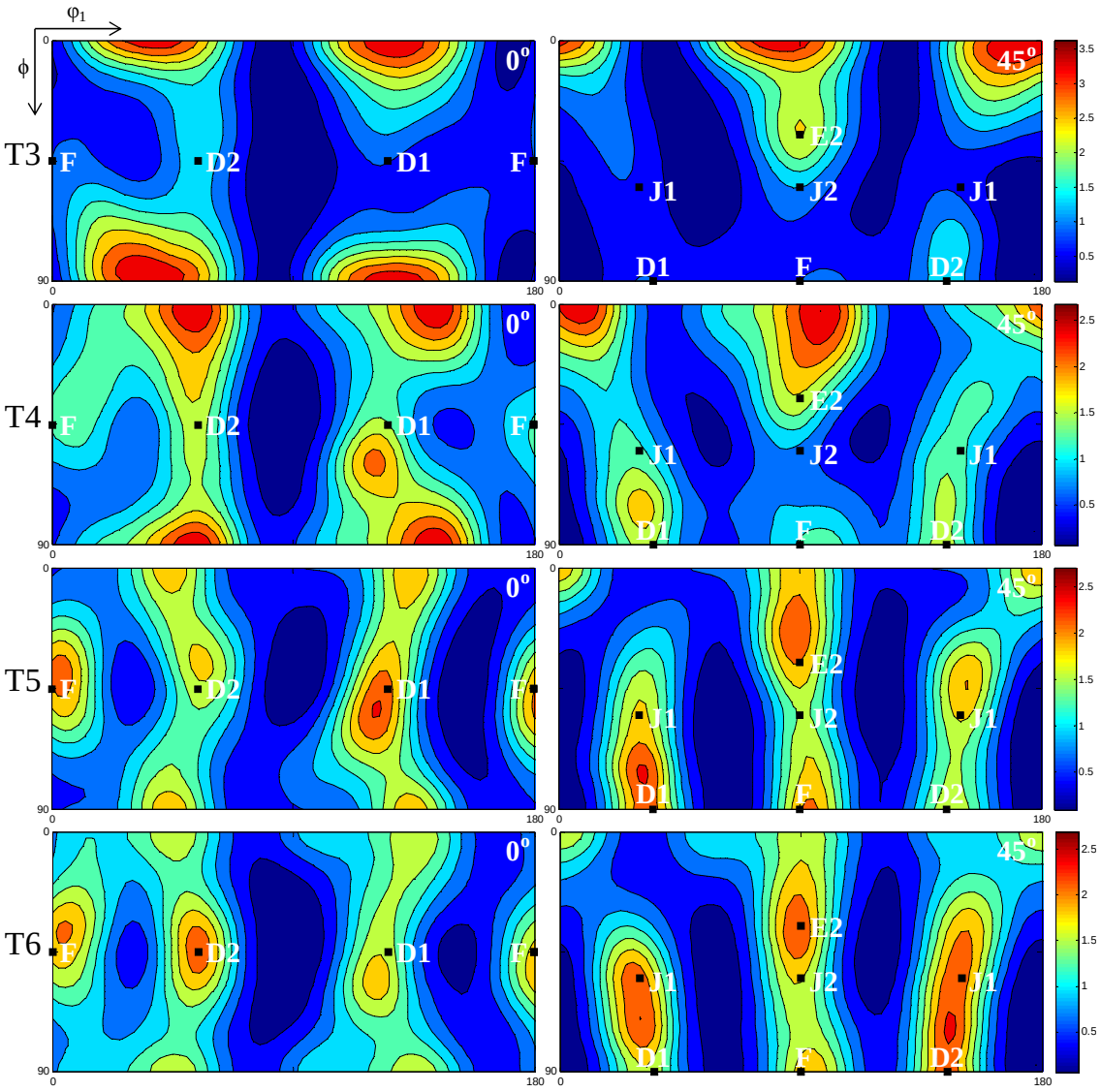

Figure 4.8. Continued.

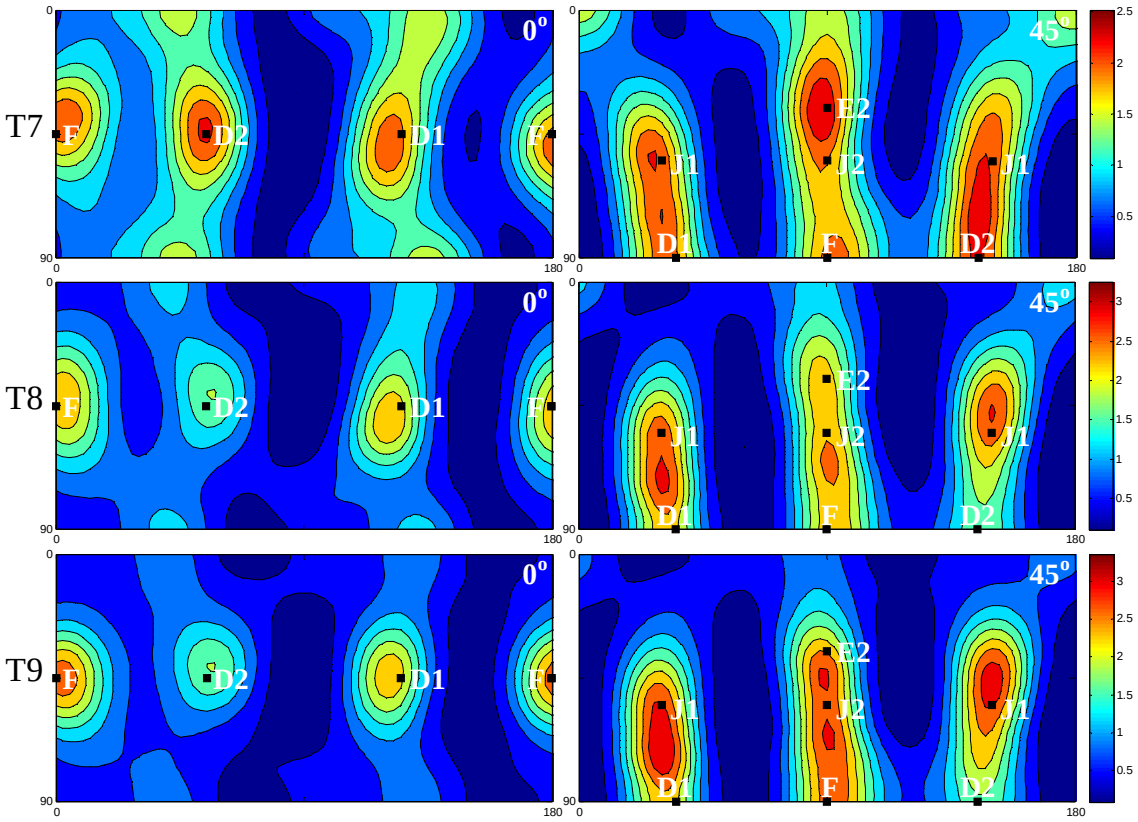

Figure 4.8. Continued.

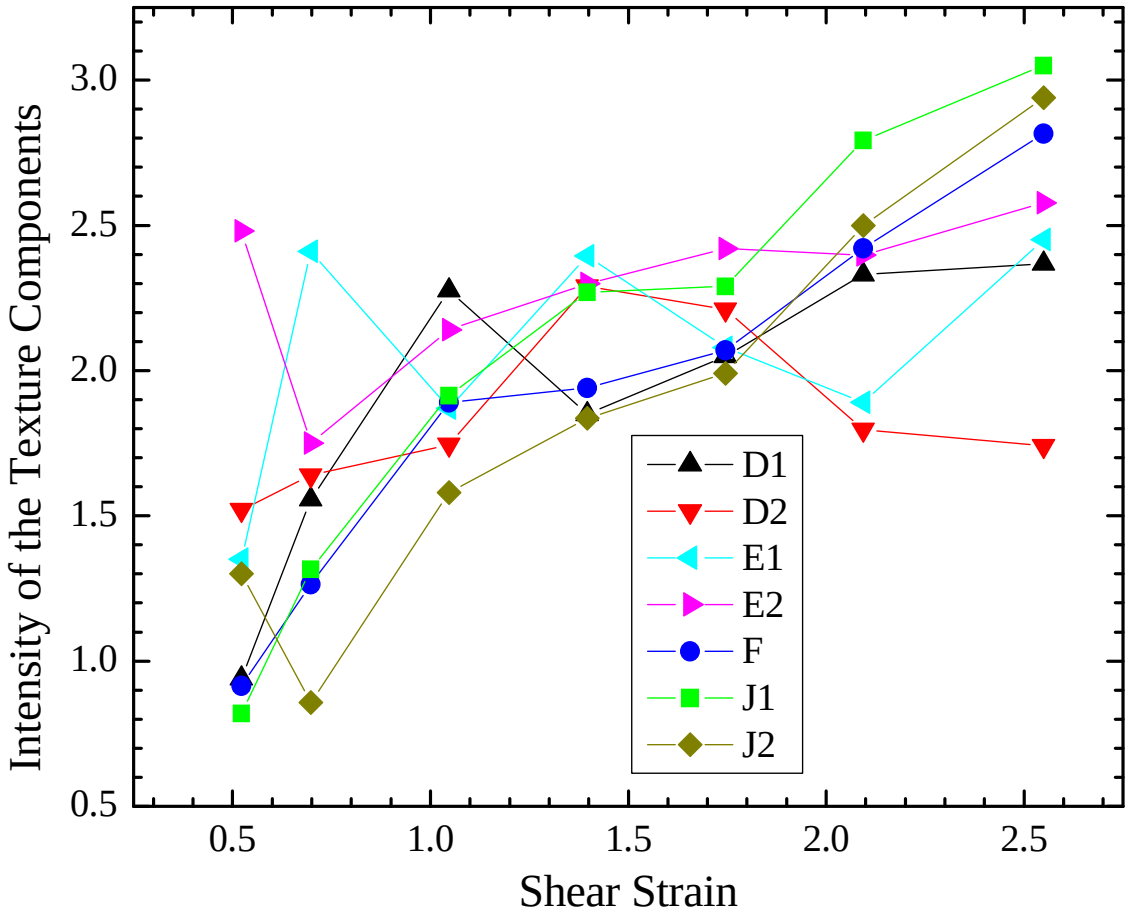

Figure 4.9. The intensity evolutions of the ideal bcc torsion texture components in the bcc martensite phase measured as a function of the applied shear strain.

which shows a decreasing trend at higher shear strains, is of particular importance as it is closely related to the length changes/induced axial forces observed under free/fixed-end torsional deformation conditions, respectively [89]. A more detailed discussion regarding the evolution of the **D2** component will be given in Section 4.6.3.

4.5.3. Phase-Grain Orientation-Texture Relations in the Parent Austenite

The phase, grain orientation, and texture components are mapped through post-processing of the EBSD images obtained from the Zθ plane of the pin samples, Figure 4.1. Two samples, T3 and T6, are selected for further discussion and their respective maps are presented in Figure 4.10. The phase maps are presented in the first column to show the phase distributions of the bcc martensite phase (red) within the austenite grains (green). The distribution of the grain orientations are illustrated in the 'orientation map' using a color scale with the corresponding legend presented in the inverse pole figure. Accordingly, the red grains have their {001} plane normals aligned with the Z-axis; while the blue grains their {111}, and the green their {101}.

As introduced in Table 2.1, grains with specific orientation relations belong to certain ideal texture components ({hkl} plane normals parallel to the Z-axis and <uvw> parallel to θ). Then the texture component maps in Figure 4.10 can be used to reveal the texture component of each grain; e.g., **C** grains marked with purple, **A*** grains with green, etc. Also, the grains of interest are marked with arrows for further discussion in Section 4.6.2.

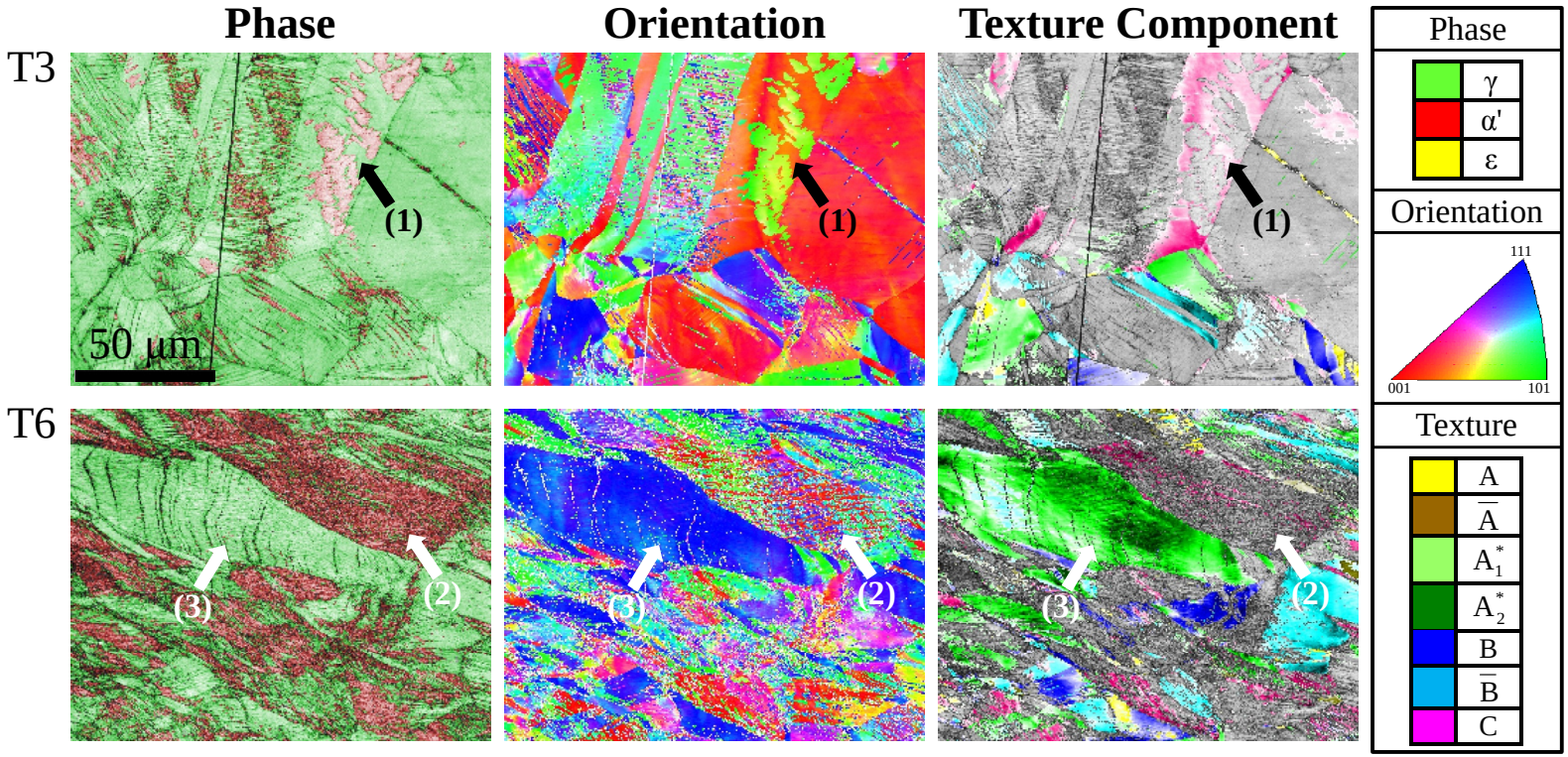

Figure 4.10. Phase, grain orientation, and texture component maps of T3 and T6 obtained from EBSD measurements. The arrows indicate three grains of interest: a partially transformed grain (grain 1) in T3; and two adjacent grains in T6, where one is heavily transformed (grain 2) while the other is not (grain 3). The scale bar corresponds to 50 microns.

4.6. Discussion

4.6.1. fcc Texture Evolution in Single-phase fcc Alloys and Influence of SFE

In previous studies, it was shown that the changes in the SFE can alter the presence and evolution of the ideal texture components as observed in copper-type and brass-type textures with decreasing SFE values [87, 88]. In addition, Hughes et al. [86] reported the influence of SFE on the texture development in various Ni-Co alloys. The SFE reported for the current 304L stainless steel (for the austenite phase) is about 17-20 mJ/m^2 depending on the variations in the composition [53, 64, 115] and lies in between the Ni-60wt.%Co alloy [86] and brass [87, 88].

Table 4.1 summarizes the changes in fcc texture components with increasing applied shear strain for Cu, brass, Ni, and Ni-60% Co, in comparison to the current 304L SS. Let us examine the three key components: **C**, **B**, and $\mathbf{A}_2^*$.

First, the **C** is the dominant component in Cu and also is an important component in brass alloys upon torsional deformation; showing little effect of reducing the SFE from 80 to 10 mJ/m^2, Table 4.1 [67, 85, 87, 88]. On the other hand, according to the work by Hughes et al., while **C** is a dominant component in Ni (SFE = 240 mJ/m^2), it weakens to disappear during deformation of Ni-60%Co alloy with a much lower SFE (20 mJ/m^2) [86]. The dramatic change in the **C** component in the Ni-60%Co alloy was attributed to the planarity in slip character resulting in grain subdivisions and cell blocks [86]. The results of Ni-60%Co [86] conflicts most of the brass texture data e.g., [87, 88, 90] even though it is expected that both Ni and Cu alloys are subjected to a similar change in slip character when alloyed to lower the SFE.

Table 4.1. Torsion texture evolution of various single phase fcc materials with different stacking fault energy (SFE) values. Also included are current results from the 304L stainless steel in which a fcc to bcc phase transformation occurs.

Material	**Crystal Str.**	**SFE (mJ/m^2)**	**Changes in fcc Texture Components with Increasing Shear Strains**				
			$A/\overline{A}$	**A_1^***	**A_2^***	**$B/\overline{B}$**	**C**
Cu [67, 85, 87, 88]	fcc	80 [53]	Weakens	Stronger at lower strains (fixed end)	More intense at large strains (fixed end)	More intense at large/very large strains	Strengthens and becomes the dominant one
Brass [87, 88, 90]	fcc	<10 [53]	Remains as moderate/low	Strengthens	Gradually disappears/Non-existent	Accepted as the dominant one at RT but depends on the alloy content	Strengthens and could become the dominant one
Ni [86]	fcc	240	Weakens	Weakens	Moderate and weakens to random	Moderate	Strengthens and becomes the dominant one
Ni-60% Co [86]	fcc	20	Strengthens	Initially strengthens and plateaus	Weakens in the very early stage/Non-existent	Strengthens and becomes the dominant one	Weakens to random
304L SS (current work)	fcc → fcc+bcc	18 [115]	Strengthens	Strengthens to become the dominant one	Weakens	Strengthens	Strengthens and then significantly weakens to random

The **B** component is another important fcc texture component for torsional deformation in all cases shown in Table 4.1. In addition, it is also shown that **B** component is not very sensitive to the changes in SFE.

While the $\mathbf{A}_2^*$ component remains visible under torsional deformation to a relatively large applied strain in pure Cu [67], its intensity almost vanishes with deformation when the SFE is lowered to brass, Table 4.1. A similar trend was also observed in the pure Ni when the SFE was lowered by alloying with 60% Co [86].

Neither brass nor Ni-60% Co alloy exhibited any phase transformations and the decrease in the $\mathbf{A}_2^*$ component intensity was solely attributed to the lower SFE in these studies [86, 88]. The current study on 304L SS also shows a consistent behavior in that the $\mathbf{A}_2^*$ component intensity decreases significantly with deformation, which can be attributed to the low SFE in the 304L SS, and not necessarily associated with the martensitic phase transformation.

4.6.2. fcc Texture Evolution in 304L SS and Selective Transformation

The martensitic transformation kinetics during torsional deformation of the current 304L stainless steel is illustrated using the bcc transformation rate together with the phase fraction data as a function of the applied shear strain in Figure 4.11a. The transformation rate increases rapidly to a maximum at T5 and decreases rapidly thereafter; making T5 the turning point between these two stages. Figure 4.11b shows the correlation between the transformation rate and the intensity changes of the **C** texture component of the fcc phase.

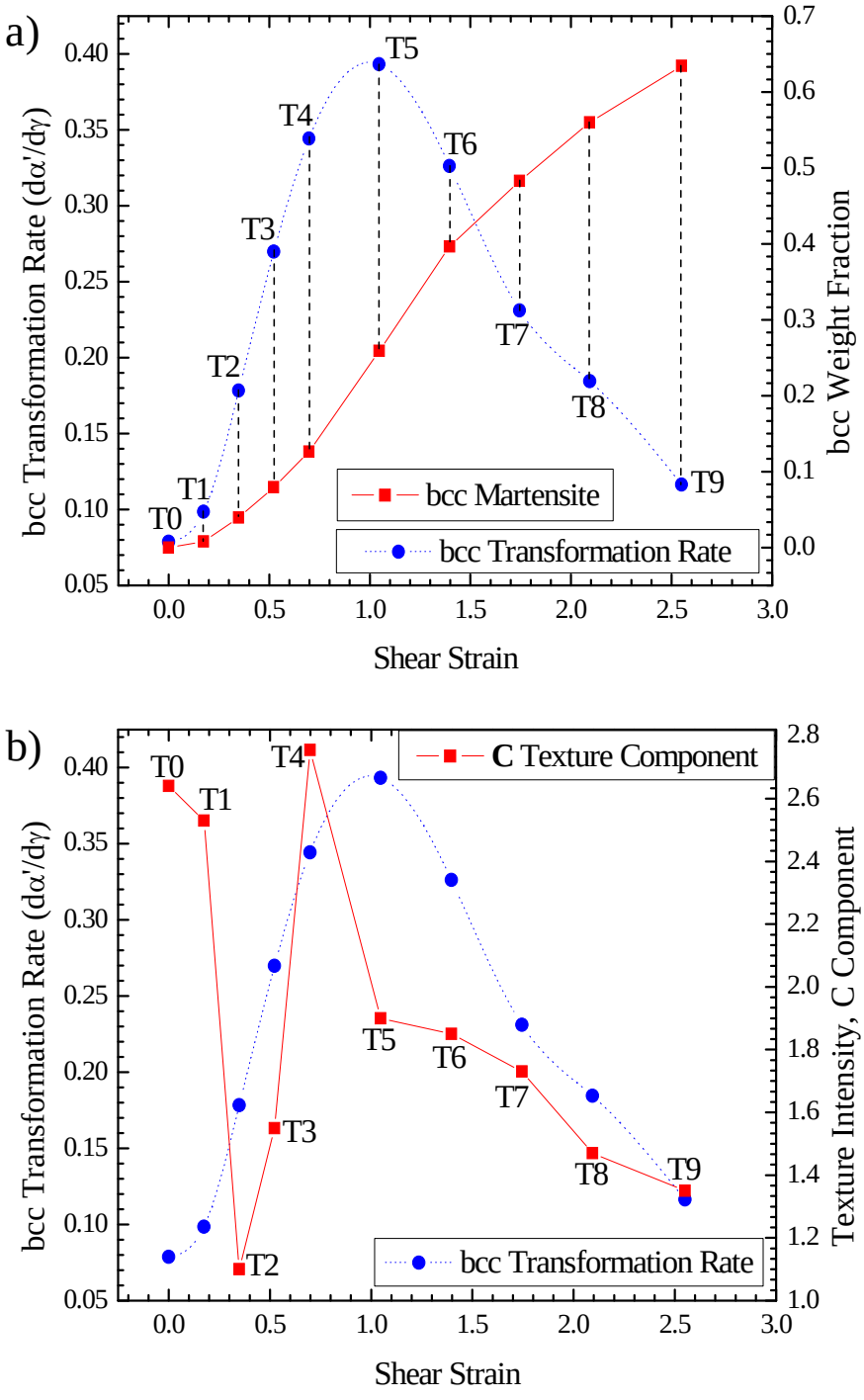

Figure 4.11. a) The relationship between the bcc martensite phase transformation rate and bcc phase fraction evolution and b) bcc transformation rate and the evolution of the intensity of the **C** component as a function of the applied shear strain.

After the breakdown of the initial texture (from T0 to T2), the transformation rate increases with increasing intensity of the **C** component. This behavior continues until the **C** component reaches a maximum intensity at T4. Subsequently, a dramatic decrease is observed in the intensity of the **C** component accompanied by the maximum transformation rate at T5. After reaching the maximum at T5, the transformation rate keeps decreasing along with the diminishing **C** component intensity. This suggests that the transformation rate is closely related to the **C** component in that it could be selectively transforming.

The dramatic downshift in the intensity level passing from T4 to T5 further indicates that the remnants of the grain families in the vicinity of the **C** component have gone under selective transformation, which, in turn, leads to the downshift in the transformation rate with eventually depleting the **C** component.

A set of grains with low Taylor factors contains a slip system favorably oriented with respect to the applied stress; requiring relatively smaller total shears to accommodate the deformation. Consequently, these grains are reported to result in less pronounced deformation-induced substructures compared to grains oriented with higher Taylor factors [116]. This can be illustrated using Eq. (4-1) [117]:

$$\sum \Delta\gamma = M\Delta\varepsilon \tag{4-1}$$

According to this relation the grains with the highest Taylor Factors (M) experience the highest sum of microscopic shears ($\Sigma\Delta\gamma$) for an applied von Mises equivalent macro-strain ($\Delta\varepsilon$) and, therefore, would accumulate the highest amount of dislocation density and stored energy [114, 117]. The Taylor factors from the work of

Jonas et al. [113] for the ideal fcc torsion texture components were reported as $\mathbf{A}/\overline{\mathbf{A}} = 1$, $\mathbf{A}_1^*/\mathbf{A}_2^* = 1.154$, $\mathbf{B}/\overline{\mathbf{B}} = 1.414$, $\mathbf{C} = 1.73$. Similarly, according to our VPSC result, the **C** component has the highest Taylor factor amongst all the ideal austenite texture components, Figure 4.6. Therefore, a set of grains belonging to the **C** component would offer greater number of dislocation intersections that can act as possible nucleation sites for the martensite embryos; and the associated stored energy would supply the highest driving force for the transformation. Accordingly, the grains belonging to the **C** component would be subjected to a preferential phase transformation. Therefore, the typically strong **C** component during torsional deformation of a single-phase alloy would be preferentially consumed for the martensitic transformation in the current specimens resulting in the strong correlation between the transformation rate and the **C** texture evolution.

The transformation-texture relation in the context of preferential transformation was further investigated at the microscopic level using the EBSD results, Figure 4.10. For the T3 specimen, where not much transformation has yet taken place towards the end of the incubation period; the phase map shows that the microstructure consists mostly of austenite grains (green). It also shows that the strain-induced martensite (red) appears predominantly at the shear band intersections. However, it should also be noted that not all shear banded regions transformed to bcc martensite as it is evident in both phase maps of T3 and T6.

Let us further examine the grain marked with the 'arrow 1', Figure 4.10, for the relationship between grain orientation and the transformation. The orientation map of T3

reveals this 'grain 1' (remnants of the parent austenite matrix) to be of (100) type shown in red, i.e., a grain with its (100) plane normal parallel to Z axis. The texture component map shows more details on the grain orientation in that this particular grain (remaining austenite matrix marked with the 'arrow 1') belongs to the **C** component shown in purple, which is a subset of the (100) type whose $[0\bar{1}1]$ is also parallel to the θ direction. Therefore, the T3 results illustrate that the bcc martensite is predominantly appearing on fcc with the **C** texture component, which is consistent with the S-XRD results.

Furthermore, the gray areas in the texture component maps correspond to grains that could not be indexed for any of the ideal fcc texture components. It is naturally expected that the martensite phase will not contribute to any of the listed texture components; thereby, making the detection of the austenite texture relation easier especially at higher deformations, where the austenite grains can be heavily consumed by the martensite phase. It should be noted that very few of the austenite grains observed in the EBSD texture component map are oriented to satisfy an ideal texture component. However, when combined with more statistically meaningful S-XRD data, the EBSD texture component map provides useful microscopic details.

The T6 phase map shows that the "grain 2' has transformed to bcc martensite (mostly red), while 'grain 3' is still fully austenitic (green). The orientation map reveals the untransformed 'grain 3' to be of (111) type suggesting that it belongs to **A** or **A*** type. It is, however, more difficult to distinguish the orientation relationship of the remainder of the austenite matrix in the heavily transformed 'grain 2' due to the presence of the embedded martensite. Nevertheless, as stated previously, the martensite phase will not be

indexed for any of the ideal fcc texture components and, therefore, the detection of the austenite texture relation becomes possible. The result shows the remnants of the austenite matrix in 'grain 2' to be of (100) type (red). Finally, the texture component map reveals that the untransformed 'grain 3' is **A*** type (green), while heavily-transformed 'grain 2' (i.e., the austenite matrix of it) belongs to the **C** type (purple).

In summary, based on the observation of phase, orientation, and texture component maps, the bcc martensites appear at the shear banded regions preferentially in a grain with its (100) plane normals parallel to the Z-axis; but more specifically, in a grain with the **C** texture component, which is a subset of the former with its $[0\bar{1}1]$ parallel to θ as well. This was best illustrated in the case of T6, where 'grain 2' (belonging to the **C** component) was heavily transformed, whereas neighboring 'grain 3' (belonging to one of the **A*** components) remained completely untransformed.

Another texture component of interest is the **B** component, which grows in intensity and becomes a major one in most cases of low-SFE alloys under torsion [86, 87] including the current study. However, when the intensity hierarchy is compared between the Ni-60%Co alloy and current 304L SS (with very close SFE values to each other), there is a significant difference. For the case of Ni-60%Co alloy, the sequence is strong **B** component followed by **A** and $\mathbf{A}_1^*$, whereas for the 304L SS case it is a dominant $\mathbf{A}_1^*$ followed by **A** and **B**. The **A** and **A*** components have the lowest Taylor factors (1 and 1.154) amongst the ideal fcc components [113], Figure 4.6. **B**, on the other hand, lies between the **A**/**A*** and **C** components with a relatively higher Taylor factor (1.414) [113], Figure 4.6. This implies that the **B** component might as well be selectively undergoing

martensitic transformation similar to the **C** component but at a lower rate. Hence, even though it is a general trend that the overall intensities of the **A**, $\mathbf{A}_1^*$, and **B** components all increase with increasing shear strains; selective transformation of the **B** component can hinder its intensity build-up when martensitic transformation is occurring, and result in the observed hierarchy shift in the ideal fcc texture components from a dominant **B** to a dominant $\mathbf{A}_1^*$ in the current alloy. A similar argument was also put forth in the work of Angel [2] where it was suggested that the most energetic grains, such as **C** component in this case, would be consumed first for the martensitic transformation later to be followed by grains with less stored energy, such as **B**, when the most energetic grains start to deplete.

4.6.3. bcc Texture Evolution in 304L SS

Since the parent austenite phase becomes textured through the deformation process, the product martensite is also expected to be textured. Whether the martensite phase only mimics the parent texture through a variant selection mechanism or forms its own deformation texture can be studied through detailed examination of the martensite texture evolution. As stated earlier, the **D2** component is of special interest in this case as it can help understand the course of the bcc texture evolution. In the work of Baczynski et al. [89], it was shown that this particular component is closely related to the type of the torsional deformation, i.e., free- or fixed-end testing. The results they obtained from three different pure bcc materials (namely, Ti IF Steel, Ti-Nb IF Steel, and α-Fe) suggest that under free-end deformation, the **D2** component increases in intensity with increasing

shear strains whereas under fixed-end testing conditions it shows the opposite behavior, i.e., decreases in intensity with increasing shear strains.

The texture intensity evolution of the **D2** component in the present work, Figure 4.9, shows similar behavior as the fixed-end deformation case of pure bcc materials. Based on this 'signature' behavior of the **D2** evolution, it is suggested that even under multi-phase deformation conditions, with the martensite phase gradually being introduced through transformation; the bcc phase forms its own deformation texture rather than simply inheriting the texture of the parent austenite phase.

4.7. Conclusions

A 304L stainless steel, that exhibits the transformation induced plasticity (TRIP) behavior, was studied under torsional deformation at room temperature to investigate the phase transformation behavior and its relations with the texture evolution using the synchrotron x-ray and electron back-scatter diffraction (S-XRD and EBSD) techniques. The conclusions are as follows.

1. During room temperature torsion testing a total bcc martensitic phase fraction of 63.5 wt.% was achieved at a shear strain of 2.55. The transformation rate exhibited a sharp increase in the early stage of deformation showing a peak at the intermediate shear strain of 1.04 followed by a sharp decrease.

2. The texture evolution under torsional deformation was manifested by a dominant $\mathbf{A}_1^*$ followed by **A** and **B** components at the maximum shear strain of 2.55. The **C** component initially increased and then rapidly decreased whereas the dominant components listed above showed a continuous increase with deformation. Overall, the **C** component was very weak reaching almost the random texture level at the maximum shear strain applied.

3. The close correlation between intensity evolution of the fcc **C** texture component $(100)[0\bar{1}1]$ and the rate of martensitic transformation was documented under torsion both with S-XRD and EBSD techniques revealing the preferential transformation of the grains belonging to this component. The slower increase in **B** component with respect to the $\mathbf{A}_1^*$ was also attributed to the selective transformation since this component lies in between the $\mathbf{A}_1^*$ and **C** components in terms of the Taylor factor. This caused the intensity hierarchy shift between the $\mathbf{A}_1^*$ and **B** components. In the current study, the $\mathbf{A}_1^*$ becomes the dominant one unlike the literature results that showed a dominant **B** component during the torsional deformation of low stacking fault energy fcc materials that do not involve any phase transformations.

4. The bcc martensite was observed to develop its own deformation texture rather than inheriting the texture from the parent austenite phase during the transformation according to the characteristics of the **D2** component which is sensitive to the type of torsional deformation, i.e., free-end vs. fixed-end. It was found to decrease in intensity with increasing shear deformation for the current deformation mode of fixed-end torsion,

which is consistent with the deformation texture development of other monolithic bcc materials deformed under the same condition.

Chapter 5 Influence of the Load Character on the Phase Transformation Kinetics and Texture Evolution in a TRIP Steel under Biaxial Loading

Abstract: The martensitic phase transformation kinetics and its relations with the texture evolutions and the deformation/transformation microstructures in the parent austenite phase were studied for a transformation induced plasticity (TRIP) steel under biaxial loading conditions at ambient temperature. The applied loading paths included: simultaneous biaxial torsion/tension, simultaneous biaxial torsion/compression, and stepwise loading of tension followed by torsion. Synchrotron x-ray and electron back-scatter diffraction techniques were used to measure the evolutions of the phase fractions, texture, and microstructures as a function of the applied strains. The influence of loading characters and paths on the changes in martensitic phase transformation kinetics are discussed in the context of texture-transformation relations and preferential transformation mechanisms, effects of axial strains on shear band evolutions, and volume changes associated with the martensitic transformation.

5.1. Introduction

During cold-forming operations conventional steels may require additional processes such as inter-pass annealing in order to achieve the final desired form without premature failure. On the other hand, the TRIP phenomenon can help achieve higher cold deformation levels without the need of additional treatments and, hence, plays an important role in determining the material formability. Therefore, understanding of the factors affecting the transformation kinetics in more realistic forming operations is of significant technical importance. Specifically, the loading-path dependency of phase transformations is one of the important fundamental issues that require further investigations.

Most engineering materials are subjected to a combination of shear and axial forces during manufacturing processes and applications. For instance, in the case of sheet metal forming processes, the local stress state at a point in the material can have any arbitrary combination of shear and tension leading to variations in the phase transformation kinetics at different points in the material; potentially resulting in distortions in the finished product [118]. However, basic studies on the phase transformations under biaxial deformation [47, 100] are limited and the fundamental understanding on the transformation-texture-microstructure relations under combined shear and axial loads is lacking.

In this chapter, the phase transformation kinetics and their relations with the texture evolution as well as the deformation/transformation microstructures under biaxial deformation modes will be discussed in comparison to the torsion case. The biaxial

deformation modes include simultaneous torsion/tension, simultaneous torsion/compression, and stepwise loading of tension followed by torsion. The measurements are performed using synchrotron x-ray and electron back-scatter diffraction techniques (S-XRD and EBSD). The influence of loading characters and paths on the phase transformation kinetics will be discussed in the context of: texture-dependent preferential transformations, shear band evolutions, and volume changes associated with martensitic phase transformation.

5.2. Material and Mechanical Testing

The properties of the 304L stainless steel are presented in Chapter 3. The biaxial tests were performed using various strain paths including biaxial torsion/tension (BT) and biaxial torsion/compression (BC) where the shear and axial strains are applied simultaneously; and stepwise deformation of tension followed by torsion (S). The mechanical tests were performed using the servo-hydraulic MTS multi-axial load frame of the VULCAN beamline at Oak Ridge National Laboratory. The same specimen geometry as in Chapters 3 & 4 was used for the biaxial torsion/tension and stepwise tension followed by torsion cases. The biaxial torsion/compression specimens, on the other hand, had a slightly longer gage length (7 mm) to provide adequate length for the compressive deformation.

All of the applied strains are summarized in Figure 5.1 in terms of applied shear and axial strains for various loading paths studied: torsion (T), simultaneous biaxial torsion/tension (BT), biaxial torsion/compression (BC), and stepwise tension followed by

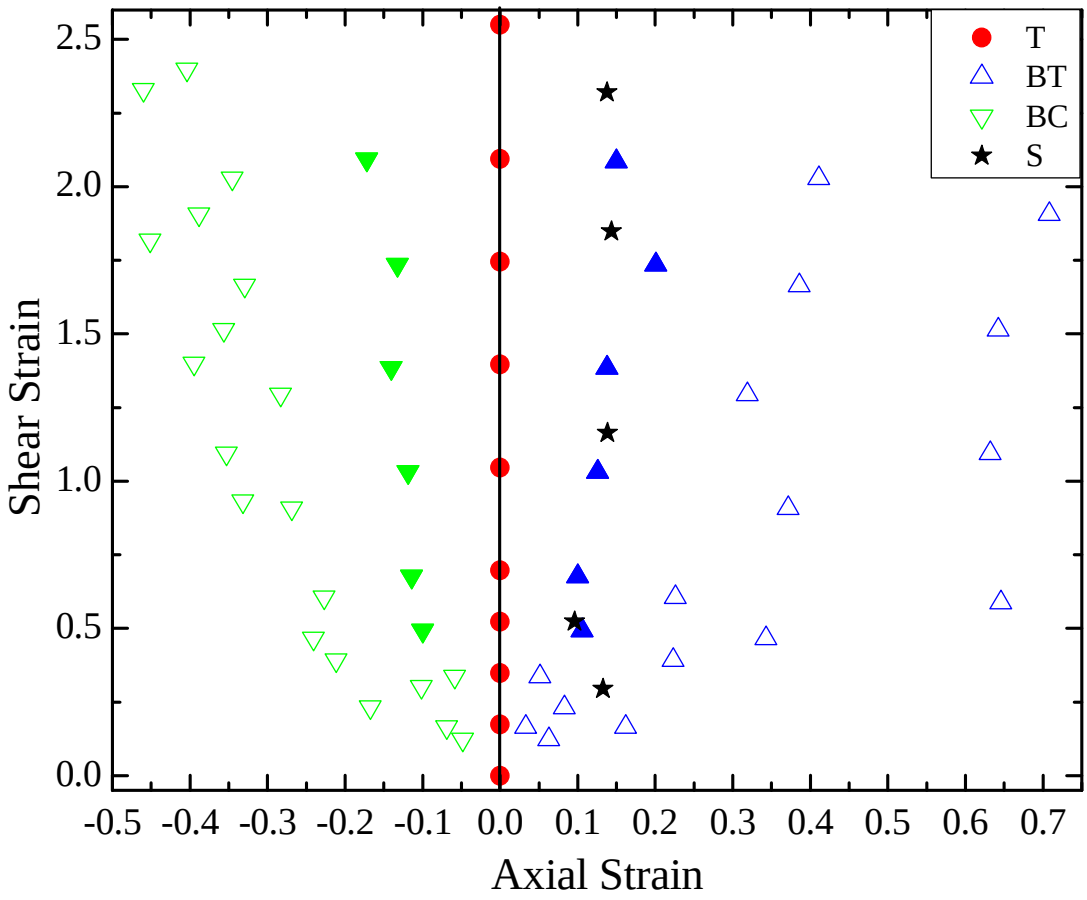

Figure 5.1. The distribution of the shear and axial strains for: torsion (T), simultaneous biaxial torsion/tension (BT) and torsion/compression (BC), and the stepwise tension-torsion (S). Also shown are the selected subsets in filled symbols for direct comparisons.

torsion (S). As described in Chapter 4, first the specimens were deformed under torsion, Figure 5.1, to nine different shear strain levels (γ=0 to 2.55) at an applied equivalent strain rate of $5x10^{-3}$ s^{-1} at room temperature under the fixed-end condition. In order to compare the results from the biaxial cases to the torsional case, von Mises equivalent strains were used. Total equivalent strains of the biaxial tests were matched to the pure torsion cases by adjusting the normal to shear strain ratio using Eq. (5-1) for simultaneous deformations and Eq. (5-2) for the stepwise case,

$$\varepsilon_{eq}=\sqrt{\varepsilon_{ax}^2+\frac{\gamma^2}{3}} \tag{5-1}$$

$$\varepsilon_{eq}=\varepsilon_{ax}+\frac{\gamma}{\sqrt{3}} \tag{5-2}$$

, where ε_{eq} is the total equivalent strain and ε_{ax} is the applied axial strain [102].

The biaxial deformations were carried out using the same equivalent strain rates as the torsion case. However, even though it was possible to control the axial and torsional strain rates separately under stepwise deformation, only one strain rate could be controlled under simultaneous biaxial loading. Accordingly, for the simultaneous loading cases, the torsional equivalent strain rates were set to $5x10^{-3}$ s^{-1} and the resulting axial strain rates were found to be on the order of $x10^{-3}$ s^{-1}.

Finally, subsets of the data are selected from each simultaneous biaxial deformation case with similar applied axial strains (from 0.12 to 0.23 for torsion/tension and -0.1 to -0.17 for torsion/compression), shown as filled symbols in Figure 5.1, for further analyses. The actual shear to axial strain ratios are presented in Table 5.1 along with the specimen designation scheme used in this study.

Table 5.1. The specimen designation showing applied shear/axial strains for: torsion (T), select subsets from biaxial torsion/tension (BT) and torsion/compression (BC), and stepwise tension-torsion (S). Note that the specimen number groups a matched specimen set with a comparable equivalent strain.

Specimen # / Load Type	**0**	**1**	**2**	**3**	**4**	**5**	**6**	**7**	**8**	**9**
T	0	0.17	0.35	0.52	0.70	1.04	1.40	1.74	2.09	2.55
BT	-	-	-	0.49/0.11	0.68/0.10	1.03/0.13	1.38/0.14	1.73/0.20	2.09/0.15	-
BC	-	-	-	0.49/-0.10	0.68/-0.10	1.03/-0.11	1.38/-0.12	1.73/-0.11	2.09/-0.15	-
S	-	-	-	0.29/0.13	0.52/0.10	-	1.16/0.14	-	1.85/0.14	2.32/0.14

5.3. Texture and Phase Fraction Measurements Using Synchrotron X-ray Diffraction

The sample extraction process and the S-XRD measurement scheme for the biaxial case studies are the same as described in Chapter 4 with an exception that the beam size was 300 μm by 500 μm (height x width), which allowed us to illuminate approximately 3600 grains through the tip of the pins.

5.4. Microstructural Characterization Using Electron Back-scatter Diffraction

Following S-XRD measurements, select samples from biaxial torsion/tension (BT3-BT6), and biaxial torsion/compression (BC3-BC6) specimens were characterized using electron back-scatter diffraction (EBSD) to investigate the microstructure-phase transformation-texture evolution relations. The details of the measurements are the same as those described in Chapter 4.

5.5. Results

5.5.1. Phase Transformation Kinetics

5.5.1.1. Simultaneous Biaxial Torsion/Tension and Torsion/Compression

All martensitic phase transformations under simultaneous biaxial torsion/tension (BT) and torsion/compression (BC), in comparison to torsion (T), are presented in Figure 5.2a. During the simultaneous biaxial tests, the applied axial strains (ε_{ax}) are varied between 0.035 to 0.8 in tension and -0.07 to -0.46 in compression, Figure 5.1, while

Figure 5.2. bcc martensite phase evolution as a function of applied equivalent strain under torsional (T) and simultaneous biaxial deformation conditions of torsion/tension (BT) and torsion/compression (BC). a) All measured data from T, BT, and BC cases. b) Selected subsets from BT and BC with a comparable amount of applied axial strains shown in comparison to the results from T. The data points are fit using the Olson-Cohen model and the fitting parameters (α, β) are summarized in the table inset, where n=2.59 for all cases. c) bcc martensite transformation rates of the selected subsets shown in (b).

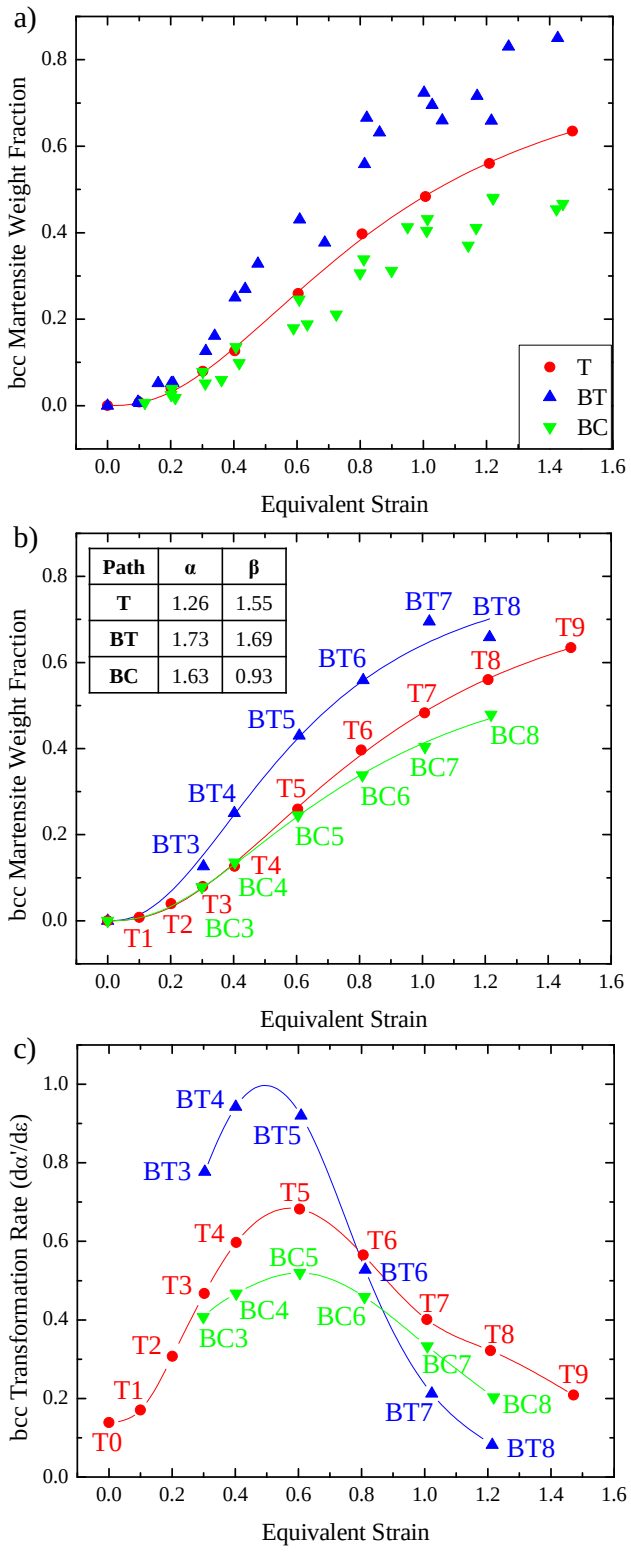

Figure 5.2. Continued

adjusting the shear strains according to Eq. (5-1); to match the equivalent strain (ε_{eq}) levels to the torsional deformation cases. Overall, for a given applied equivalent strain, it is observed that the martensitic phase transformation is enhanced for BT compared to T, whereas it is suppressed under BC.

As mentioned earlier, subsets of the data are selected from each simultaneous biaxial deformation case with comparable applied axial strains for further analyses, Figure 5.1 and Table 5.1. Figure 5.2b shows the bcc martensite evolution of the BT and BC subsets in comparison to the T data.

The peak transformation rate for each deformation mode are observed at similar equivalent strains, Figure 5.2c. The BT case, however, shows the highest peak transformation rate earlier and then diminishes rapidly, while the BC case shows the lowest peak transformation rate that stays below the case of T throughout the strain range studied.

Furthermore, the Olson-Cohen method [20] was used to compare the differences in the phase transformation kinetics by fitting the bcc martensite fraction-plastic strain curves in Figure 5.2b.

$$f^{\alpha'} = 1 - \exp\left\{-\beta\left[1 - \exp(-\alpha\varepsilon)\right]^n\right\} \tag{3-1}$$

The resultant fit parameters (α and β) are shown in Figure 5.2b as an inset. First, all fitting parameters including the exponential constant, n, were allowed to vary for the T case resulting in α=1.26, β=1.55, and n=2.59. For the BT and BC, n was fixed to 2.59 when fitting the data. When the results are compared, the α parameter increases from 1.26

(T) to 1.73 for BT and to 1.63 for BC; whereas the β parameter increases from 1.55 (T) to 1.69 for BT and decreases to 0.93 for BC.

5.5.1.2. Stepwise Tension Followed by Torsion

In the case of S specimens, the samples were subjected to a uniaxial tensile pre-strain of about 0.13 prior to the torsional straining, Figure 5.1 and Table 5.1. Similar to the simultaneous biaxial deformation cases, the equivalent strains under stepwise tension-torsion are calculated using Eq. (5-2) to match the strains to their torsional counterparts. However, since the tensile pre-strains were only on the order of ~0.13, martensitic transformation occurred mainly during the subsequent torsional straining (α'≈1.3 wt.% from tensile pre-strain). Therefore, the bcc phase evolution results observed for the S case are presented in Figure 5.3 as a function of applied shear strains to better illustrate the influence of tensile pre-strains to the transformation kinetics in comparison to the pure torsion. Overall, the amount of bcc martensite is significantly higher for the S case than the T case. Moreover, the incubation period was not as noticeable for the S case unlike the T case.

5.5.2. Texture Evolution

5.5.2.1. Simultaneous Biaxial Torsion/Tension and Torsion/Compression

The austenite texture evolution in terms of ODFs, under BT and BC conditions are presented in Figures 5.4 and 5.5, respectively. The texture evolution under BT shows a dominant $\mathbf{A}_1^*$ component and a **C** component initially growing in strength followed by a decreasing trend much like the results presented under the T case [12].

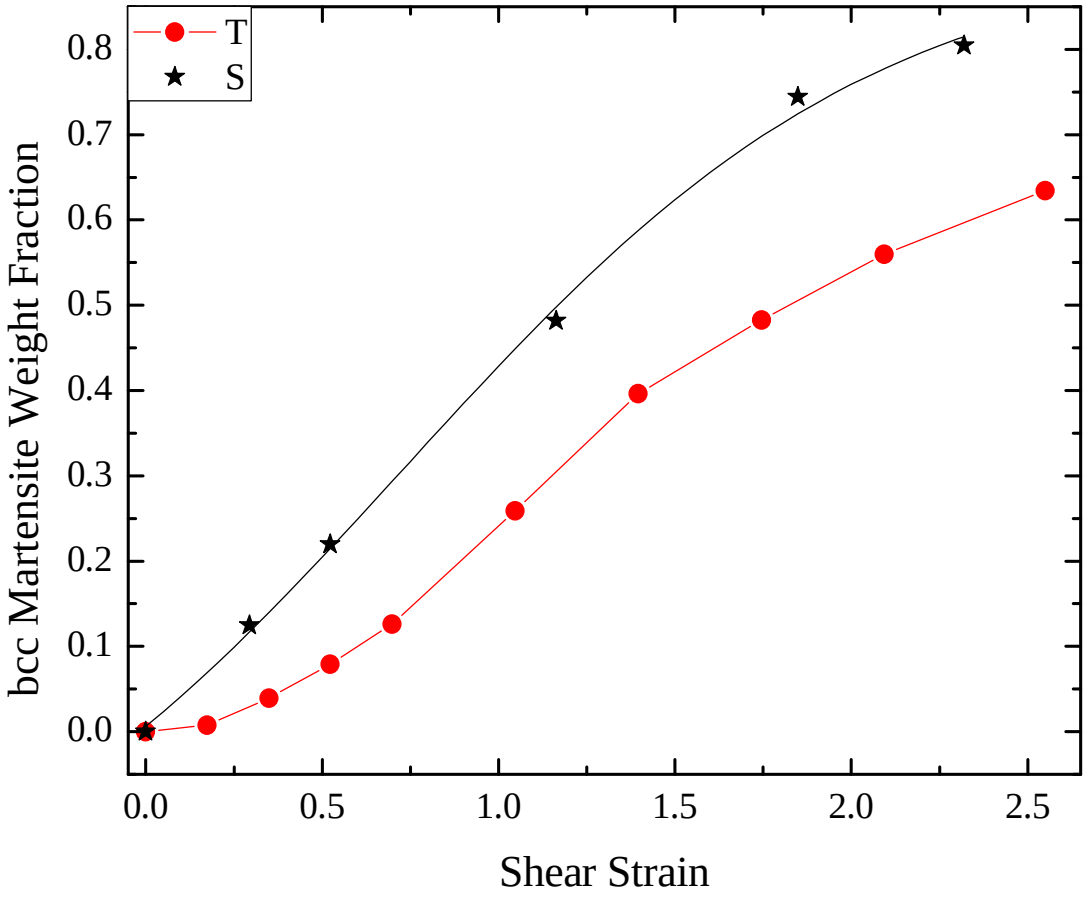

Figure 5.3. bcc martensite phase evolution as a function of applied shear strain under stepwise tension-torsion (S) in comparison to torsion (T). The only difference between the two cases are that the S specimens were subjected to a uniaxial tensile 'pre-strain' of about 0.13 before the subsequent torsion.

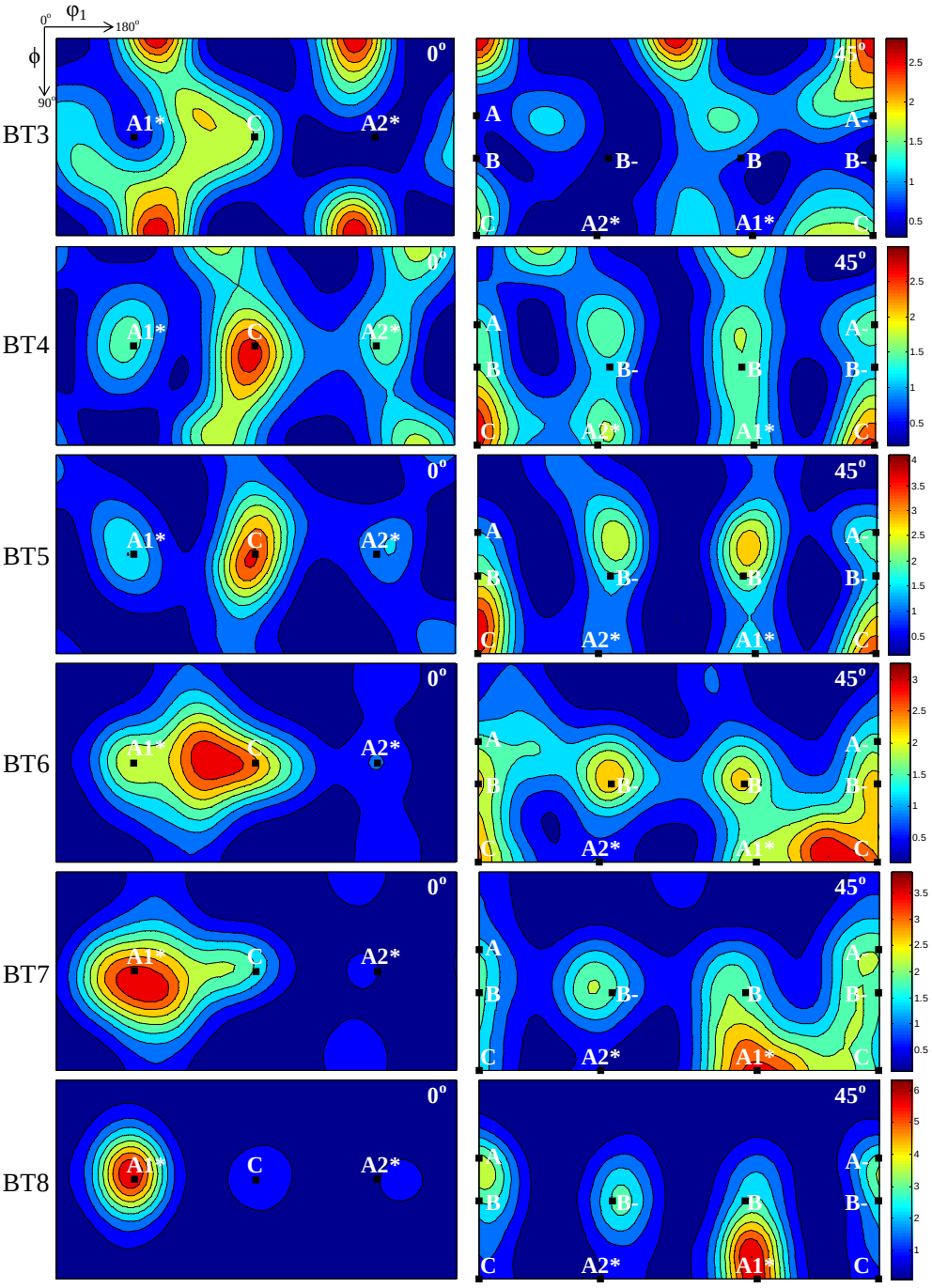

Figure 5.4. Orientation distribution function (ODF) sections (φ_2 = 0° and φ_2 = 45°) showing the qualitative texture evolution of the fcc austenite under biaxial torsion/tension as a function of equivalent strain from BT3 to BT8.

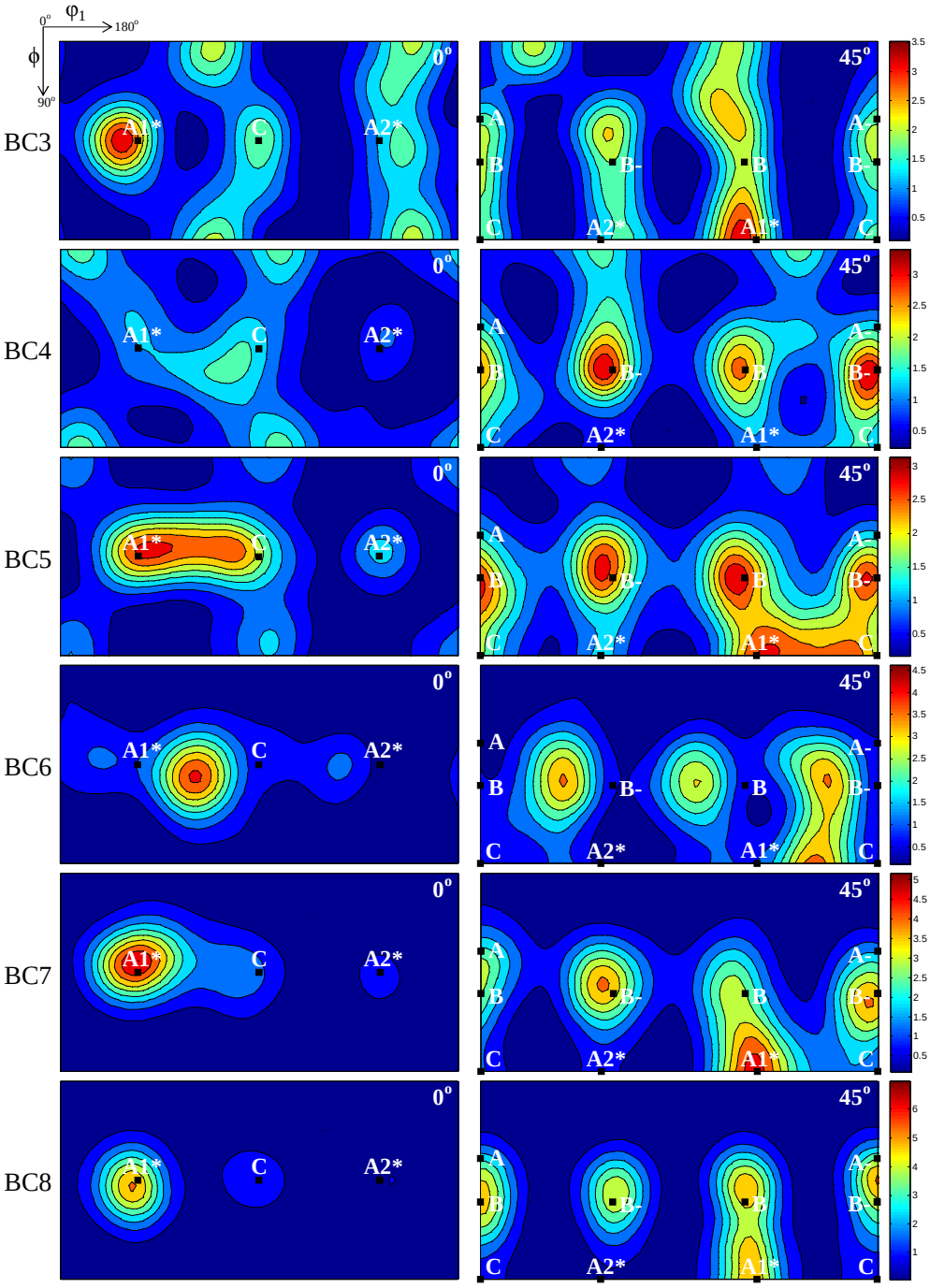

Figure 5.5. Orientation distribution function (ODF) sections (φ_2 = 0° and φ_2 = 45°) showing the qualitative texture evolution of the fcc austenite under biaxial torsion/compression as a function of equivalent strain from BC3 to BC8.

For the BC case, a dominant $\mathbf{A_1^*}$ is also present, however, the **C** component is always weak. The $\mathbf{A_2^*}$ component is insignificant in both cases of BT and BC, whereas the **B** component stands as the second strongest component to $\mathbf{A_1^*}$, to be followed by the **A** component.

As it was presented in the previous chapter, the most dominant texture components are defined as $\mathbf{A_1^*}$, **B**, and **C** for this alloy. The quantitative evolution of texture intensities of $\mathbf{A_1^*}$, **B**, and **C** components for the BT and BC cases are summarized in Figure 5.6b and c, respectively. The texture intensity evolutions under torsional deformation are also presented in Figure 5.6a starting from the as-received state ($\varepsilon_{eq} = 0$) to sample failure ($\varepsilon_{eq} = 1.47$) as a reference.

For the BT subset, Figure 5.6b, the **C** component shows an initial increase from $\varepsilon_{eq} = 0.3$ to 0.6, becoming the dominant one in this strain interval; followed by a continuous decrease similar to the case of T. On the other hand, $\mathbf{A_1^*}$ and **B** intensities show continuous increase resulting in the same component hierarchy as the case of T in the end.

For the BC, Figure 5.6c, the hierarchy of the texture components at the end of the deformation and the general trend of the $\mathbf{A_1^*}$ and **B** components are similar compared to the T and BT cases. The **C** component, however, shows a continuous decrease from the early stage of the deformation. Overall, even though the final intensity hierarchy is not different under the changing deformation modes, the **C**-component intensity evolutions show significant differences and will be further discussed in Section 5.6.1.

Figure 5.6. Intensity evolutions of the key fcc texture components, $\mathbf{A}_1^*$, **B**, and **C**, as a function of applied equivalent strains for a) torsion (T), b) simultaneous biaxial torsion/tension (BT) subset, and c) simultaneous biaxial torsion/compression (BC) subset.

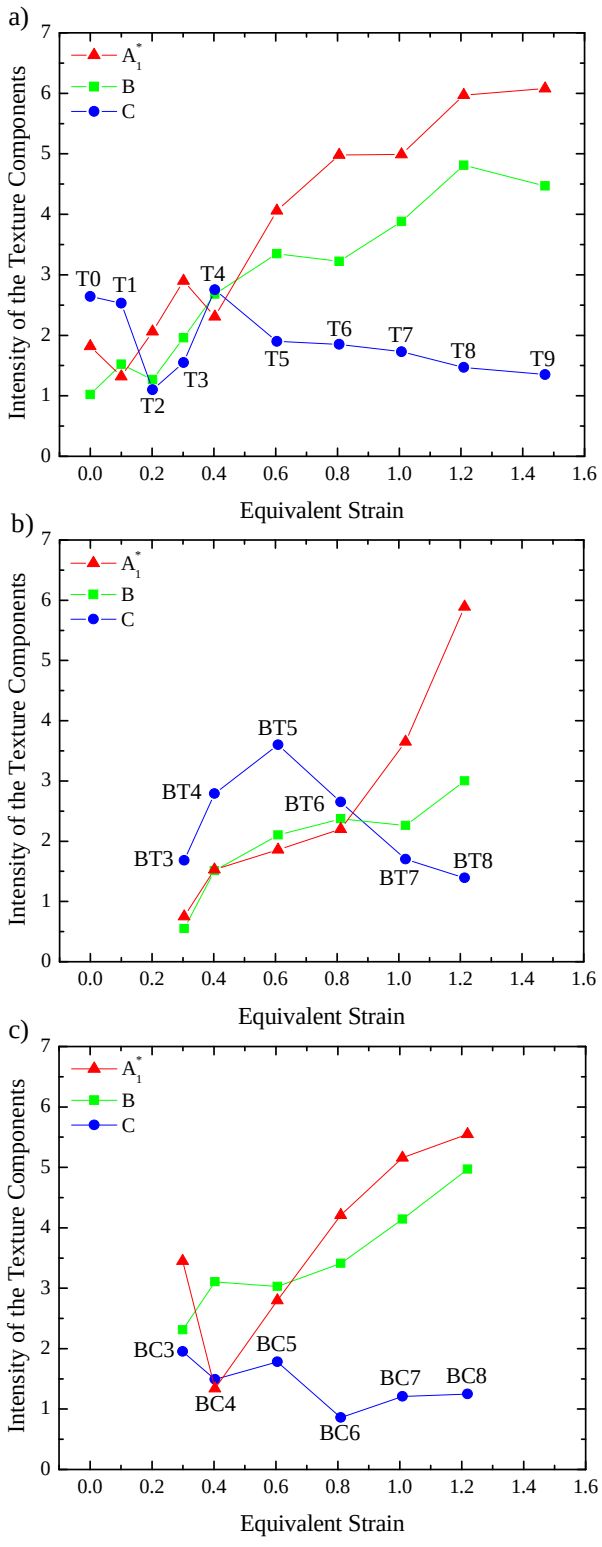

Figure 5.6. Continued

5.5.2.2. Stepwise Tension Followed by Torsion

The ODFs of the S-cases are presented in Figure 5.7. The $\mathbf{A}_1^*$ component is the dominant component, whereas **C** and $\mathbf{A}_2^*$ components are weak/random at S9. These trends closely resemble the ones observed under the torsional deformation. The intensity hierarchy, on the other hand, is manifested as $\mathbf{A}_1^* > \mathbf{A} \geq \mathbf{B} >> \mathbf{C} > \mathbf{A}_2^*$.

5.5.3. Evolution of Deformation and Transformation Microstructures

The evolution of the deformation/transformation microstructures for samples deformed under torsion, biaxial loading torsion/tension and biaxial torsion/compression are characterized using EBSD. The bcc phase evolutions from the EBSD measurements show a reasonable agreement with the S-XRD data, Figure 5.8. Each EBSD data point corresponds to an average of five different measurements and the error bars represent the standard deviation.

The band contrast images are also shown in Figure 5.9. For the pure torsion, T, Figure 5.9 shows that as the deformation progresses from T3 to T6 the corresponding band contrast images become darker; illustrating the evolution of the shear band density with increasing strains. Such trend is more prominent for the biaxial deformation cases. Moreover, for a given deformation level; e.g., comparing T6 with BT6 or BC6; the band contrast density seems to increase from T, BC, to BT. More quantitative comparisons are presented in Figure 5.10.

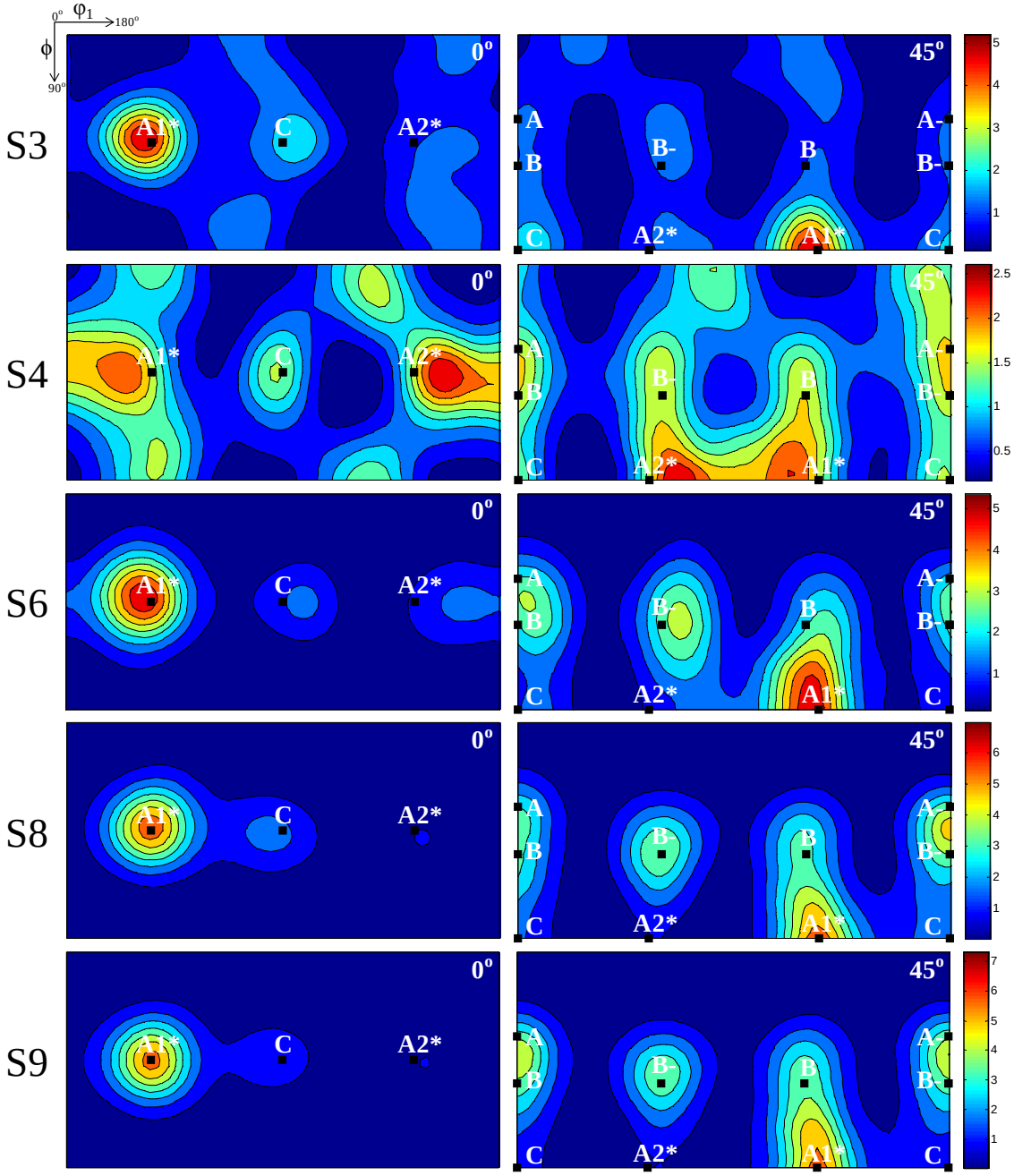

Figure 5.7. Orientation distribution function (ODF) sections (φ_2 = 0° and φ_2 = 45°) showing the qualitative texture evolution of the fcc austenite under stepwise tension-torsion as a function of equivalent strain from S3 to S9.

Figure 5.8. Comparison of the bcc martensite fractions obtained from the EBSD measurements with the results from S-XRD measurements for a) torsion (T), b) simultaneous biaxial torsion/tension (BT), and c) simultaneous biaxial torsion/compression (BC). Each data point is an average of five different measurements and the error bars correspond to their standard deviations.

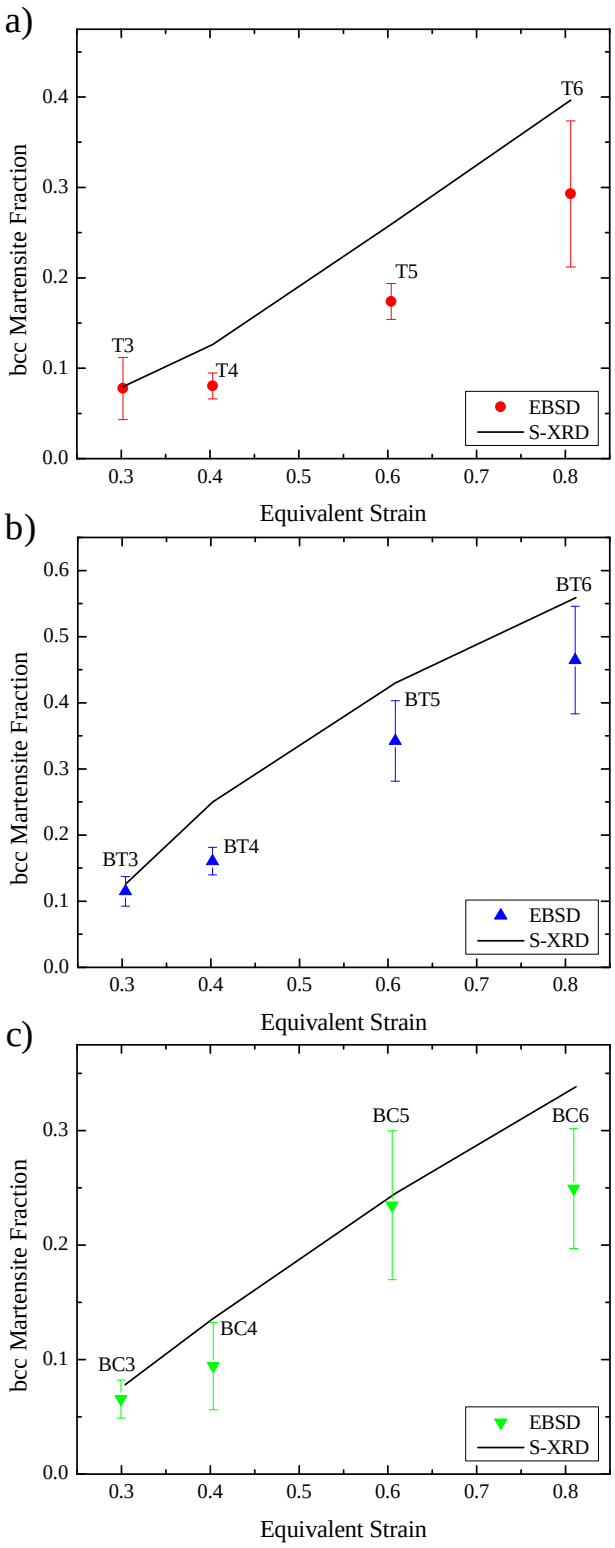

Figure 5.8. Continued.

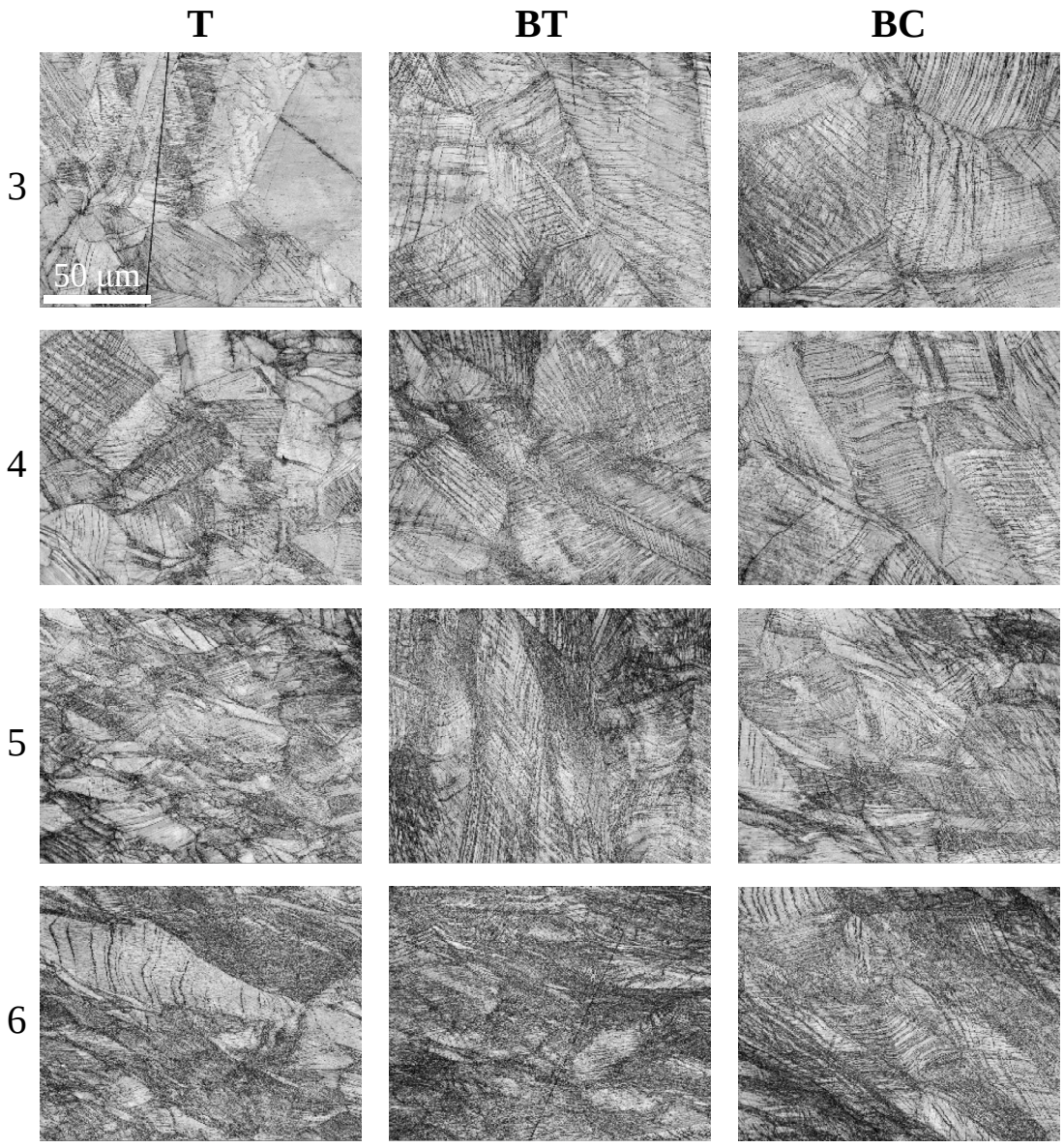

Figure 5.9. Band contrast images measured using EBSD. The columns correspond to the applied loading paths: torsion (T), simultaneous biaxial torsion/tension (BT), and simultaneous biaxial torsion/compression (BC). The rows correspond to the specimen numbers denoting the matched equivalent strain levels. For example, T3, BT3, and BC3 were all subjected to $\varepsilon_{eq} \approx 0.3$. The scale bar corresponds to 50 microns.

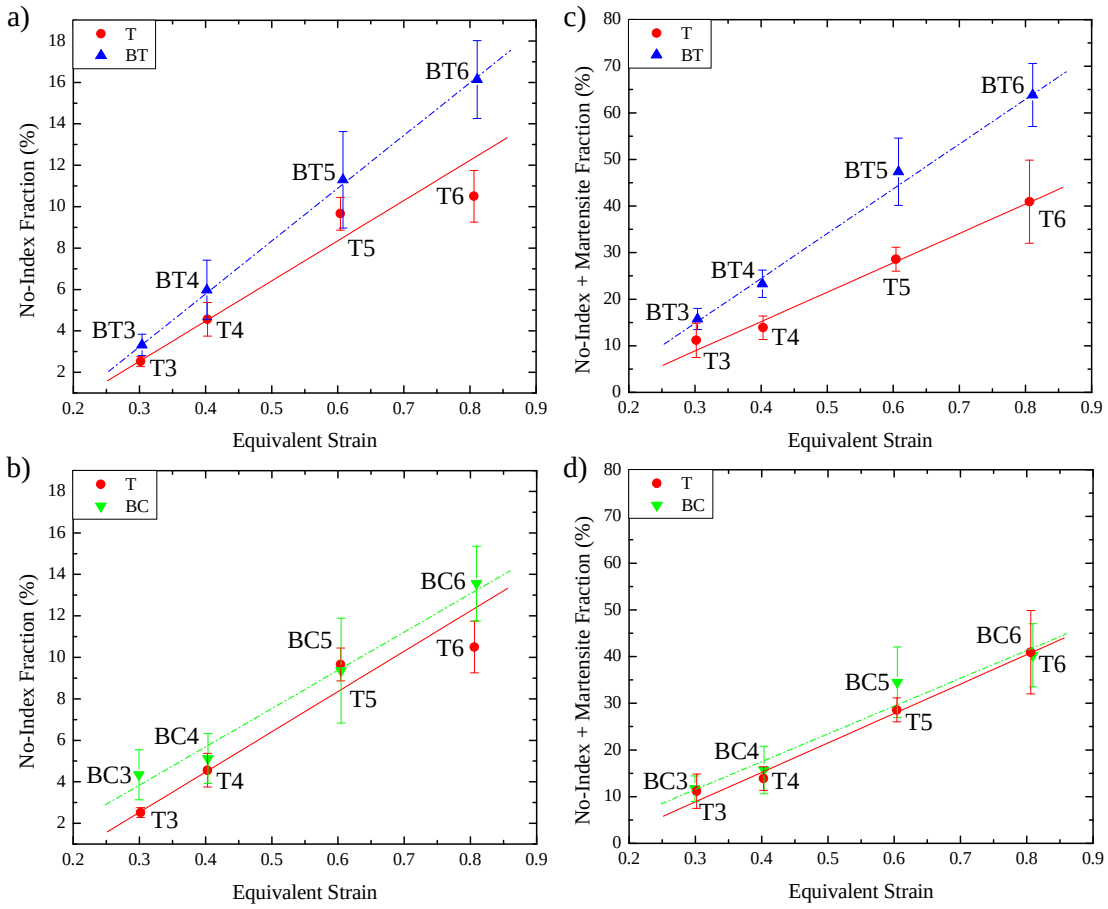

Figure 5.10. Quantitative 'No-Index' and 'bcc Martensite' fractions measured using EBSD as a function of applied equivalent strains. The evolution of the 'No-Index' fractions for: a) BT and T and b) BC and T. The evolution of the 'No-Index + Martensite' fractions for: c) BT and T and d) BC and T. Each data point corresponds to an average of five different measurements and the error bars correspond to their standard deviations. The lines are linear fits to the data points.

It should be noted that microstructural features such as grain boundaries and microscopic shear bands cannot be indexed during the phase identification using the EBSD. Instead, they are registered as the 'No-Index' fraction [116, 119]. Therefore, assuming a similar average grain size for T, BT, and BC, the 'No-Index' fraction can be used to quantify the evolution of shear bands. The evolution of the 'No-Index' fractions are presented for the BT and BC sets as a function of applied equivalent strains in comparison to T in Figures 5.10a and b, respectively. A total of five different areas were measured for each specimen to improve the statistics, and for all the EBSD measurements, same scan parameters; i.e., electron-beam energy, beam size, and scan steps; were used. The results show that, in all three cases, the 'No-Index' fraction increases almost linearly with the strain. Moreover, for a given strain, the 'No-Index' fraction increases from T, BC, to BT.

The 'No-Index' fraction, however, will only indicate the amount of shear bands that has not yet undergone martensitic transformation. Therefore, in order to probe the total amount of transformed and remaining shear bands, the sum of the 'No-Index' and the martensite fractions are also presented in Figures 5.10c and d for the BT and BC sets, respectively. The evolution of shear bands and their significance for the martensitic transformation kinetics will be discussed along with the results from the Olson-Cohen analysis in Section 5.6.1.

5.6. Discussion

5.6.1. Martensitic Transformation Kinetics under Biaxial Deformation

The correlation between the **C** texture component evolution and the martensitic phase transformation rate was also observed for biaxial torsion/tension (BT) and torsion/compression (BC) cases, Figures 5.11a and b.

In Figure 5.11a, a good correlation between the transformation rate and the **C** intensity evolution is observed for the BT case similar to the T case. Moreover, the **C** intensity levels are higher under BT compared to T, which is also accompanied by a relatively higher peak transformation rate as well as the amount of the martensite formed for a given applied equivalent strain. The addition of tensile strains during the BT may have caused this as tensile deformation for this alloy yields a (100)/(111) type texture in the axial (Z) direction as evidenced by the inverse pole figure (IPF) measured for a sample deformed under uniaxial tension to ε=0.35, Figure 5.12a. Since the **C** component is also a (100) type texture, i.e., has the (100) plane normals parallel to the axial Z direction; added tension is then expected to enhance the formation of the **C** component.

The BC subset, on the other hand, yields the least amount of martensite accompanied by the lowest transformation rate, which is also consistent with its very low **C** intensity development, Figure 5.11b. From the perspective of compression texture evolution, compressive deformation of the current alloy yields a (110) type texture in the axial direction as evident from the IPF measured for a sample deformed to ε=-0.25, Figure 5.12b.

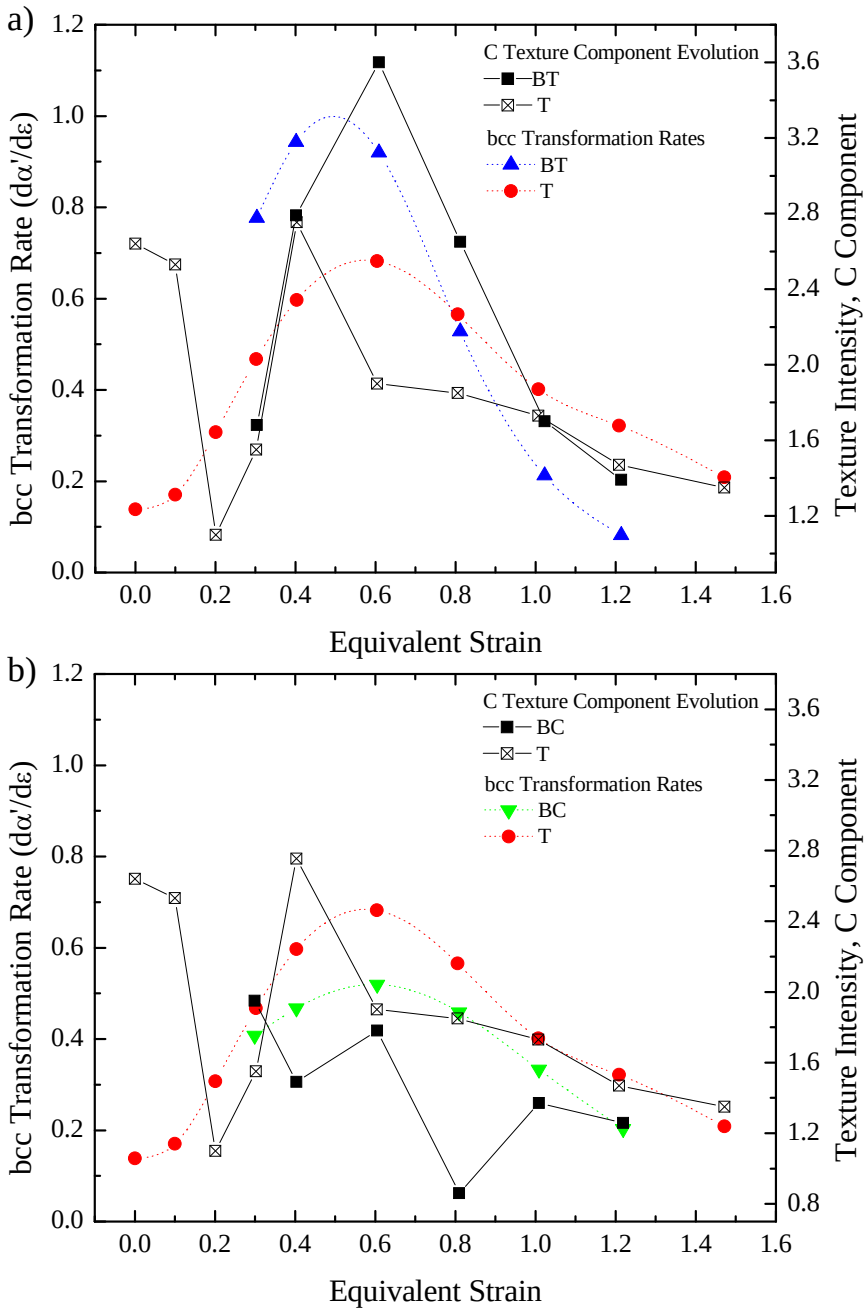

Figure 5.11. The correlation between the bcc transformation rate and the evolution of the **C** texture component intensity as a function of the applied equivalent strain for: a) simultaneous biaxial torsion/tension (BT) and b) simultaneous biaxial torsion/compression (BC) in comparison to torsion (T).

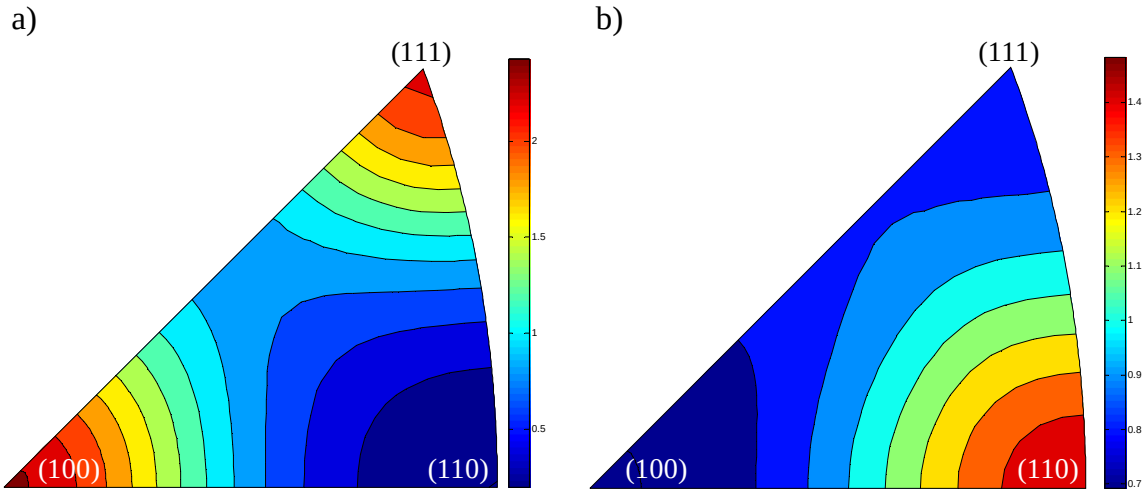

Figure 5.12. Inverse Pole Figures (IPF) measured from the axial direction, Z; showing the austenite texture evolution under a) tensile deformation of $\varepsilon = 0.35$ and b) compressive deformation of $\varepsilon = -0.25$.

Therefore, the addition of compressive texture component does not affect the overall texture evolution in an advantageous way for the preferred phase transformation.

In addition, the evolution of shear bands and their relations with martensitic transformation are also investigated for the biaxial deformation cases, since intersections of microscopic shear bands, e.g., stacking-fault bundles, are considered to be effective sites for the nucleation [105].

The Olson-Cohen (O-C) analysis [20], inset table in Figure 5.2b, suggests that the increase in the bcc martensite fraction under BT condition is related both to the increase in the rate of shear band formation (α) and the higher probability that their intersections will generate a martensite embryo (β), compared to torsion [12]. On the other hand, even though the O-C analysis suggests an increase in the rate of shear band generation (α) under BC, a lesser probability that their intersections will generate an embryo (β) suppresses the martensite formation in comparison to torsion.

The formation of shear bands is a way of accommodating the deformation and, therefore, the number of shear bands will increase with increasing strains regardless of the deformation mode as observed in Figures 5.9, 5.10a and b. However, the rate of shear band formation will be dependent on the loading condition. For instance, the 'No-Index' fraction increases more rapidly under BT compared to T, Figure 5.10a; indicating a higher rate of shear band generation in accordance with the higher α parameter from the O-C analysis. Furthermore, Figure 5.10c reveals an overall shift in the total amount of shear band volume (transformed+untransformed) in favor of BT compared to T; thus, consistent with the higher β parameter of BT from the O-C fits.

The evolution of the 'No-Index' fraction under BC also suggests a slightly higher amount of microscopic shear bands in comparison to T, Figure 5.10b; again consistent with the O-C analysis. However, when the total transformed and untransformed volumes are compared in Figure 5.10d, the difference between BC and T is marginal, which is in a good agreement with the O-C analysis, where the lower β of the BC case counters the higher α.

Overall, the results suggest that, in comparison to torsion, inhibiting factors for martensitic transformation are in operation under BC, whereas it is the opposite under BT even though both biaxial subsets were subjected to similar magnitudes of axial and shear strains as summarized in Figure 5.1 and Table 5.1.

5.6.2. Effects of Axial Strains on the Transformation Kinetics

Ungar et al. [120] has reported the differences in deformation microstructures under torsion and tension using x-ray diffraction line profile analysis and transmission electron microscopy. A multiple slip is reported to be dominant under tension, whereas double slip is dominant under torsional deformation. The differences in deformation micro-mechanics resulted in different dislocation densities, where a higher dislocation density was observed under torsion. However, dislocations move mainly in parallel planes under torsion (near to the plane of torsional shear stress) and, therefore, dislocation intersections occur less frequently compared to tension [104].

The intersection of microscopic shear bands, such as stacking-fault bundles, are an effective site for strain-induced martensitic transformation. A wide stacking fault is formed by either interaction between unlike dislocations or interaction between mobile

dislocations and pre-existing dislocations of a different slip system. After the formation of such wide stacking faults, the active dislocations passing on slip planes near the stacking fault can easily be extended, thereby, greatly increasing the frequency of overlapping stacking faults and possible nucleation sites for the bcc martensite [121].

Moreover, dislocation annihilation can take place by the combination of dislocations of the same Burgers vector with opposite characters. Therefore, as there are more active slip systems (N), i.e., different Burgers vectors, for a given dislocation density the average separation between the dislocations of the same Burgers vector and of opposite character will increase by a factor of N in comparison to a case where only one kind of dislocation is active [122].

Therefore, the introduction of simultaneous axial strains is expected to stimulate the transformation by increasing the probability of dislocation intersections over the already large dislocation density supplied by torsion through introducing unlike dislocations and dislocations of a different slip system via multi-slip. Also, the more prominent the presence of axial strains, the lower the rate of dislocation annihilation would be compared to pure torsion. Accordingly, in comparison to torsion, the martensitic transformation kinetics would enhance under BT as has been shown earlier.

From this perspective, a similar behavior in martensite transformation kinetics is expected under BC, but the experimental results presented otherwise. The transformation of the austenite to bcc martensite is accompanied by a volume expansion (as much as 4%) [118, 123-125]. As it was introduced in Chapter 2, according to Bain formation of a bcc lattice from the fcc structure requires a distortion in the parent phase, also called the

Bain-distortion, $\underline{\underline{B}}$. It can be expressed using the lattice constants of the parent fcc (a_{fcc}) and product bcc phases (a_{bcc}) according to Eq. (2-7) and the associated volume change can be calculated using Eq. (2-8) [37, 38].

$$\underline{\underline{B}} = \begin{bmatrix} \sqrt{2}a_{bcc}/a_{fcc} & 0 & 0 \\ 0 & \sqrt{2}a_{bcc}/a_{fcc} & 0 \\ 0 & 0 & a_{bcc}/a_{fcc} \end{bmatrix} \tag{2-7}$$

$$\frac{dV}{dV_0} = \det(\underline{\underline{B}}) \tag{2-8}$$

The 304L stainless steel used in this study only constituted of the austenite phase in the as-received 'stress-free' state. Therefore, in order to investigate the volume changes accompanying the martensitic transformation, the lattice parameters obtained from the deformed/transformed specimens were used to illustrate the point. The Rietveld refinements using full Debye-Scherrer rings from all rotations (ω), provided the lattice parameters to be on the order of a_{fcc} = 3.59 and a_{bcc} = 2.87 angstroms for specimens T1 to T9. The corresponding volume changes ranged from 2% to 2.5% based on the calculations from all of the samples deformed under torsion (T1 to T9).

Further, the shape change accompanying the transformation can be described by a deformation gradient $\underline{\underline{F'}}_T$, Eq. (5-3); consisting of a shear, γ, and a dilatational component, Δ, parallel and perpendicular to the habit plane, respectively [38].

$$\underline{\underline{F'}}_T = \begin{bmatrix} 1 & \gamma & 0 \\ 0 & 1+\Delta & 0 \\ 0 & 0 & 1 \end{bmatrix} \tag{5-3}$$

Consequently, the surrounding phases, i.e., the parent austenite and the already-formed martensite, would put each newly-forming martensitic embryo under compression; signifying the effect of volumetric constraints on martensitic transformation. For instance, the M_S temperature of very thin specimens are reported to be higher than that of bulk specimens as the grains in bulk specimens are subjected to more constraints [125]. As a result, even though the compressive strains would not have the same effect on every martensite variant, these inhibiting factors could be responsible for the lower probability of martensite embryo generation regardless of the higher amount of shear band formation in the BC case.

In summary, the effects of the application of simultaneous axial strains over the torsional strains on the martensitic phase transformations are found to be two-fold. The application of simultaneous tensile strains enhances the martensitic transformation both through supplying more favorably oriented grains for transformation and higher rate of shear band generation as well as an increased probability of martensite embryo formation at their intersections. On the other hand, the application of simultaneous compressive strains not only inhibits the formation of favorably oriented grains for transformation but also reduces the probability of martensite embryo generation even with the increased shear band density; thereby hindering the martensitic transformation in comparison to torsion.

5.6.3. Enhanced Martensitic Transformation Kinetics under Stepwise Deformation

The axial pre-strains ranged from 0.1 to 0.14 in the case of stepwise tension-torsion (S), Figure 5.1 and Table 5.1; and the increase in martensite weight fraction ranged from 4.5 in S3 to 18 wt.% in S9 compared to their torsional counterparts, Figure 5.3. On the other hand, the reference sample deformed under tension to a similar strain (ε=0.12) produced only 1.3 wt.% bcc martensite. Therefore, the active mechanism responsible for the observed increase in bcc martensite phase fraction under stepwise tension-torsion (S) should not be solely related to additional bcc fraction introduced by the tensile pre-strains.

Deformation of the austenite phase creates the necessary defect structure, which acts as embryos for the martensite phase [3]. In the work of Spencer et al. [126], the application of plastic pre-strains at room temperature increased the rate of martensitic transformation under secondary tensile deformation at 77K; which was induced by the high density of pre-existing dislocations introduced by the preliminary deformation at room temperature.

Similarly, in the case of stepwise tension-torsion (S), even though the initial tensile pre-strains do not introduce a significant amount of bcc martensite, they can aid in the formation of the necessary defect structure to overcome the initial incubation period for the transformation [2, 3, 127, 128]. This, in turn, could result in enhanced martensitic transformation under subsequent torsional deformation. This also manifests itself in the

almost linear increase in bcc martensite fraction starting from the earlier levels of deformation under stepwise deformation compared to torsion, Figure 5.3.

5.7. Conclusions

A 304L stainless steel that exhibits the transformation-induced plasticity (TRIP) effect was studied under simultaneous biaxial deformation modes of torsion/tension and torsion/compression, and stepwise loading of tension followed by torsion at room temperature to investigate strain-state dependent phase transformation kinetics and its relations with the texture evolution and the deformation microstructures using synchrotron x-ray diffraction (S-XRD) and electron back-scatter diffraction (EBSD) techniques. The conclusions are as follows.

1. The martensitic transformation kinetics was enhanced under biaxial torsion/tension, whereas it was suppressed under biaxial torsion/compression when compared to pure torsion for a given applied equivalent strain. The application of stepwise tension followed by torsion also enhanced the martensitic transformation similar to the biaxial torsion/tension case.

2. The texture evolution of the parent austenite phase under all deformation conditions was manifested with a dominant $\mathbf{A}_1^*$ component. Under simultaneous biaxial torsion/tension the **C** component intensity initially increased in strength followed by a decreasing trend similar to torsion. However, for the simultaneous biaxial

torsion/compression the **C** component was always very weak. As for the stepwise tension-torsion, the **C** component was always close to the point of depletion. The **B** component, on the other hand, was the second strongest component to $\mathbf{A}_1^*$ for all the cases.

3. Martensitic transformation rate under simultaneous biaxial torsion/tension showed a close relation with the **C** component evolution similar to the case of torsion in terms of the preferred transformation. Moreover, higher **C** intensity levels were observed under torsion/tension compared to torsion, which was accompanied with a higher peak transformation rate. The torsion/compression, on the other hand, yielded the least amount of transformation along with the lowest transformation rate consistent with the lowest **C** intensity levels observed.

4. The Olson-Cohen analysis showed that both the rate of shear band generation (α) and the probability that a shear band intersection will generate a martensite embryo (β) increased under simultaneous biaxial torsion/tension when compared to torsion. On the other hand, even though the analysis also suggested an increase in α under simultaneous biaxial torsion/compression, β decreased compared to torsion. This behavior was also confirmed by shear band analysis using EBSD measurements. The suppression on volume increase associated with martensitic transformation was attributed to this behavior under torsion/compression as compressive forces could oppose the necessary volume expansion during the transformation.

5. The enhanced transformation observed under stepwise tension-torsion was attributed to the initial tensile deformation producing the necessary defect structure in the austenite phase required for martensitic embryos to nucleate, thereby, overcoming the incubation period and accelerating the transformation under subsequent torsional deformation. An additive effect of bcc martensite formed under tensile pre-strains was found to be of minor importance. The **C** component reached depletion at a faster rate than pure torsion, which is consistent with the enhanced martensitic transformation during the secondary torsional deformation.

Chapter 6 Summary and Conclusions

In this study a commercial 304L stainless steel (0.022 C, 0.03 Co, 18.18 Cr, 0.14 Cu, 1.54 Mn, 0.11 Mo, 0.076 N, 8.55 Ni, 0.026 P, 0.0117 S, 0.29 Si and balance Fe) that exhibits the transformation induced plasticity (TRIP) behavior was studied under various loading conditions. The load paths included pure torsion, simultaneous biaxial loadings of torsion/tension and torsion/compression, and stepwise loading of tension followed by torsion in addition to a baseline study of uniaxial tension and compression. Synchrotron x-ray and electron back-scatter diffraction techniques (S-XRD and EBSD) were used to probe the phase transformations-microstructure-texture evolution relations in the deformed specimens.

Under torsional deformation, nine specimens were used (T1-T9) to cover the entire plastic deformation range from γ_{T1}=0.17 to γ_{T9}=2.55. The radial position dependent phase transformations were monitored for all the specimens and an Olson-Cohen type model was found to satisfactorily fit the experimental results thereby also showing the linear variation of plastic strains through the radius of the torsionally-deformed solid cylindrical specimens to be reasonable.

The phase transformation kinetics under torsional deformation was investigated using the near-surface data from all the deformed specimens. The transformation kinetics was related to the texture evolution in the parent austenite phase in terms of preferential phase transformation mechanisms. It was revealed that the grains belonging to the **C** component, $(100)[0\bar{1}1]$, were preferentially transforming followed by the grains with the **B** orientation, $(11\bar{2})[1\bar{1}0]$. This was related to the high Taylor factors these orientations have, which translated into having a higher driving force for martensitic transformation

as well as more nucleation sites for martensite embryos. The bcc martensite phase, on the other hand, developed its own deformation texture rather than simply inheriting one from the austenite.

As for the biaxial deformation cases, the strain-induced martensitic transformation showed enhanced kinetics under biaxial torsion/tension and stepwise tension-torsion cases, while exhibiting slower kinetics under biaxial torsion/compression compared to torsion. From the texture perspective, the **C** component intensity was enhanced under biaxial torsion/tension and weakened under biaxial torsion/compression consistent with the higher and lower martensitic transformation amounts they yielded, respectively.

Furthermore, the Olson-Cohen analysis revealed higher rate of shear band generation under both torsion/tension and torsion/compression compared to torsion, the intersections of which could act as favorable nucleation sites for martensite embryos. The analysis also showed that the probability of a shear band intersection generating a martensitic embryo increase under torsion/tension and decreased under torsion/compression in comparison to torsion. These results were further supported by quantitative investigation of deformation/transformation microstructures via EBSD. Accordingly, benefitting both from the increase in the rate/amount of shear band formation and the increased probability that their intersections would generate a martensitic embryo, the phase transformation kinetics were enhanced under torsion/tension in comparison to torsion. The decrease, on the contrary, under biaxial torsion/compression was attributed to the volume changes associated with martensitic transformation; where austenite (fcc) to martensite (bcc) transformation is accompanied

by an increase in the volume, which the compressive force works to counter, i.e., lowering the probability of martensitic embryo generation despite the higher rate of shear band formation in comparison to torsion.

Finally, the increase under stepwise tension-torsion was attributed to the tensile pre-strains creating the defect structure required for the initiation of martensitic transformation thereby overcoming the initial incubation period and accelerating the phase transformation under secondary torsional deformation.

REFERENCES

[1] S.A. Kulin, M. Cohen, B.L. Averbach, JOM-J Met, 4 (1952) 661-668.

[2] T. Angel, J Iron Steel I, 177 (1954) 165.

[3] S.S. Hecker, M.G. Stout, K.P. Staudhammer, J.L. Smith, Metall Trans A, 13 (1982) 619-626.

[4] R.P. Reed, Acta Metall, 10 (1962) 865.

[5] M.C. Mataya, M.J. Carr, G. Krauss, Mater Sci Eng, 57 (1983) 205-222.

[6] T. Mukai, M. Yamanoi, H. Watanabe, K. Higashi, Scripta Mater, 45 (2001) 89-94.

[7] T. Mukai, M. Yamanoi, K. Higashi, Mater Trans, 42 (2001) 2652-2654.

[8] W.J. Kim, C.W. An, Y.S. Kim, S.I. Hong, Scripta Mater, 47 (2002) 39-44.

[9] V.F. Zackay, E.R. Parker, D. Fahr, R. Busch, ASM Trans Q, 60 (1967) 252.

[10] P. Jacques, Q. Furnemont, A. Mertens, F. Delannay, Philos Mag A, 81 (2001) 1789-1812.

[11] V. Randle, O. Engler, Introduction to Texture Analysis - Macrotexture, Microtexture & Orientation Mapping, CRC Press, 2000.

[12] E. Cakmak, H. Choo, K. An, Y. Ren, Acta Mater, 60 (2012) 6703-6713.

[13] K.X. Tao, D.W. Brown, S.C. Vogel, H. Choo, Metall Mater Trans A, 37A (2006) 3469-3475.

[14] R.K. Ray, J.J. Jonas, Int Mater Rev, 35 (1990) 1-36.

[15] R.K. Ray, J.J. Jonas, M.P. Butronguillen, J. Savoie, ISIJ Int, 34 (1994) 927-942.

[16] P. Hedstrom, U. Lienert, J. Almer, M. Oden, Scripta Mater, 56 (2007) 213-216.

[17] N.J. Wittridge, J.J. Jonas, Acta Mater, 48 (2000) 2737-2749.

[18] M. Humbert, B. Petit, B. Bolle, N. Gey, Mater Sci Eng A-Struct, 454 (2007) 508-517.

[19] J.A. Venables, Philos Mag, 7 (1962) 35.

[20] G.B. Olson, M. Cohen, Metallurgical Trans, A 6 (1975) 791-795.

[21] E.C. Oliver, P.J. Withers, M.R. Daymond, S. Ueta, T. Mori, Appl Phys A-Mater, 74 (2002) S1143-S1145.

[22] R.E. Reed-Hill, R. Abbaschian, Physical Metallurgy Principles, Third ed., PWS-Kent Publishing Company, Boston, 1992.

[23] M.A. Meyers, K.K. Chawla, Mechanical Behavior of Materials, Prentice-Hall, Inc., New Jersey, 1999.

[24] E. Hornbogen, Physical Metallurgy of Steels, in: R.W. Cahn (Ed.) Physical Metallurgy, North-Holland Publishing Company, Netherlands, 1974.

[25] J.W. Christian, Phase Transformations, in: R.W. Cahn (Ed.) Physical Metallurgy, North-Holland Publishing Company, Netherlands, 1974.

[26] A.K. Sinha, Ferrous Physical Metallurgy, Butterworths, Stoneham, MA, 1989.

[27] G.B. Olson, M. Cohen, J Less-Common Met, 28 (1972) 107.

[28] J.R. Patel, M. Cohen, Acta Metall, 1 (1953) 531-538.

[29] A.A. Lebedev, V.V. Kosarchuk, Int J Plasticity, 16 (2000) 749-767.

[30] Z. Nishiyama, Martensitic Transformation, Academic Press, New York, 1978.

[31] P.M. Kelly, Acta Metall, 13 (1965) 635.

[32] J.W. Brooks, M.H. Loretto, R.E. Smallman, Acta Metall, 27 (1979) 1839-1847.

[33] J.W. Brooks, M.H. Loretto, R.E. Smallman, Acta Metall, 27 (1979) 1829-1838.

[34] N. Gey, B. Petit, M. Humbert, Metall Mater Trans A, 36A (2005) 3291-3299.

[35] T. Suzuki, H. Kojima, K. Suzuki, T. Hashimoto, M. Ichihara, Acta Metall, 25 (1977) 1151-1162.

[36] G.B. Olson, M. Cohen, Metall Trans A, 7 (1976) 1897-1904.

[37] E.C. Bain, T Am I Min Met Eng, 70 (1924) 25-46.

[38] F. Marketz, F.D. Fischer, Comp Mater Sci, 3 (1994) 307-325.

[39] M.S. Wechsler, D.S. Lieberman, T.A. Read, T Am I Min Met Eng, 197 (1953) 1503-1515.

[40] R. Lagneborg, Acta Metall, 12 (1964) 823.

[41] K.X. Tao, H. Choo, H.Q. Li, B. Clausen, J.E. Jin, Y.K. Lee, Appl Phys Lett, 90 (2007).

[42] Y. Tomota, H. Tokuda, Y. Adachi, M. Wakita, N. Minakawa, A. Moriai, Y. Morii, Acta Mater, 52 (2004) 5737-5745.

[43] K.X. Tao, J.J. Wall, H.Q. Li, D.W. Brown, S.C. Vogel, H. Choo, J Appl Phys, 100 (2006).

[44] S. Cheng, X.L. Wang, Z.L. Feng, B. Clausen, H. Choo, P.K. Liaw, Metall Mater Trans A, 39A (2008) 3105-3112.

[45] N. Jia, Z.H. Cong, X. Sun, S. Cheng, Z.H. Nie, Y. Ren, P.K. Liaw, Y.D. Wang, Acta Mater, 57 (2009) 3965-3977.

[46] P. Hedstrom, L.E. Lindgren, J. Almer, U. Lienert, J. Bernier, M. Terner, M. Oden, Metall Mater Trans A, 40A (2009) 1039-1048.

[47] P.J. Jacques, Q. Furnemont, F. Lani, T. Pardoen, F. Delannay, Acta Mater, 55 (2007) 3681-3693.

[48] S. Cheng, Y.D. Wang, H. Choo, X.L. Wang, J.D. Almer, P.K. Liaw, Y.K. Lee, Acta Mater, 58 (2010) 2419-2429.

[49] D. Goodchild, W.T. Roberts, D.V. Wilson, Acta Metall, 18 (1970) 1137.

[50] Lecroise.F, A. Pineau, Metall Trans, 3 (1972) 387.

[51] G.L. Huang, D.K. Matlock, G. Krauss, Metall Trans A, 20 (1989) 1239-1246.

[52] P.J. Jacques, J. Ladriere, F. Delannay, Metall Mater Trans A, 32 (2001) 2759-2768.

[53] G.E. Dieter, Mechanical Metallurgy, SI Metric ed., McGraw Hill, 1983.

[54] B.E. Warren, E.P. Warekois, Acta Metall, 3 (1955) 473-479.

[55] R.P. Reed, R.E. Schramm, J Appl Phys, 45 (1974) 4705-4711.

[56] X. Tian, Y.S. Zhang, Mater Sci Eng A-Struct, 516 (2009) 73-77.

[57] L.G. Martinez, K. Imakuma, A.F. Padilha, Steel Res, 63 (1992) 221-223.

[58] J. Unfried-Silgado, L. Wu, F.F. Ferreira, C.M. Garzon, A.J. Ramirez, Mater Sci Eng A-Struct, 558 (2012) 70-75.

[59] S. Curtze, V.T. Kuokkala, A. Oikari, J. Talonen, H. Hanninen, Acta Mater, 59 (2011) 1068-1076.

[60] A. Dumay, J.P. Chateau, S. Allain, S. Migot, O. Bouaziz, Mater Sci Eng A-Struct, 483-84 (2008) 184-187.

[61] N. Ohkubo, K. Miyakusu, Y. Uematsu, H. Kimura, ISIJ Int, 34 (1994) 764-772.

[62] R.E. Schramm, R.P. Reed, Metall Trans A, 6 (1975) 1345-1351.

[63] V. Shrinivas, S.K. Varma, L.E. Murr, Metall Mater Trans A, 26 (1995) 661-671.

[64] J.A. Lichtenfeld, M.C. Mataya, C.J. Van Tyne, Metall Mater Trans A, 37A (2006) 147-161.

[65] S.K. Varma, J. Kalyanam, L.E. Murr, V. Srinivas, J Mater Sci Lett, 13 (1994) 107-111.

[66] A. Nadai, Theory of Flow and Fracture of Solids, Second ed., McGraw Hill Book Company, Inc., New York, Toronto and London, 1950.

[67] F. Montheillet, M. Cohen, J.J. Jonas, Acta Metall, 32 (1984) 2077-2089.

[68] J.H. Poynting, P R Soc Lond A-Conta, 82 (1909) 546-559.

[69] H. Swift, W., Engineering, 163 (1947) 253.

[70] B.D. Cullity, S.R. Stock, Elements of X-ray Diffraction, Third ed., Prentice Hall, Upper Saddle River, New Jersey, 2001.

[71] M. Hatherly, W.B. Hutchinson, An Introduction to Textures in Metals, Institution of Metallurgists, London, 1979.

[72] M.G. Stout, J.S. Kallend, U.F. Kocks, M.A. Przystupa, A.D. Rollett, Proc Int Conf Textures Mater, 8th, (1988) 479-484.

[73] W. Gambin, Plasticity and Textures, Kluwer Academic Publishers, Dordrecht/Boston/London, 2001.

[74] U.F. Kocks, C.N. Tome, H.R. Wenk, Texture and Anisotropy, Cambridge University Press, 1998.

[75] E.A. El-Danaf, A. Al-Mutlaq, M.S. Soliman, Mater Sci Eng A-Struct, 528 (2011) 7579-7588.

[76] D. Raabe, K. Luecke, Mater Sci Forum, 157-162 (1994) 597-610.

[77] J.L. Raphanel, P. Vanhoutte, Acta Metall, 33 (1985) 1481-1488.

[78] A.W. Stephens, in, University of Arizona, 1968.

[79] S. Suwas, A.K. Singh, K.N. Rao, T. Singh, Z Metallkd, 93 (2002) 928-937.

[80] B.R. Kumar, A.K. Singh, S. Das, D.K. Bhattacharya, Mater Sci Eng A-Struct, 364 (2004) 132-139.

[81] D. Raabe, Mater Sci Tech Ser, 11 (1995) 985-993.

[82] L.S. Toth, P. Gilormini, J.J. Jonas, Acta Metall, 36 (1988) 3077-3091.

[83] L.S. Toth, J.J. Jonas, Proc Int Conf Textures Mater, 8th, (1988) 337-342.

[84] G.R. Canova, U.F. Kocks, J.J. Jonas, Acta Metall, 32 (1984) 211-226.

[85] L.S. Toth, J.J. Jonas, D. Daniel, J.A. Bailey, Textures and Microstructures, 19 (1992) 245-262.

[86] D.A. Hughes, R.A. Lebensohn, H.R. Wenk, A. Kumar, P Roy Soc Lond A Mat, 456 (2000) 921-953.

[87] K. Sekine, P. Van Houtte, J. Gil Sevillano, E. Aernoudt, Proc Int Conf Textures Mater, 6th, (1981) 396-407.

[88] P. Van Houtte, E. Aernoudt, K. Sekine, Proc Int Conf Textures Mater, 6th, Vol. 1 (1981) 337-346.

[89] J. Baczynski, J.J. Jonas, Acta Mater, 44 (1996) 4273-4288.

[90] R.O. Williams, T Metall Soc AIME, 224 (1962) 129.

[91] F. Montheillet, P. Gilormini, J.J. Jonas, Acta Metall, 33 (1985) 705-717.

[92] L.S. Toth, J.J. Jonas, P. Gilormini, B. Bacroix, Int J Plasticity, 6 (1990) 83-108.

[93] G. Kurdjumow, G. Sachs, Z Phys, 64 (1930) 325-343.

[94] Z. Nishiyama, Sci Rep Res Inst, Tohoku Univ, 23 (1934-35).

[95] G. Wassermann, Arch Eisenhüttenwes, 16 (1933).

[96] A.B. Greninger, A.R. Troiano, T Am I Min Met Eng, 185 (1949) 590-598.

[97] S. Kundu, H.K.D.H. Bhadeshia, Scripta Mater, 55 (2006) 779-781.

[98] M.P. ButronGuillen, C.S. DaCostaViana, J.J. Jonas, Metall Mater Trans A, 28 (1997) 1755-1768.

[99] N.J. Wittridge, J.J. Jonas, J.H. Root, Metall Mater Trans A, 32 (2001) 889-901.

[100] M.P. Miller, D.L. McDowell, J Eng Mater-T ASME, 118 (1996) 28-36.

[101] T. Marin, P.R. Dawson, M.A. Gharghouri, R.B. Rogge, Acta Mater, 56 (2008) 4183-4199.

[102] M. Doner, H. Chang, H. Conrad, J Mech Phys Solids, 22 (1974) 555-573.

[103] P. Brondsted, B.S. Johansen, V. Maegaard, P.S. Sorensen, Proc Risoe Int Symp Mater Sci, 15th, (1994) 255-261.

[104] L.S. Toth, J. Lendvai, I. Kovacs, B. Albert, J Mater Sci, 20 (1985) 3983-3987.

[105] L.E. Murr, K.P. Staudhammer, S.S. Hecker, Metall Trans A, 13 (1982) 627-635.

[106] F. Szekely, I. Groma, J. Lendvai, Mater Sci Eng A-Struct, 277 (2000) 148-153.

[107] B. Hutchinson, L. Ryde, P. Bate, Proc Int Conf Textures Mater, 14th, 495-497 (2005) 1141-1149.

[108] L. Lutterotti, S. Matthies, H.R. Wenk, A.S. Schultz, J.W. Richardson, J Appl Phys, 81 (1997) 594-600.

[109] B. Cina, Acta Metall, 6 (1958) 748-762.

[110] F. Bachmann, R. Hielscher, H. Schaeben, Sol St Phen, 160 (2010) 63-68.

[111] E. Cakmak, H. Choo, K. An, Y. Ren, Mater Lett, 65 (2011) 3013-3015.

[112] R.A. Lebensohn, C.N. Tome, Acta Metall Mater, 41 (1993) 2611-2624.

[113] L.S. Toth, K.W. Neale, J.J. Jonas, Acta Metall, 37 (1989) 2197-2210.

[114] J.J. Jonas, L.S. Toth, Scripta Metall Mater, 27 (1992) 1575-1580.

[115] P. Chapellier, R.K. Ray, J.J. Jonas, Acta Metall Mater, 38 (1990) 1475-1490.

[116] Q. Xue, J.F. Bingert, B.L. Henrie, G.T. Gray, Mater Sci Eng A-Struct, 473 (2008) 279-289.

[117] J.J. Jonas, Int J Mech Sci, 35 (1993) 1065-1077.

[118] E.S. Perdahcioglu, H.J.M. Geijselaers, J. Huetink, Mater Sci Eng A-Struct, 481 (2008) 727-731.

[119] F.J. Humphreys, J Mater Sci, 36 (2001) 3833-3854.

[120] T. Ungar, L.S. Toth, J. Illy, I. Kovacs, Acta Metall, 34 (1986) 1257-1267.

[121] H. Fujita, S. Ueda, Acta Metall, 20 (1972) 759.

[122] J. Weertman, S.S. Hecker, Mech Mater, 2 (1983) 89-101.

[123] A. Shibata, H. Yonezawa, K. Yabuuchi, S. Morito, T. Furuhara, T. Maki, Mater Sci Eng A-Struct, 438 (2006) 241-245.

[124] C.L. Magee, R.G. Davies, Acta Metall, 20 (1972) 1031.

[125] A.J. McEvily, R.C. Ku, T.L. Johnston, T Metall Soc AIME, 236 (1966) 108.

[126] K. Spencer, J.D. Embury, K.T. Conlon, M. Veron, Y. Brechet, Mater Sci Eng A-Struct, 387-89 (2004) 873-881.

[127] T. Iwamoto, T. Tsuta, Y. Tomita, Int J Mech Sci, 40 (1998) 173.

[128] V. Talyan, R.H. Wagoner, J.K. Lee, Metall Mater Trans A, 29 (1998) 2161-2172.

Vita

Ercan Cakmak was born in Istanbul, Turkey, in 1985. He received his B.S. degree in Metallurgical and Materials Engineering (MME) from Istanbul Technical University (ITU), Istanbul, Turkey, in 2008. In the same year, he was admitted as a graduate student by the department of Material Science and Engineering (MSE) at the University of Tennessee at Knoxville (UTK), USA. He received the M.S. degree in MSE from UTK in 2009, and completed his Doctor of Philosophy degree in 2014.